FLUID DYNAMIC AND PERFORMANCE BEHAVIOR OF

MULTIPHASE PROGRESSIVE CAVITY PUMPS

A Thesis

by

SHANKAR BHASKARAN NARAYANAN

Submitted to the Office of Graduate Studies of
Texas A&M University
in partial fulfillment of the requirements for the degree of

MASTER OF SCIENCE

August 2011

Major Subject: Mechanical Engineering

FLUID DYNAMIC AND PERFORMANCE BEHAVIOR OF

MULTIPHASE PROGRESSIVE CAVITY PUMPS

A Thesis

by

SHANKAR BHASKARAN NARAYANAN

Submitted to the Office of Graduate Studies of
Texas A&M University
in partial fulfillment of the requirements for the degree of

MASTER OF SCIENCE

Approved by:

Chair of Committee,	Gerald Morrison
Committee Members,	Timothy Jacobs
	Gioia Falcone
Head of Department,	Dennis O'Neal

August 2011

Major Subject: Mechanical Engineering

ABSTRACT

Fluid Dynamic and Performance Behavior of
Multiphase Progressive Cavity Pumps. (August 2011)
Shankar Bhaskaran Narayanan, B.Tech., National Institute of Technology Karnataka
Chair of Advisory Committee: Dr. Gerald Morrison

It is common for an oil well to produce a mixture of hydrocarbons that flash when exposed to atmospheric pressure. The separation of oil and gas mixtures on site may prove expensive and lead to higher infrastructure and maintenance costs as well. A multiphase pump offers a good alternative with a lower capital cost and increased overall production.

A Progressive Cavity Pump (PCP) is a positive displacement pump type that can be used to pump a wide range of multiphase mixtures, including high viscosity fluids with entrained gas and solid particles in suspension. Despite its advantages, a PCP has a reduced ability to handle high gas-liquid ratios due to limitations of its elastomeric stator material required to overcome thermo and mechanical effects. Also the efficiency decreases significantly with increases in gas volume fractions and reduced differential pressures.

The current study focuses on studying the behavior of this unique pump in a wide range of GVFs and studying the effect of this ratio on overall efficiency, temperature and pressure distribution on the stator. The pump exhibits vibration issues at specific differential pressures and they have been studied in this work. This can be of critical value as severe vibration issues can damage the pump components such as couplings and bearings leading to high maintenance costs.

Another important issue addressed by this research is the behavior of this pump in transient conditions. Oil well production is highly unpredictable with unexpected rises and drops in GVFs. These transient conditions have been simulated by varying the GVF over wide ranges

and studying the pump's behavior in terms of load, temperature rises and instantaneous pressure profiles on the pump stator.

This thesis provides a comprehensive study of this pump, its operating ranges and behavior in off-design conditions to assist oil and gas exploration ventures in making an informed choice in pump selection for their applications based on field conditions.

Dedicated to the proudest man and the strongest woman I have ever known.

To my PARENTS …

ACKNOWLEDGEMENTS

NOMENCLATURE

$A_{rotor} =$		Cross-sectional area of rotor
$A_{stator} =$		Cross-sectional area of stator
$A_f =$		Fluid flow area
$A_i =$		Acceleration in the direction of the co-ordinate i (r, θ, z)
b=		Pressure drop co-efficient
$\beta =$		Thermal expansion coefficient
$\eta_v =$		Volumetric efficiency
e=		Eccentricity of rotor
$f=$		Friction co-efficient
$G_r =$		Grashof number
g=		Acceleration due to gravity
H=		Pump head
h=		Heat transfer co-efficient
k=		Polytropic gas constant
L =		Axial length of stator
$m_{ai}=$		Mass flow rate of air
N =		RPM of pump
$\eta=$		Efficiency
$P_x =$		Pressure at an axial distance x from the pump inlet

$P_i=$ Pump intake pressure

$P_d =$ Pump discharge pressure

$\rho_g=$ Gas density

$\rho_l =$ Liquid density

$\rho_{ai} =$ Density of air inlet

$P_{ai}=$ Pressure of air inlet

$P_{drive} =$ Power input to drive

$P_{fluid} =$ Power input to fluid

$P_{Mechanical\ Losses} =$ Power lost due to mechanical losses

PID = Proportional integral derivative control algorithm

$P_s=$ Pitch of stator

$P_r =$ Prandtl number

$\Delta P =$ Differential pressure across pump

$Q_{ai}=$ Volume flow rate of air inlet

$Q_t=$ Theoretical volume displaced by pump

$Q_g=$ Gas flow rate

$Q_l=$ Liquid flow rate

$q_{s\_\mu}=$ Slip for a liquid with kinematic viscosity μ

$R_a =$ Rayleigh number

RPM = Revolutions per minute

$T_{ai}=$ Temperature of air inlet

$T_s =$ Surface temperature

$T_\infty =$ Ambient air temperature

$\Delta T =$ Differential temperature across pump

$t=$ Thickness of cavity slot

$\mu =$ Kinematic viscosity

$V_{fluid} =$ Velocity of fluid in pump

$V_{max} =$ Maximum velocity of particle

$w=$ Width of unfolded slot

$\omega =$ Angular speed of rotation

TABLE OF CONTENTS

LIST OF FIGURES

LIST OF TABLES

1. INTRODUCTION

Multiphase pumping technology is a relatively a new concept which replaces the conventional methods of separating the oil and gas mixtures on site. This technology aids in moving a mixture of oil, gas and sometimes even solid particulates to a central processing facility. The elimination of separation equipment at the production site reduces capital costs to a large extent.

Liquids of nearly any viscosity, liquid-gas mixtures, and even liquids with large solid particles in suspension can all be pumped equally well with a progressive cavity pump (PCP). Designed by the French engineer René Moineau in the 1930s, the PCP is constituted of two helical gears, one inside the other and rotating around their longitudinal axis which are parallel but spaced between each other. The external gear has one more thread or tooth element than the internal element.

The internal element is designed so as to be always in contact with the external element. The cross sections of the elements consist of couple profiles achieved by epicycloids and hypocycloid combination whose generator circles have a diameter of same length as the longitudinal axis of the two helical elements.

Currently, the PCPs are being widely used for lifting fluids from depths of 2000m and deeper in oil and gas wells. The progressing cavity pump offers to the petroleum industry a great number of advantages over traditional lift equipment, of which the most important is lowering the cost per barrel lifted.

The motion which leads to the formation of "closed cavities" is achieved by the movement of volume without deformation in a helical motion along the external element when the rotor

_____
This thesis follows the style of *SPE Journal*.

spins. As long as the helices of the external element run more than a single revolution the pump will enable a discharge pressure.

This method of pumping has a few distinct advantages:

1. Reversibility and self priming
2. Does not require a check valve
3. Uniform flow rate irrespective of differential pressure
4. Capability of handling liquids of varying viscosity and GVF

The stator is generally made of molded elastomer and designed to allow for slow swelling, long life duration and fair chemical and mechanical strength. The monitoring of the utilization temperature of this elastomer has been very critical as temperature fluctuations deform the stator altering the volumetric efficiency of the pump.
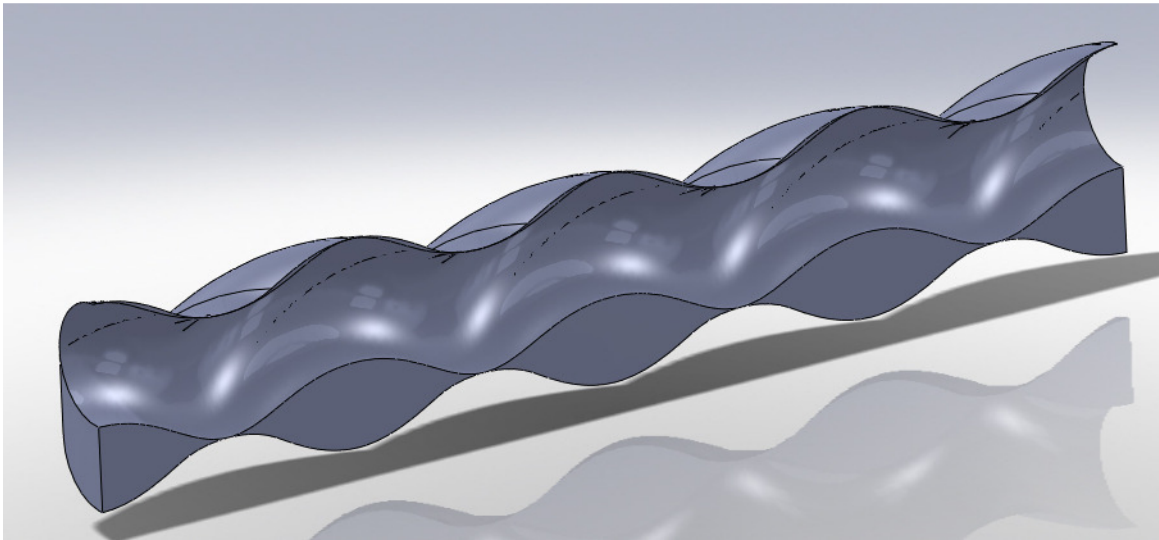
Figure 1.1 : Fluid path in a progressive cavity pump.

With low life cycle costs and operational simplicity, progressive cavity pumps are ideal for standard multiphase applications. The elastomeric stator makes it possible to even transport abrasive solid particles without much physical damage to the pump internals.
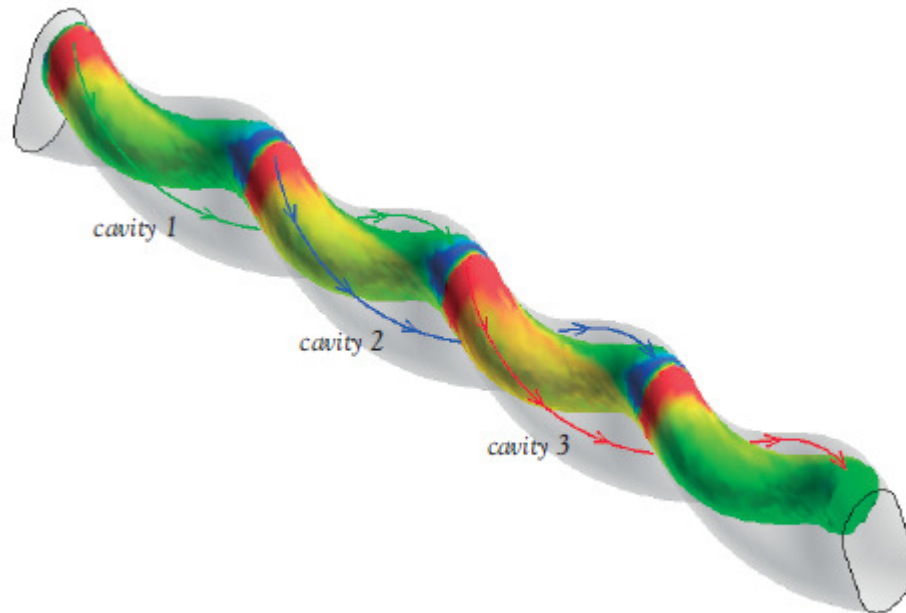
Figure 1.2: Cavity movement over a rotation and the movement of the fluid [1].

The general topic of this thesis is the experimental investigation of the fluid dynamic and performance behavior of a multiphase progressive cavity pump. Figure 1.1 and Figure 1.2 and illustrate the fluid path and the overall direction of flow respectively. During the experimental phase, a progressive cavity pump was used, which was geometrically characterized by a ratio of inner to outer screw diameter of 128 mm to 296 mm, a thread pitch of 612 mm as well as a screw package length of 120 mm.

Although these pumps have been studied for multiphase flows, there is no substantial work analyzing the behavior of this pump at high GVFs and the related vibration issues.

Phase-1 of the project focused on studying the pump at high gas volume fractions. The axial distribution of pressure and temperature for a range of GVFs was investigated. The volumetric flow rate and its dependence on suction pressure was studied and the mechanical efficiency of the pump at high GVFs was calculated.

The current work is intended to target the following issues:

- A range of GVFs have been investigated ranging from full water to 100% gas. For the high GVFs the process can also be termed as wet gas compression.

- The dependence of mechanical efficiency on GVF was studied which gave key insights into sizing the drive for the pump. A thermodynamic approach to calculating the power input the fluid was used to give more accurate results.

- The pumps response to transient conditions have been considered where the pump was subject to a drastic change in GVF from 75 % to running in full dry conditions and the dry out time was noticed. This was done to simulate actual field conditions where the extraction could be subject to slugs of pure gas or pure oil

- The pump was also subject to a surge of water when running at 98% GVF. This experiment would simulate the oil field condition where sudden surges of liquid could be observed in an otherwise dry running pump. The pressure build-up and temperature drop along the stator of the pump was studied in detail.

- The stator surface temperature at the last stage of compression was monitored and a heat transfer model was used to predict the rubber temperature. This would give an easy way to correlate the surface temperature to the actual rubber temperature and aid real time monitoring of the pump at high GVF. This is critical because prolonged exposure to high temperatures causes the rubber stator to swell leading to a change in cavity sizes which in turn affects the volumetric efficiency of the pump or cause pump failure.

- The effects of higher GVFs on the load of the pump have been studied. These are related because of the contribution of rubbing friction on the load of the motor.

- Severe vibration issues have been noticed at certain differential pressures in the pump. This could mean bearing dislocation at these conditions. Bearing failure could be critical in the field and if the pump is allowed to run at these conditions for prolonged periods it could cause permanent damage to the bearings and couplings. Accelerometers mounted at the bearing housing have been used to monitor the vibration at these conditions leading to the identification of conditions which could cause failure.

This thesis is divided into six sections. Section 2 is a literature review focusing on past experimental and analytical works on the PCP. Understanding how the basic analytical model of the pump is developed is vital in understanding the operating principles on which they function. Section 3 discusses on the theory and operating principles of the progressive cavity pump. Section 4 diagrams the experimental facility that was used to evaluate the PCP and the matrix of operating conditions performed. Section 5 presents the results of work done to investigate the feasibility of the two concepts presented. Section 6 summarizes the conclusions and recommendations of the total work.

2. LITERATURE REVIEW

Progressive cavity pumps were invented by René Moineau in the year 1930 while inventing a compressor for jet engines. He realized that this principle could be used to transport fluids and impart pressure. He went on to form a new company "Pompes Compresseurs Mécanique" PCM in 1932 which specialized in manufacturing the PCP. In 1936 some licensing arrangements were made with companies in the USA and eventually many industries began to manufacture this pump.

The progressive cavity pump (PCP) is a type of positive displacement pump capable of moving nearly any fluid. As illustrated by Karassik [2] and Brian Nesbitt [3] a PCP is a screw pump with a single, helical rotor. In the past these pumps were also referred to as eccentric gear pumps, eccentric screw pumps but the modern name is more apt for the description of the pumping mechanism. The pitch of the stator is two times that of the rotor allowing sealing of the cavities which, with rotation of the rotor result in a smooth axial flow of the liquid. Different kinds of couplings can be used based on the application and operating condition. The length of the rotor and stator can be increased to attain higher differential pressures.

More details about multi-lobe pumps can be found in Cholet [4]. Multi-lobe pumps have the following advantages over the conventional pumps:

- Higher capacity due to larger volume of fluid displaced.
- Lower value of eccentricity decreasing rotor unbalance and consequently pump vibration.
- Higher total head rating.
- Higher resistant toque due to lower operating speeds and hence lesser damage to the pump.

Although the design has gone through several iterations, the basic concept remains the same. One of the key advantages of this pump is its ability to pump products of ranging density and

high viscosity. Unlike a centrifugal pump, the pump head does not degrade with viscosity. Due to this versatility, this pump has been of key consideration for multiphase pumping. In oil exploration fields the chances of encountering a mixture of immiscible fluids including solid particulates is high and a pump has to be able to handle a wide range of the gas ratios involved. Most of the PCPs used for multiphase are installed on the surface but there are cases where they are installed vertically or down hole run by a long shaft. Studies by Delpassand [5] focused on the working mechanism while Gamboa et al.[6] [7] and Bratu [8] focused on pumping behaviors. These are discussed in detail in the following sections.

Bratu [8] studied the performance and behavior of the pump for GVFs ranging from 0-90%. He also suggested a new analytical model to predict the pressure and temperature distribution in the pump and how it varied for different GVFs. Figure 2.1 shows the pressure build up along the axis for a range of GVFs. It is evident that the pressure build up is non-linear and steeper towards the discharge at high GVFs. As GVF increases the pressure profile in the pump becomes more and more nonlinear.

An analytical model was developed by Bratu [8] where classical momentum and mass conservation equations are applied to multiphase compressible flow. The pressure distribution along the pump is determined by the pressure drop of slippage multiphase flow through rotor-stator contact. An iterative process is described in Appendix B where pressure distribution is related to slippage flow, but the slippage flow rate compensates the cavities gas compressed volume which again is a function of pressure distribution. A simple formula (Equation 2.1, 2.2) gives the pressure distribution as follows. This predicts a linear pressure profile along the axis for 0% GVF.

$$\frac{P_x}{P_d} = 1 - F\left(\alpha, \frac{x}{L}\right) \qquad \qquad 2.1$$

where P_x is the pressure at section x and P_d is the pressure at discharge. α is the gas volume fraction. The value of the polynomial was calculated. F is expressed as

$$F\left(\alpha, \frac{x}{L}\right) = \left[1 - \frac{2\alpha}{L}\left(1 - \frac{x}{2L}\right)x\right] \qquad 2.2$$
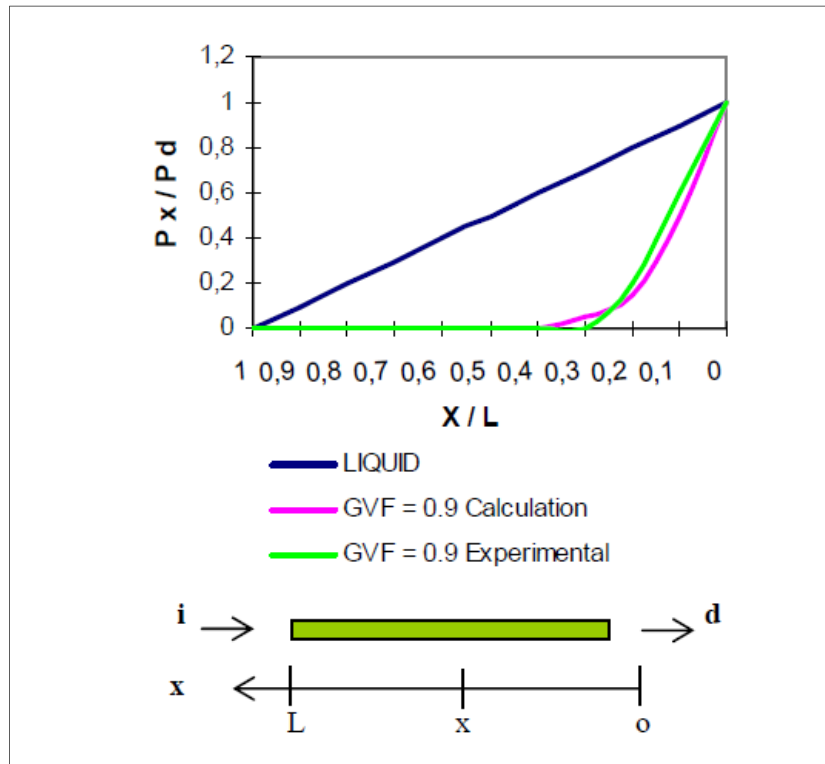
Figure 2.1: Axial pressure distribution for a range of GVFs [8].

Experiments concluded that the inlet volume of the gas was dependent on inlet pressure and compressibility of the gas needs to be taken into account. The dependence of inlet volume on inlet pressure and its dependence on GVF have not been studied in depth. Bratu [8] emphasized a co-relation between the viscous friction temperature T, pressure gradient P, co-efficient of friction f, and pump velocity N. Also there is a mention of dependence of motor torque on GVF but no significant experimental data was presented to correlate the motor Torque to the flow conditions. Figure 2.2 illustrates their findings of stator temperature dependence on RPM and GVF.

Bratu [8] concluded that a PCP's operational life can be improved by reducing the rotational velocity, delivered pressure and a tighter rotor-stator fit. The analytical formulas developed enabled improvement of the pump performance.

Gamboa et al.[7] computational and experimental work on the PCP emphasized a pump fitted with a metallic stator with a fixed, positive clearance around the single helical rotor. This kind of a pump eliminates wear due to friction and hence pumps have a longer life. However there is a decrease in the output flow rate due to leakage back to suction due to the fixed clearance. This leakage is called slip. These kind of pumps are hence different from the conventional elastomeric stator fit pumps as the latter have almost zero slip unless the stator has worn out. The geometric dimensions of the pump are summarized in Table 2.1**.**
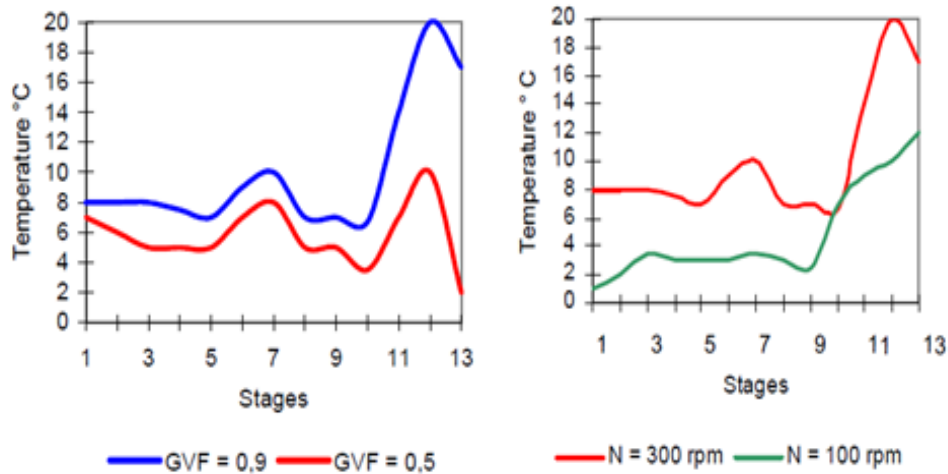
Figure 2.2 : Temperature of stator as a function of GVF and temperature [8].

Table 2.1 : Geometric parameters of PCP [7].

Interference (mm)	-0.37
Rotor diameter (mm)	39.878
Eccentricity (mm)	4.039
Stator Pitch (mm)	119.99

Pressure and temperature sensors installed on the stator helped monitor the pressure build-up across the stator. This helped in comparing experimental data to computational studies. Experiments were conducted both under single and multiphase conditions. Liquid viscosity in single-phase tests varied from 1-480 cP. Also light oil with a viscosity of 42 cP was used for multiphase tests. The upper limit of the GVF was limited to a 80%.

Computational studies were based on three different analytical models 1) flow past a rotating cylinder between two closely fitted parallel plates, 2) flow past a straight wall with a developed ("untwisted") stator flute moving axially along this wall – like a convergent divergent bearing space that has wedge flow and the associated developed positive and negative pressures, and 3) flow through a slit that models the clearance between the rotor and the surrounding stator (called the "Model of the PCP"). This was done for a fluid viscosity of 133 cP. This result demonstrated that the maximum velocity of the fluid is reached over the greater portion of the cross-sectional area of the cavity.

Figure 2.3 shows velocity profiles and the pressure distribution for the two-dimensional untwisted (developed) model, assuming that the fluid is Newtonian and has a viscosity of 133 cP, for an axial velocity of 30 cm/s. The differential pressure between the entrance and exit ports was equal to zero. Figure 2.3 shows that the moving rotor displaces all fluid inside pump without increasing the pressure. This result demonstrated that the pump operates in a manner similar to the relative movement of parallel plates, creating couette flow. Fluid moved axially without generating an increase of pressure, as with all positive displacement pumps. The increase of pressure in the discharge port produces a migration of fluid from this zone towards the cavity opened to discharge. This migration of fluid causes elevation of pressure in the cavity exposed, demonstrating that the pump reacts to the pressure, never generates it. Then the rotor must push the fluid until it has been expelled.
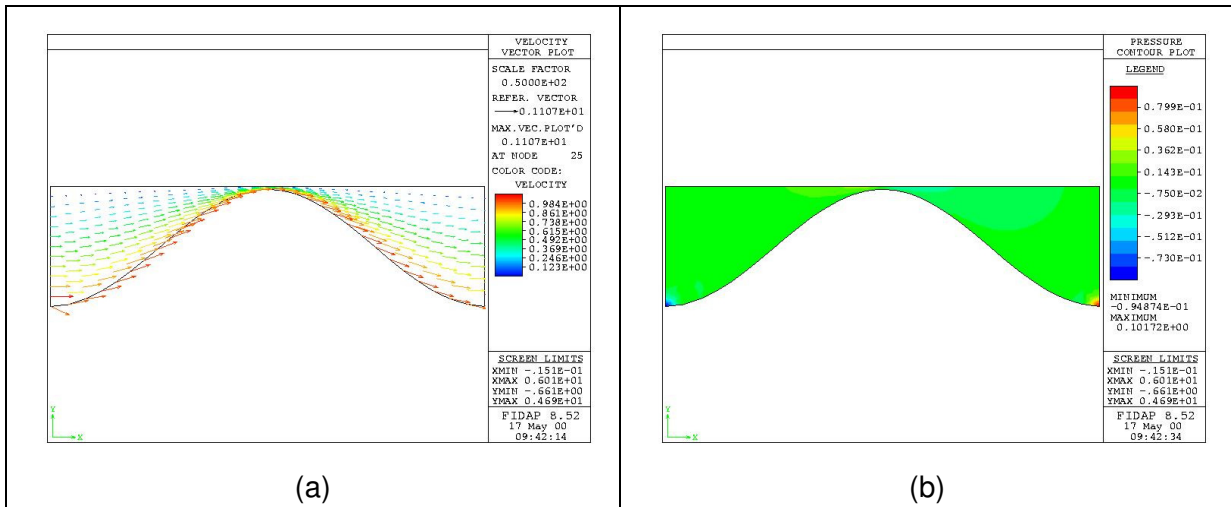
Figure 2.3 : Results of 2D untwisted model simulation. Tangential velocity of 30cm/s a liquid viscosity of 133cP and zero discharge pressure (a) velocity vector distribution (b) pressure distribution [7].

The cavity open to discharge takes on the pressure of the discharge port, creating a difference of pressure with respect to its adjacent cavity. This differential pressure produces leakage of the fluid between both cavities, which is called slip. The slip creates a region where the flow is a combination of that caused by the displacement of the rotor and that produced by the pressure difference.

Regions of high and low pressure near clearance regions were observed, indicating the preferential direction of the flow. The obtained results of the model untwisted by Gamboa et al.[6] demonstrated that the slippage between the cavities must be interpreted as a zone of stagnation where the relative velocity of the fluid with respect to rotor is reduced.

Figure 2.4 illustrates the results of modeling a PCP as a slit. This was done for a fluid viscosity of 133cP. It demonstrated that maximum velocity of the fluid was attained over the greater portion of the cross sectional area of the cavity. The small number of elements prevented better results in this case. Experimental studies were conducted to verify computational results and study the buildup of pressure across the axial length of the pump.
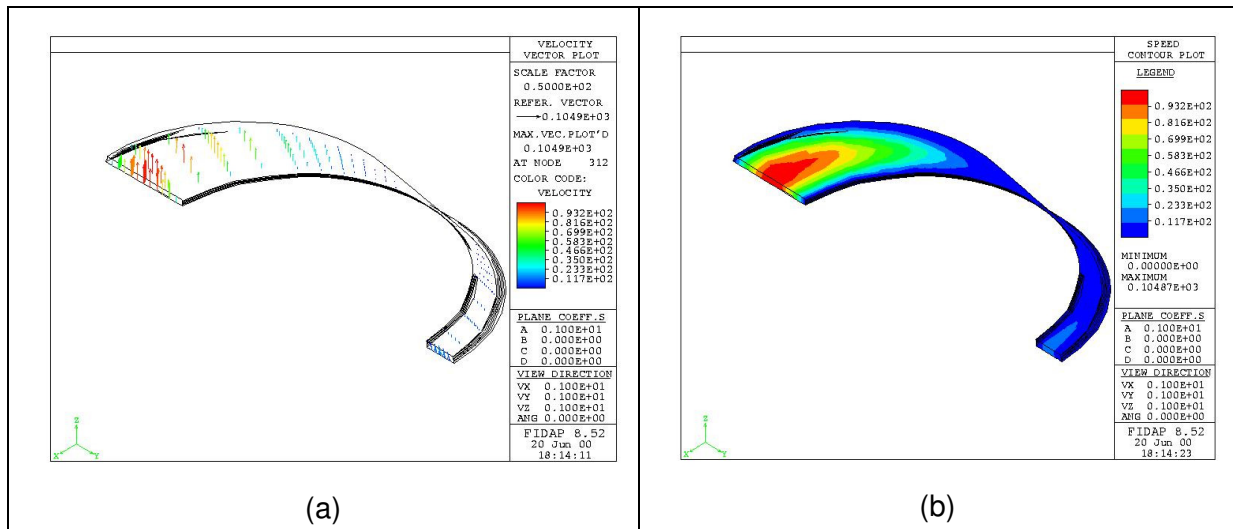
Figure 2.4 : Results of flow simulation within a slit. Models the slip in a PCP
(a) velocity vector distribution (b) contours of velocity for the same domain [7].

Experiments were conducted to study the flow curves over a range of rpm's, GVF's and viscosities. It was a clear observation that the flow reduced with greater differential pressure across the pump owing to back flow at higher pressure difference. This linear decrease in flow rate was not observed for fluids with low viscosity. Figure 2.5 illustrates this non-linearity in case of fluids with low viscosity. The increase in viscosity also produced a greater flow rate. Another consequence of viscosity was greater differential pressure at which zero-flow condition occurred. These observations are very specific to a pump with a positive clearance and it is unlikely that such observations could be made for our PCP which had an elastomeric stator. The behavior of the PCP in the current study would be different due to its zero clearance between the rotor and stator.
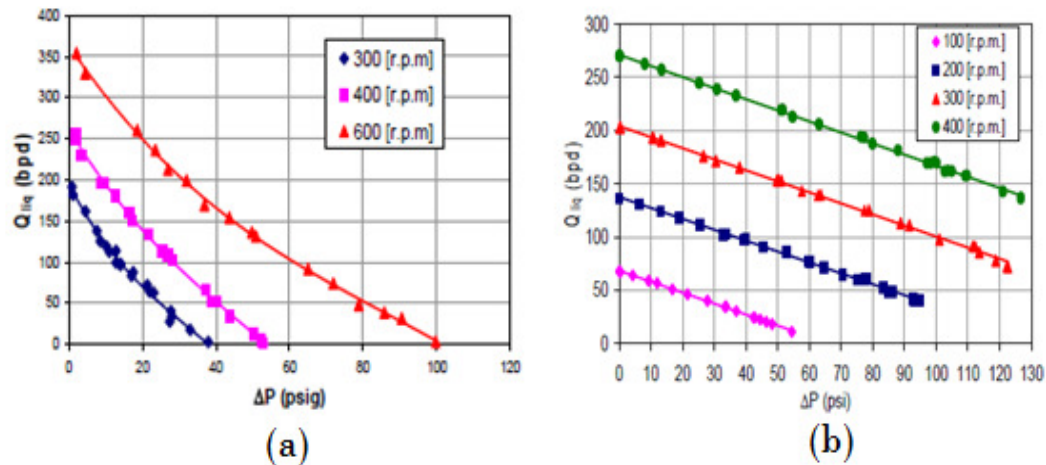
Figure 2.5 : Characteristic curves of Q vs Δ P. (a) 1cP (b) 42 cP [7].

An important observation was that at low RPM's the zero flow condition was reached at 5psig of differential pressure. This was different in behavior compared to PCPs with elastomeric stators implying that the PCPs with metallic stators have a minimum speed of operation required to overcome slippage and the pump performance also depended upon the properties of the material of the stator.

Not only do the results obtained demonstrated that the characteristic curve of a PCP with a metallic stator differs totally from the traditional curve of the PCP with an elastomeric stator material, but it was also concluded that there is some relationship between the mechanical properties of the stator material and the hydraulic behavior of the pump.

In case of two-phase flow curves there was an increased flow rate at higher GVF and the decrease of flow with differential pressure was not linear as in the case of single-phase flow. This is shown in Figure 2.6. For GVFs above 20% Gamboa et al.[7] observed 2 regions of operation called the "low pressure" zone ranging from 0 to a certain ΔP where the total flow of two-phase condition is above the single phase condition and a "High pressure" zone where flow rate for two-phase condition is less than that of single phase.

Egashira and Yamashita [9] have documented better volumetric efficiency when handling gas-liquid mixtures in twin-screw pumps. According to this previous work, a logical assumption could be that for the "low pressure" region the internal slip is principally that due to liquid. It means that the gas is not flowing through the clearance of the pump. On the contrary, this phase is trapped in the cavity, and as it moves with the cavity the gas is compressed. Since part of energy transfer to fluid is used in compression work, the slippage is lower.
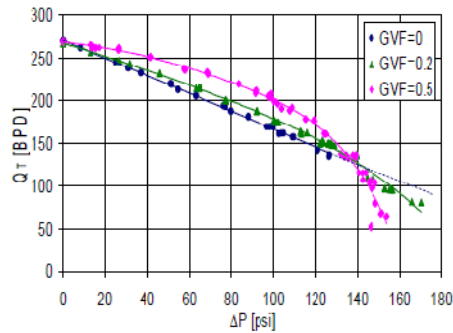
Figure 2.6 : Characteristic curve with two-phase flow at 400 rpm [7].

This could be better explained by observing the pressure rise along the length of the stator. The instantaneous pressure profiles were acquired by sensors installed axially on the pump stator. These profiles illustrated in Figure 2.7 are significantly affected by the GVF and show the pressure gradient along the axis.
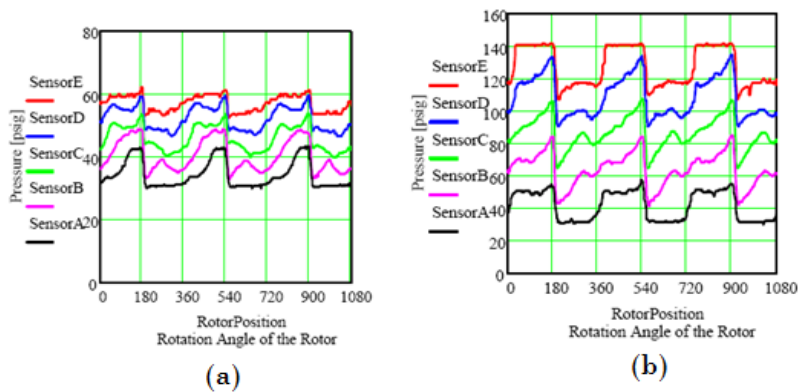
Figure 2.7 : Pressure profiles at 400 RPM. (a) GVF 80% $\Delta P = 28$ psi (b) GVF 20% $\Delta P = 114$ psi [7].

Here the increase of the GVF diminished the size of the pressure spikes associated with sealing lines within the pump. At 180º, the rotor is right upon the sensors, and they measure the pressure of sealing lines passing over them. At this point Sensors A and B registered pressure spikes. Belcher [10] observed pressure spikes for an elastomer stator PCP and explained them comparing the fluid film between the rotor and the stator with a convergent-divergent bearing. The presence of these pressure spikes also agreed with the results of simulations made for simplified models of a PCP with a metallic stator. It explained the increase of pressure in the clearance as being due to the fluid stagnation that takes place when the fluid pushed by the rotor encounters the fluid leaking through the clearance, and which is the product of the differential pressures between adjacent cavities.

Also the pattern of pressure build up at a single point changed drastically with GVF. Figure 2.8 illustrates the GVF effect on pressure build on a single sensor. Around 360º, first cavity is close to suction and discharge. When the rotor reaches this position under single-phase conditions, the internal pressure measured by the first sensor increased instantaneously due to the entrapment of the liquid. This position was called the "Close Point". Later, the rotor continued its movement while pressure inside cavity was 80% greater than suction pressure. In the cases of two-phase flow, the increase of pressure does not occur at 360º. For GVF=20 and 40%, the "Close Point" happened in 390° and the pressure inside the cavity was 60% greater than the suction pressure. Although the "Close Point" occurred in the same position for a GVF=80%, the pressure reached at this instant was hardly 30% greater than the suction pressure.

$$\text{Relative Increase in Pressure} = \frac{P_x - P_i}{P_i} \qquad\qquad 2.3$$

Gamboa et al.[7] concluded that instantaneous profiles of the first cavity demonstrate that it plays a fundamental role when the pump handles gas-liquid mixtures. Specifically, this cavity functions to reduce the fraction of gas in the mixture handled in order that the other cavities do not invest their work in compression. When other cavities (in addition to the suction)

perform the work of compression (as the case of GVF=80%) the pump operates less efficiently and total flow rate drops quickly at low differential pressure.

The analytical and experimental research by Gamboa et al.[6] validated the concept of utilizing a metallic stator in a progressive cavity pump (PCP). Even though a clearance between the rotor and stator was necessary causing an internal leakage or slip, the extensive experimental results reported herein confirmed the ability of this new PCP to handle single and two-phase fluids with reasonable volumetric efficiency. The tests were conducted on a PCP with a 40mm diameter rotor over a range of rpm, from 200 to 400 rpm. The pump pressure rise in the experiments reached 170 psi (1.17MPa) in two-phase flow for which the viscosity of the liquid phase was 42 cP and the gas void fraction (GVF) was 20%. At 80% GVF, the pressure rise was 130 psi (0.9MPa).
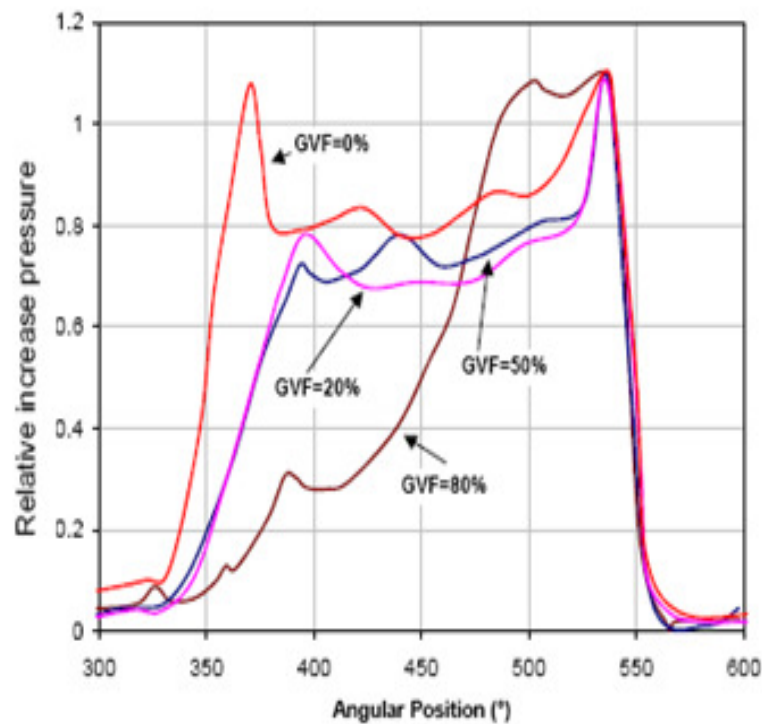
Figure 2.8 : Gas effect on instantaneous pressure. First cavity, at 300 RPM [7].

Desheng Zhou [11] et al did extensive work on the design of pump wells for PCPs. They analyzed the system performance of PCP wells based on the design of the pump. Nodal

analysis was used and wells were designed based on rotational speed, production rate and outflow performances. A very important breakthrough achieved was the study of the effect of inlet pressure and viscosity on performance.

A slot flow model is used to develop the co-relations. Though the papers main focus is on well design, the concept of cavity filling has been dealt with to a greater depth. It is emphasized that pump volumetric efficiency will drop if the cavity is partially filled. Hence complete filling of the cavity is essential for quiet and efficient operation. The critical pressure for intake has been shown to be

$$P_i = \frac{1}{8.04E6} \frac{l_s}{dt^3} \mu(nQ_t - q_{s\_\mu}) \qquad\qquad 2.4$$

The derivation has been detailed in Appendix C. The author also addresses the effect of viscosity on slip. Compared to other lifting methods a PCP can pump highly viscous fluids such as bitumen efficiently. Experimental data is used to conclude the effect of viscosity on slip. Gamboa et al[7] proposed a model for predicting slippage in a PCP but this was for the case of a metal stator and would fail for the case of an elastomeric stator as there is no clearance between the rotor and stator.

Due to difficulty in setting up a universal model for slippage flow it was suggested to use the individual manufacturer's performance curves. It is common knowledge that with higher viscosity the slip rate reduces and hence higher volumetric efficiencies are observed.

By unfolding the cavity, using average cross-sectional area and a slot flow model, critical pressures can be calculated for both Newtonian and Non-Newtonian fluids It was concluded that a decrease in rotational speed or increase in intake pressure by lowering the pump depth were good options to ensure cavity filling.

Jose Gamboa et al.[6] developed a new model to simulate the performance of a PCP taking into account the properties of stator material in 2003. The effect of differential pressure on

slippage gap was demonstrated and this gap was assumed constant for a metallic stator. This relationship was assumed to be of a quadratic form for an elastomeric stator. The model does not fit into any previous experimental data but complies with the PCP performance theory.
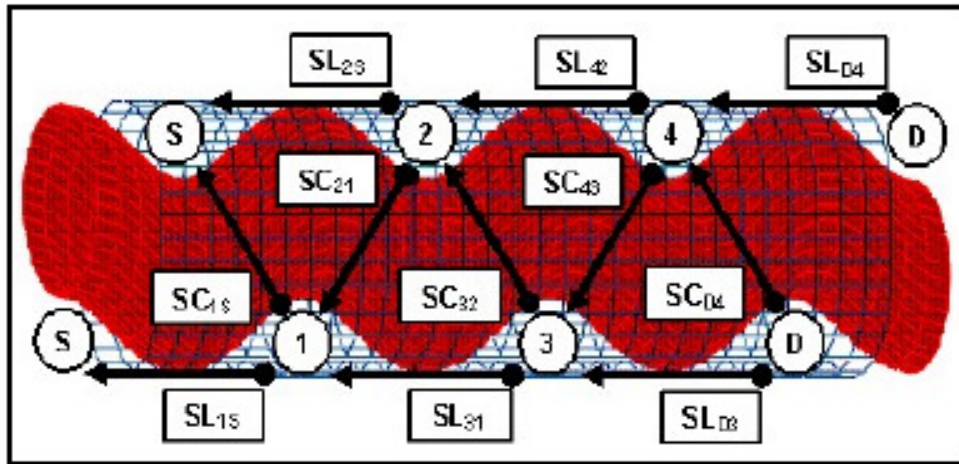
Figure 2.9 : Simplified PCP geometry to visualize internal slip [6].

In order to visualize the internal slip in the PCP a few simplifications were made. A sinusoidal trajectory was assumed for the rotor and the stator was assumed not to move. In this model cavities form and move due to the axial movement of an infinite length rotor. Figure 2.9 shows the simplified geometry with all components of slip.

In order to model the slip, three cases where considered when studying the effect of ΔP on the interference value. A constant value, a linear dependence and a quadratic dependence were assumed. Figure 2.10 shows a representation of this assumption.

With this approach, the characteristic curve of PCP is no longer linear but follows a non-linear curve as shown in Figure 2.11. The new approach to modeling internal slip flow in a PCP demonstrated that slip can be analyzed by assuming steady state flow theory in one specific rotor position. A more accurate approach could have been to investigate the gap at the region where leakage occurs. This would account for the curvature of the pump. Stator

deformation and its effect on the hydraulic behavior of the pump cannot be isolated from other factors and studied independently.
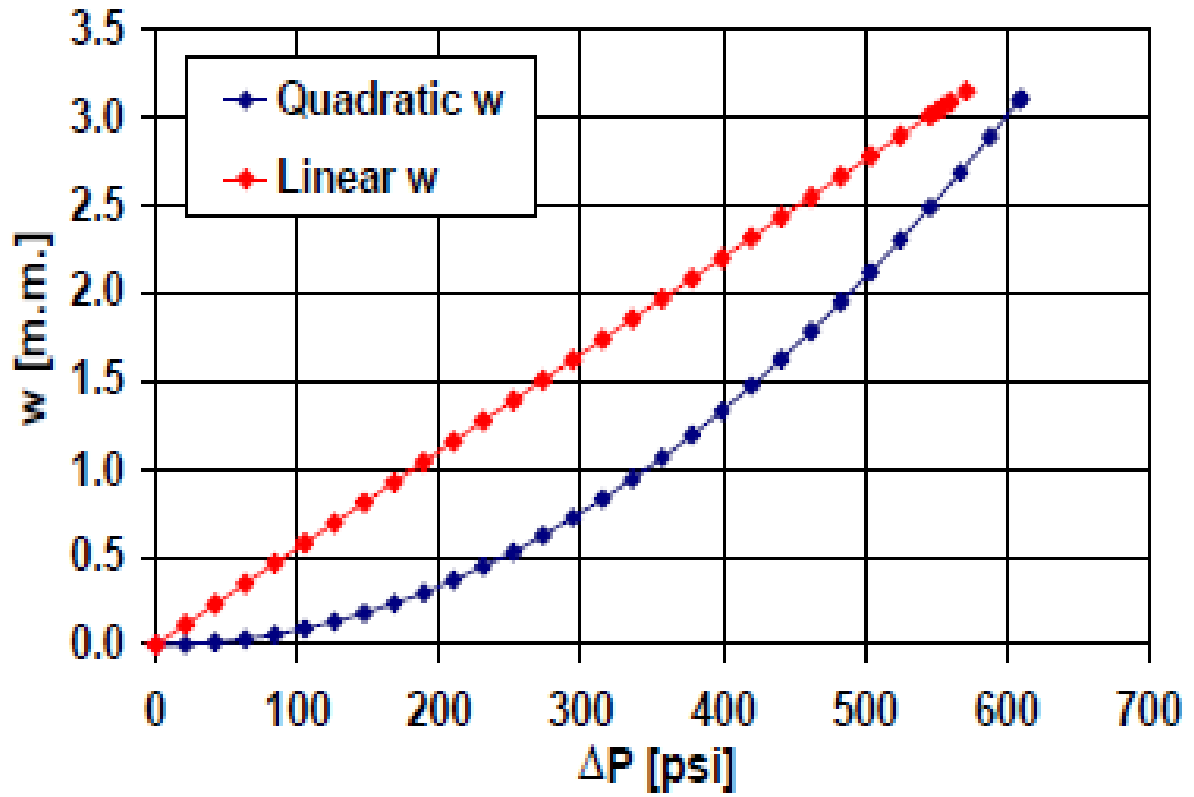
Figure 2.10 : Dependence of interference on ΔP [6].
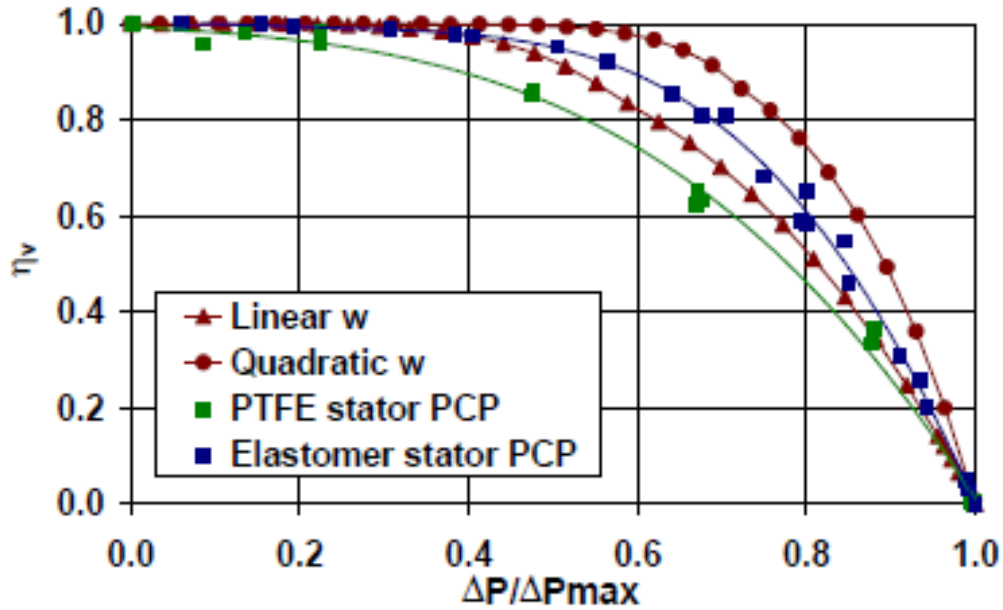
Figure 2.11 : Effect of variable slip on volumetric efficiency [6].

Delpassand [5] worked on the design and optimization for a PCP used in abrasive applications through modification of geometric design for minimum internal fluid velocities and by selecting proper materials of construction. Wear causes PC pump failure by reducing the volumetric efficiency and increasing pump slippage. The fluid velocity and slippage rate of the fluid as well as the particulates were assumed to cause most of the wear to the rotor. The fluid velocity was defined as

$$V_{fluid} = P_s * N \qquad\qquad 2.5$$

As the fluid never travels in a straight line, the maximum fluid velocity was calculated based on the longest path travelled by the fluid and hence

$$V_{max} = N * (P_s^2 + \pi^2(D + 4E_{cc})^2)^{\frac{1}{2}} \qquad\qquad 2.6$$

Pump wear was related to the geometric parameters D, E_{cc} and P_s. A ratio of $D/E_{cc} = 4$ was found to be optimum for minimum internal velocities of the fluid. PC pump internal velocity and flow rate increase as pump speed increases. As these parameters increase, the rate of particle impact to the rotor and stator increases which in turn accelerates rotor and stator wear. In general, the more abrasive the fluid, the slower the pump must operate. The amount of wear in an abrasive application is closely proportional to the speed squared of the pump. One detrimental effect that speed reduction may have on pump is illustrated in Figure 2.12 for a speed A and B where B is one half of A.

Since wear is assumed proportional to speed squared, it would take four times as long for a pump to wear at speed B compared to the same pump running at speed A. Although it would take almost four times as long to reach the same amount of wear at half the speed, the reduction in the volumetric efficiency would be doubled.
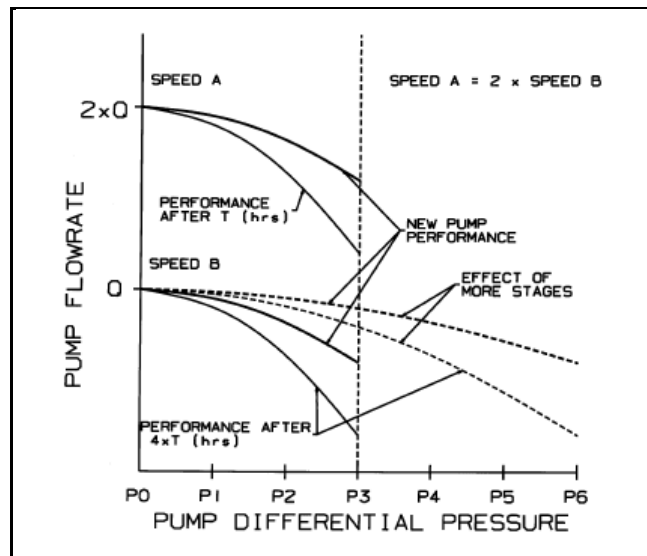
Figure 2.12 : Effect of wear on progressive cavity pump [5].

In most applications, this effect negates the usefulness of the longer life expected by reduction in speed. Using more pump stages for an abrasive application was recommended to compensate for this effect. This helped maintain high volumetric efficiencies under pressure

at even the lower speeds, reducing the effect of wear on flow rate and thereby increasing the time between pump replacements.

It was concluded by R and M Systems that progressive cavity pumps can be optimized to provide longer life in abrasive applications. Wear optimization of PC pumps could be achieved through pump geometric design, proper selection of stator elastomers and wear resistant rotor coatings, and proper sizing of the pump for the application. It was established that down-hole conditions such as concentration, size, and hardness of the sand particles influenced pump wear. PC pump life can be extended by reducing particle velocity through the pump, by running the pump at lower speed, and by adding more stages to the pump. Field results showed that the life of PC pumps can be increased significantly if pumps are optimized for the abrasive conditions.

3. THEORY

3.1   Fluid Flow Equations

Progressive Cavity Pumps (PCP) have a single helical rotor and stator. The cross section of a rotor is a circle with a diameter, d, at any place as shown in Figure 3.1. The centers of all cross sections are on a helical line with an eccentricity, e, with respect to the rotor's axis. The stator is a double internal helical gear with the same minor diameter as the rotor.

The cross-sectional area of the rotor and the stator are

$$A_{rotor} = \frac{1}{4}\pi d^2 \qquad\qquad 3.1$$

$$A_{stator} = \frac{1}{4}\pi d^2 + 4ed \qquad\qquad 3.2$$
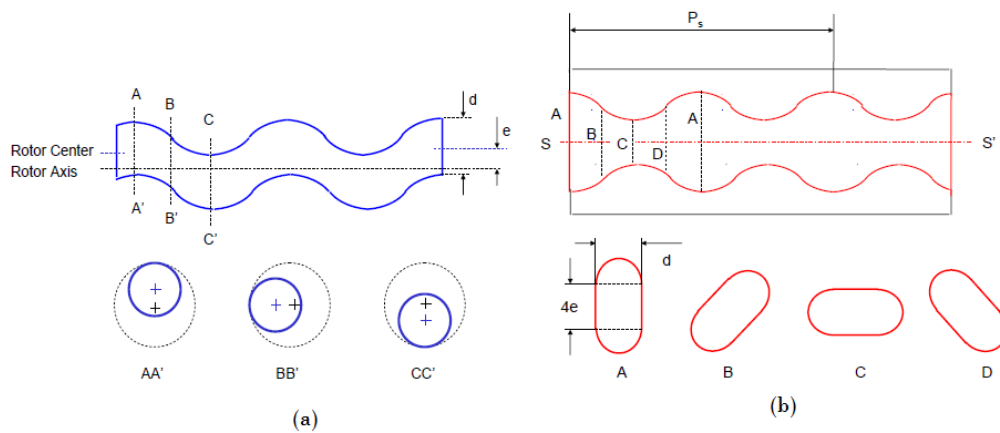
Figure 3.1: (a) A PCP rotor (b) A PCP stator [11].

The rotor rotates not only along its axis but also eccentrically around the stator center line with the same eccentricity of e. The cross-sectional area at any place could be modeled as a rectangle with width d and length 4e.

The fluid flow area is given by

$$A_f = 4ed \qquad\qquad 3.3$$

The 180^0 departed two cavities move one pitch, P_s, when the rotor goes through a full rotation. Hence the theoretical flow for a given speed of rotation n is given by the equation

$$Q_t = 4ednP_s \qquad\qquad 3.4$$

The actual flow rate is always less than theoretical flow rate due to internal slip in the pump. This slip is a function of differential pressure across the cavities. This can be seen in Figure 3.2. The slip characteristics also depend on clearance between rotor and stator, fluid viscosity and differential pressure and will be discussed in detail in the following sections. Hence the actual flow rate can be defined written as

$$Q_a = Q_t - Q_s = 4ednP_s - Q_s \qquad\qquad 3.5$$

hence the volumetric efficiency is given by

$$\eta_v = \frac{Q_a}{Q_t} = 1 - \frac{Q_s}{Q_t} \qquad\qquad 3.6$$
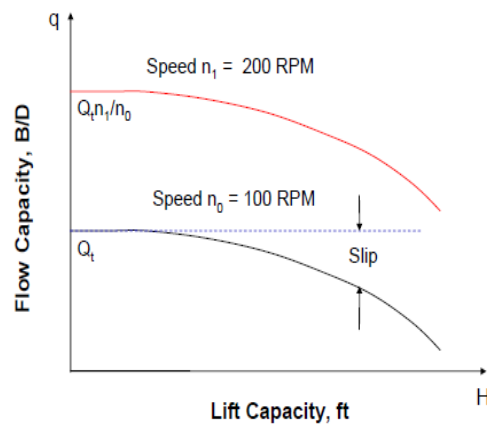
Figure 3.2 : Flow curve for half and full speed [11].

3.2   Two-Phase Pump Head and Density

The pump pressure, P, is equivalent to the two-phase pump pressure head and is given by Equation 3.7. [12]

$$H = \frac{1}{g} \int_{P_{inlet}}^{P_{outlet}} \frac{dP}{\rho_m} \; , \quad \rho_m = GVF * \rho_g + (1 - GVF) * \rho_l \qquad 3.7$$

where ρ_m is the mixture density, and ρ_g and ρ_l represent the density of the gas and the liquid. Therefore the pump total head includes flow pressure drop and well-depth. Considering the polytropic process relationship which associates gas density and pressure

$$\frac{P}{\rho_g^n} = CT \qquad 3.8$$

It can be concluded that at pump discharge pressure P the gas density reaches a maximum value and the pump head estimation becomes where ρ_m is evaluated at the discharge.

$$H > \frac{P}{g\rho_m} \qquad 3.9$$

3.3   Effect of Viscosity on Slip

The relationship of viscosity and slip is determined mostly by experimental data. A general analytical model is still being developed to model viscosity effects on slip. Gamboa et al.[7] set up a general model but it failed to predict performance for stators made of polymers. In general it can be said that the higher the viscosity of a fluid the lower would be the slip for a given differential pressure. This is due to resistance to flow offered from the liquid. Hence pumping a higher viscosity fluid would yield a higher volumetric efficiency.

One may use the following Karassik [2] empirical relationship to determine the effect of viscosity on flow rate.

$$\frac{q_{s\_\mu2}}{q_{s\_\mu1}} = \sqrt{\frac{\mu1}{\mu2}}$$

3.10

where $q_{s\_\mu1}$ and $q_{s\_\mu2}$ are volumetric slips for fluids with viscosities $\mu1$ and $\mu2$. Fluid viscosity varies with pressure and temperature and depends on fluid shear rate for non-Newtonian fluids. The shear rate in PCPs depends on rotational speed.

3.4 Cavity Filling and Critical Intake Pressure

As the PCP rotates a cavity opens and fluid enters the cavity. Until the rotor rotates and pushes the fluid the pump does not do any work on the fluid. The rotor rotation just creates a void for the entrance. The fluid is not pulled by the pump but rather pushed in by the intake pressure of the fluid. Pump volumetric efficiency would reduce greatly if the cavity is partially filled. The critical intake pressure for cavity filling is defined as

$$P_{in} = \frac{1}{8.04E6} \frac{l_s}{dt^3} \mu(nQ_t - q_{s\_\mu})$$

3.11

where d is the diameter of the rotor and l_s is the spiral length of a cavity in one stator pitch, t is the average cavity thickness. P_{in} is the critical intake pressure and n is the rotational speed in RPM.

$$l_s = (P_s^2 + (\pi(d + 4e))^2)^{\frac{1}{2}}$$

3.12

$$t = \frac{4eP_s}{\pi l_s}$$

3.13

This critical pressure defines the pressure below which the cavity cannot be completely filled. The critical speed for rotation is

$$n = \left(\frac{8.04E6dt^3 p_{in}}{l_s \mu} + q_{s\_\mu} \right) / Q_t \qquad 3.14$$

If the speed is more than the critical speed it leads to partial cavity filling and hence a reduced volumetric efficiency. Decreasing rotational speed for a given intake pressure could significantly improve volumetric efficiency of a pump. By unfolding the cavity into a rectangular cross-section Desheng Zhou [11] has developed a slot flow model to determine critical intake pressures and critical speed of rotation.

3.5   Gas Volume Fraction Calculation for the Present Study

The gas volume fraction is calculated based on the volumetric ratio of air to water entering the pump suction. The mass flow rates of the air and water are measured by the supply system. The air mass flow rate is calculated at the air supply pressure and temperature which is different from the pump inlet. The flow rate of water remains constant once the valves are set but the volume flow rate of the air is dependent on the supply tank pressure and inlet pressure of the pump. The volume flow rate of air entering the pump is based on constant mass flow rate between the tank supply and pump inlet.

$$\rho_{ai} = \frac{P_{ai}}{RT_{ai}} \qquad 3.15$$

$$m_{ai} = \rho_{ai} \, Q_{ai} \qquad 3.16$$

where $m_{ai}, \rho_{ai}, Q_{ai}$ represent the mass, density and flow rate of air at air supply conditions. This mass flow rate remains constant and the volume flow rate at pump suction depends on pump inlet conditions. Hence

$$Q_g = m_{ai} / \rho_g \qquad\qquad 3.17$$

And

$$\rho_g = \frac{P_{in}}{RT_{in}} \qquad\qquad 3.18$$

where m_{ai}, ρ_g, Q_g represent the mass, density and flow rate of the air at the pump suction conditions.

Hence the gas volume fraction at the pump inlet can be represented as

$$\text{GVF} = \frac{Q_g}{Q_g + Q_l} \qquad\qquad 3.19$$

Q_l being the water flow rate at the suction side of the pump.

3.6 Pump Power and Efficiency

The pump efficiency is defined by several different efficiencies. The drive power, as shown in Equation 3.20 is equal to the input shaft power, measured on the driveshaft between the electric motor and the pump.

$$P_{drive} = \Gamma . \omega = \frac{\Gamma . \pi . n}{60} \qquad\qquad 3.20$$

where Γ is the Torque, ω is the angular velocity and n is the speed in rpm. The drive power is further resolved into the power imparted to the fluid, irreversibility of the compression process, and that lost due to mechanical losses in the components of the pump. For a PCP the majority of the friction is due to the rubbing of the stator and the rotor.

$$P_{drive} = P_{fluid} + P_{Mechanical\ Losses} + P_{Irreversible} \qquad\qquad 3.21$$

The fluid power is further split down into the power imparted to the fluid passing through the pump and the fluid leaking back into the pump. Figure 3.3 represents the power distribution into individual fractions. Assuming the process to be isothermal, the net theoretical power imparted to a two-phase fluid can be evaluated as

$$P_{net} = Q_l.\Delta P + Q_g.p_{in}.\ln\left[\frac{P_d}{P_i}\right] \qquad 3.22$$

where Q_L and Q_G are the volumetric flow rates of the liquid and gaseous phase at the pump inlet and ΔP is the pressure difference between the discharge and the suction of the pump. For polytropic compression the work imparted to the fluid is calculated as

$$P_{net} = Q_l.\Delta P + \frac{n}{n-1}Q_g.p_{in}.\left[\left(\frac{P_d}{P_i}\right)^{\frac{n-1}{n}} - 1\right] \qquad 3.33$$

n = Polytropic Constant. The value of n varies between 1.0 for an isothermal process and $k\left(\frac{C_p}{C_v}\right)$ for an isentropic process.
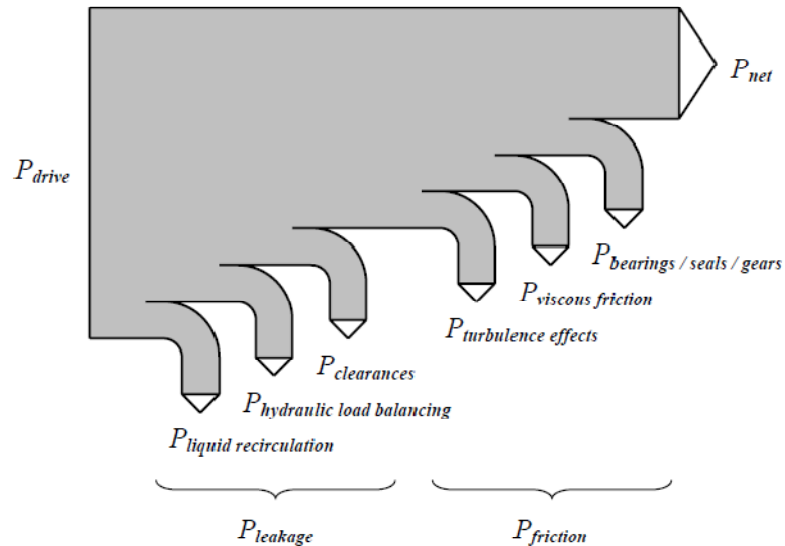
Figure 3.3: Power distribution during pumping operation [13].

A reference power for multiphase compression is the power required if 100% liquid passes through a 100% efficient pump at the same volumetric flow rate as the combined liquid and gas flow rate and is expressed as.

$$P_{ref} = (Q_l + Q_g).\Delta P \qquad\qquad 3.34$$

Three different definitions of efficiency are commonly defined for a multiphase pumping process, the mechanical, volumetric and thermodynamic efficiency.

$$\eta_{vol} = \frac{Q_{real}}{Q_{theoretical}} \qquad\qquad 3.35$$

$$\eta_{mech} = \frac{P_{net}}{P_{drive}} \qquad\qquad 3.36$$

$$\eta_{thermo} = \frac{P_{net}}{P_{ref}} \qquad\qquad 3.37$$

The volumetric efficiency is a measure of internal leakage of the pump. This could be flow through clearances and also intended back-flows. The leakage can provide effective sealing through the clearances at high gas volume fractions. The mechanical efficiency accounts for friction in the drives, irreversibilities in the compression process, and induced turbulence effects in the pump. The thermodynamic efficiency on the other hand is a measure of the ratio between ideal power needed to move the fluid to the power required if the fluid were fully incompressible. This would be 1 if the pump were operating on zero GVF.

3.7   Heat Transfer Model

Monitoring the temperature of the inner stator surface is of critical importance to the operation of the pump. As mentioned earlier, overheating of the pump stator can lead to wear which will result in lower volumetric efficiencies due to leakage flow. Also a higher

temperature can mean higher friction leading to more load on the drive. The measurement of stator surface temperature is not an easy task. This is due to the unique design of the pump with zero clearance between the rotor and stator surface. Hence the better approach used was to measure the stator temperature at the exterior. The temperature of the rubber surface was estimated using a heat transfer approach. The stator was estimated as along hollow cylinder consisting of both the rubber and aluminum sections with the thickness as stated by seepex. For an isothermal cylinder, Incropera et al. [14] suggested an expression of the form

$$\overline{Nu_D} = \frac{\bar{h}D}{k} = C Ra_D^n \qquad\qquad 3.38$$

where Ra_D^n is the Rayleigh number given by

$$Ra_D^n = \frac{g\beta(T_s - T_\infty)D^3}{\nu\alpha} \qquad\qquad 3.39$$

C and n are tabulated values. Churchill and Chu recommended a single co-relation for a wide range of Rayleigh number

$$\overline{Nu_D} = \left\{ 0.60 + \frac{0.387 Ra_D^{1/6}}{[1 + (0.559/Pr)^{9/16}]^{8/27}} \right\} ,$$
$$Ra_D < 10^{12} \qquad\qquad 3.40$$

The room temperature was assumed to be quiescent and the rubber aluminum interface was assumed to be a perfect interference fit. Considering convection to the atmosphere to be equal to the conduction through the layers of rubber and aluminum and upper limit temperature of 150° F on the stator surface was concluded to be the maximum allowable limit. This estimated the temperature of the rubber surface to be 190° F which was well below the upper limit of 200° F provided by seepex. Both Morgan's approach as well as Churchill's approach gave a value within 5% difference.

3.8   Torque Measurements

Differential pressure across the cavities contribute to the viscous friction torque. The interference between the rotor and the stator has been investigated by Bratu [8] and temperature becomes a measure of friction torque.

According to Bowden, the thermal energy developed due to viscous friction between the rotor and stator depended on the normal force. The normal force is a reaction to stator deformation which is a function of differential pressure between the cavities as well as the value of the interference fit between the rotor and stator. Hence we have the following co-relation for the pressure generated viscous friction temperature which is a measure of torque.

$$T_m = \ \Delta P_{n-m} * f * N \hspace{3cm} 3.41$$

f and N being the friction co-efficient (equivalent to Newton's dynamic viscosity) and the RPM of the pump respectively and ΔP_{n-m} is the measure of differential pressure across two subsequent cavities. This relationship has been used by Dunn, L et al. [15] and Samuel, G et al. [16] in their studies as well.

This is an important factor for pump reliability as heat generated can be controlled by the rotor-stator interference and pressure gradient across the pump. The friction co-efficient in case of multiphase pumping changes with changing GVFs and the study of the correlation of GVF to the torque in the shaft is of importance.
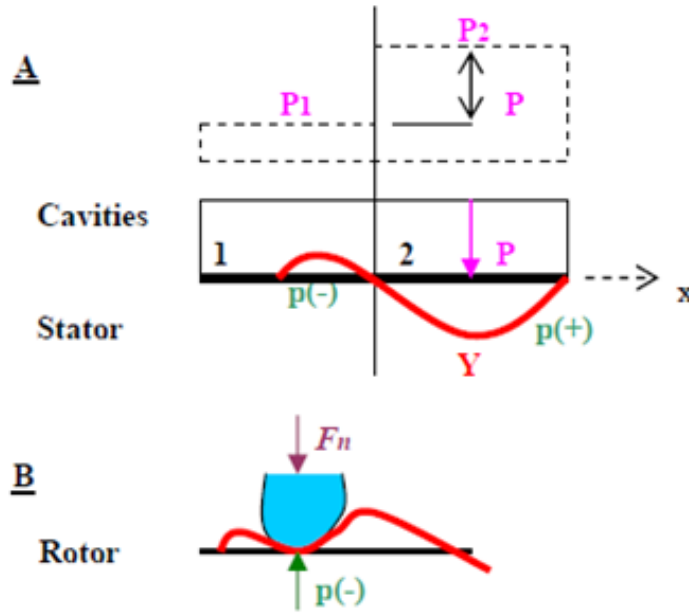
Figure 3.4 : Stator deformation due to pressure gradient inside the cavities [8].

3.9 Axial Temperature and Pressure Distribution

The pressure distribution inside the pump is a key factor in determining the pump performance. The classical momentum and mass conservation equations were applied to multiphase compressible flow by Bratu, C et al. [17]. The pressure distribution along the pump is a function of slippage flow through rotor-stator contact. In case of a compressed flow, the slip flow compensates for the reduced volume of the compressed gas and transmits pressure inside the cavities. An iterative process has been developed by Bratu,C et al. [17] where the pressure distribution is related to slip flow which compensates the cavities gas compressed volume which in turn is a function of pressure the distribution. Equation 3.42 describes the pressure distribution along the pump and has been derived in detail in Appendix B.

$$\frac{P_x}{P_d} = 1 - F\left(\alpha, \frac{x}{L}\right) \qquad\qquad 3.42$$

4. EXPERIMENTAL FACILITY

This section focuses on the multiphase experimental facility at the Turbomachinery Laboratory at Texas A&M University which was used to test the PCP at desired GVFs and flow rates. The multiphase flow was simulated by controlling the ratio of air and water at the pump inlet. The test rig is capable of both steady state and transient operations of all MPP with a maximum capability of 200HP.

4.1   Experimental Hardware
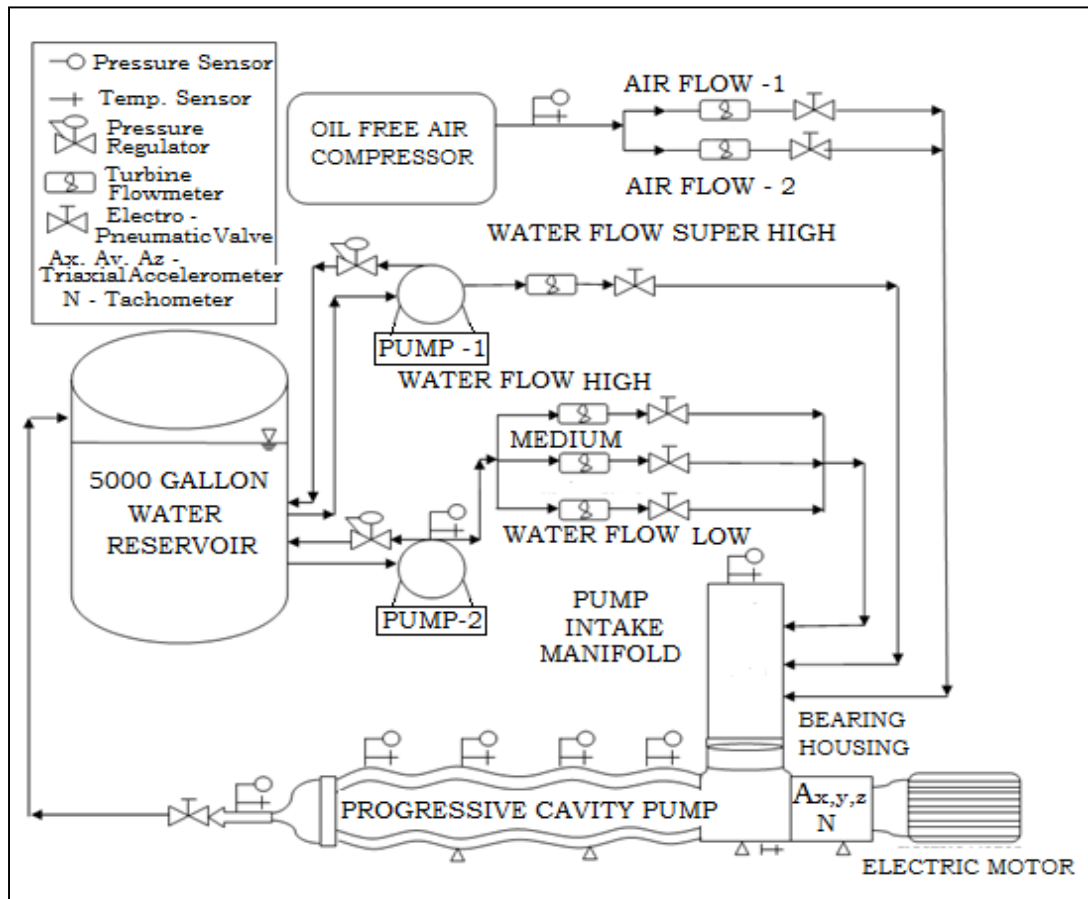
Figure 4.1 : Flow loop diagram.

The test rig is capable of both steady state and transient operations of all MPP with a maximum capability of 200HP. The facilities allow the easy installation and testing of MPPs which allows the rapid testing and development of this technology. Section 4.1 focuses on the overall system infrastructure installed in the laboratory allowing a plug and play approach to investigating MPP technology, Section 4.2 will focus on the PCP assembly, and Section 4.3 will focus on the data acquisition and instrumentation, and the experimental error analysis is detailed in Appendix D .

Figure 4.1 shows the circuit diagram for the system flow loop. All the components are described in detail. The water flow loop consists of two circulation pumps of 135GPM and 550GPM capacity respectively. The air flow loop consists of a series of compressors with a common storage tank. As explained in section 4.3.4 the flow rates are controlled by electro-pneumatic valves to maintain required pressures and flow rates. The water and air loops merge in the intake manifold of the pump inlet providing the pump with the desired multiphase mixture. The mixture is then pumped by the PCP and eventually the pumped mixture is separated. The water is then re-circulated to the storage tank and air let into the free atmosphere.

Figure 4.2 : Water supply reservoir.

Figure 4.2, Figure 4.3, and Figure 4.4 show the water supply system located outside of the laboratory. The water reservoir has a capacity of 5000 gallons. The water from the reservoir is fed to the dual centrifugal pump system with capacities of 135GPM and 550GPM respectively. The water pressure was held constant via back pressure regulators set to 120 PSI. After exiting the circulation pumps, the water flows through separate pipelines and enters the laboratory where the water flow manifold and control system is located.

Figure 4.3 : Circulation pump 1 (Capacity - 135 GPM).

Figure 4.4 : Circulation pump 2 (Capacity - 550 GPM).
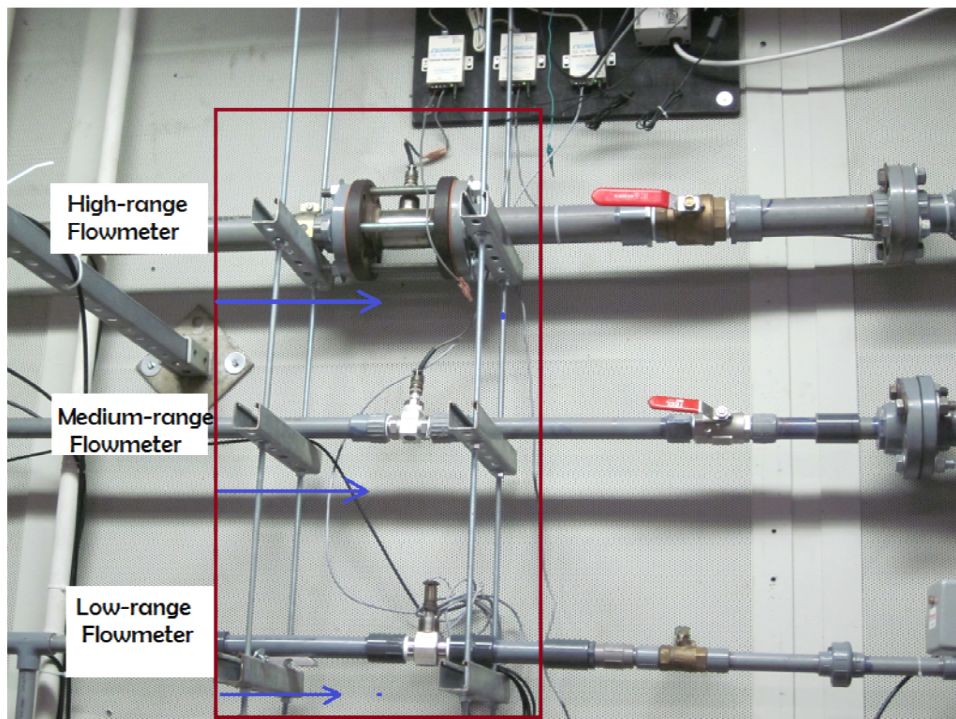
Figure 4.5 : Low, medium, and high water control and measurement manifold.
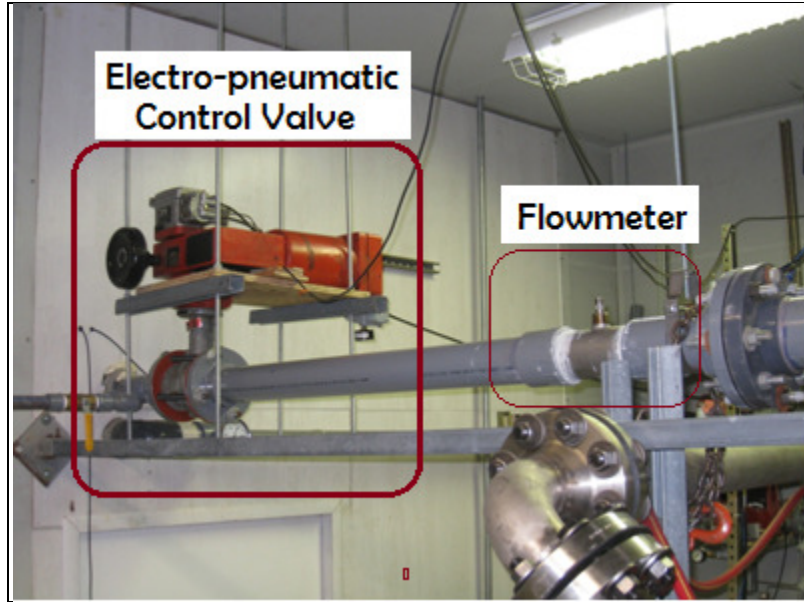
Figure 4.6 : Super high water control and measurement.

Figure 4.5 and Figure 4.6 show the water control manifold system once the supply enters the laboratory. The figures highlight electro-pneumatic valves controlled by 4-20mA input supplied by the NI-9205 module and a generic LabVIEW program developed for any MPP application. The control valves regulate the flow rate of water entering the positive displacement pump system. A total capacity of 685 GPM is available from the parallel water systems. The flow rate of the water is monitored using a manifold of turbine meters. Different flow meters and valves were used to account for the wide range of flow rates involved in the test matrix and the inability of any single flowmeter to accurately measure the entire range.

Figure 4.7 : Air compressor network.

The air compressor network shown in Figure 4.7 is made up of three 100 PSI oil free screw compressors used for this study. They are capable of supplying compressed air up to 150psi at the test section. This capacity was sufficient for our current requirements. Once the air is compressed it is then stored in a sealed tank and a pipeline is then plumbed directly into the laboratory area where it is met with an air control system explained in Section 4.3.8.
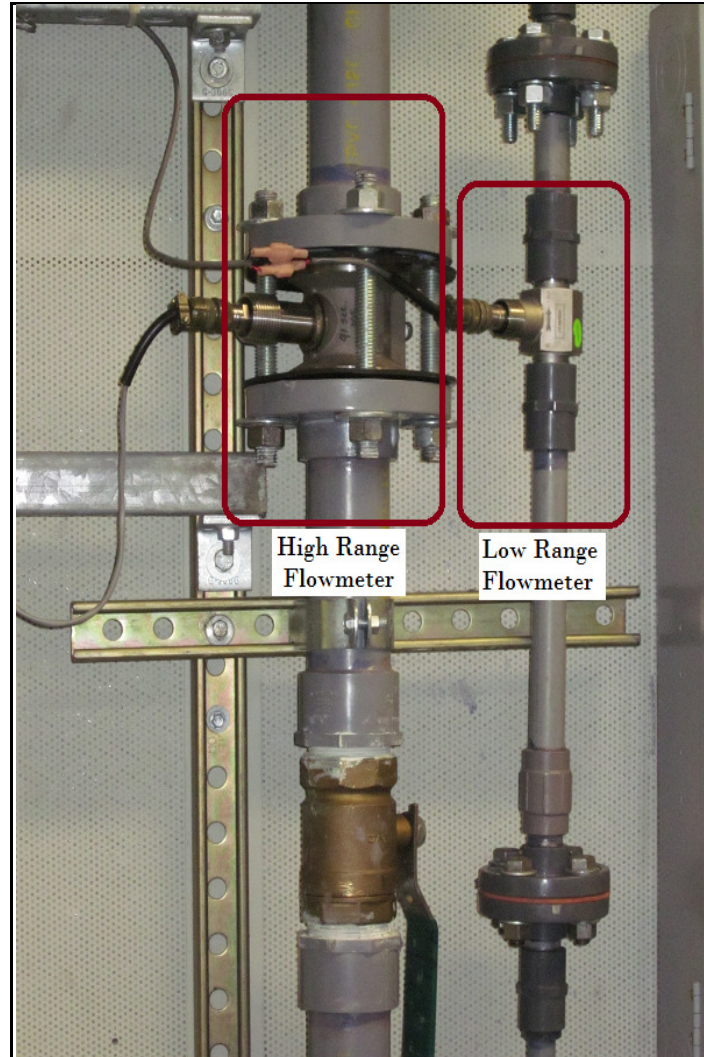
Figure 4.8 : Low and high range air flow measurement.

Figure 4.8 shows the airflow measurement system. It consists of a set of parallel turbine meters set up to monitor two different overlapping ranges of flow rates. It is followed by an electro-pneumatic valve operated from 4-20mA, temperature thermocouple, and pressure transducer. The sensor data and the control valve are also monitored from the LabVIEW data acquisition. The main difference between the water and the air control systems is that the water system controls a flow rate (GPM) while the air system controls the pump inlet pressure (psi) and holds it at a constant desired value. Through a series of calculations that

will also be presented in Section 3.5 the total flow rate and the corresponding GVF at the pump inlet was calculated.
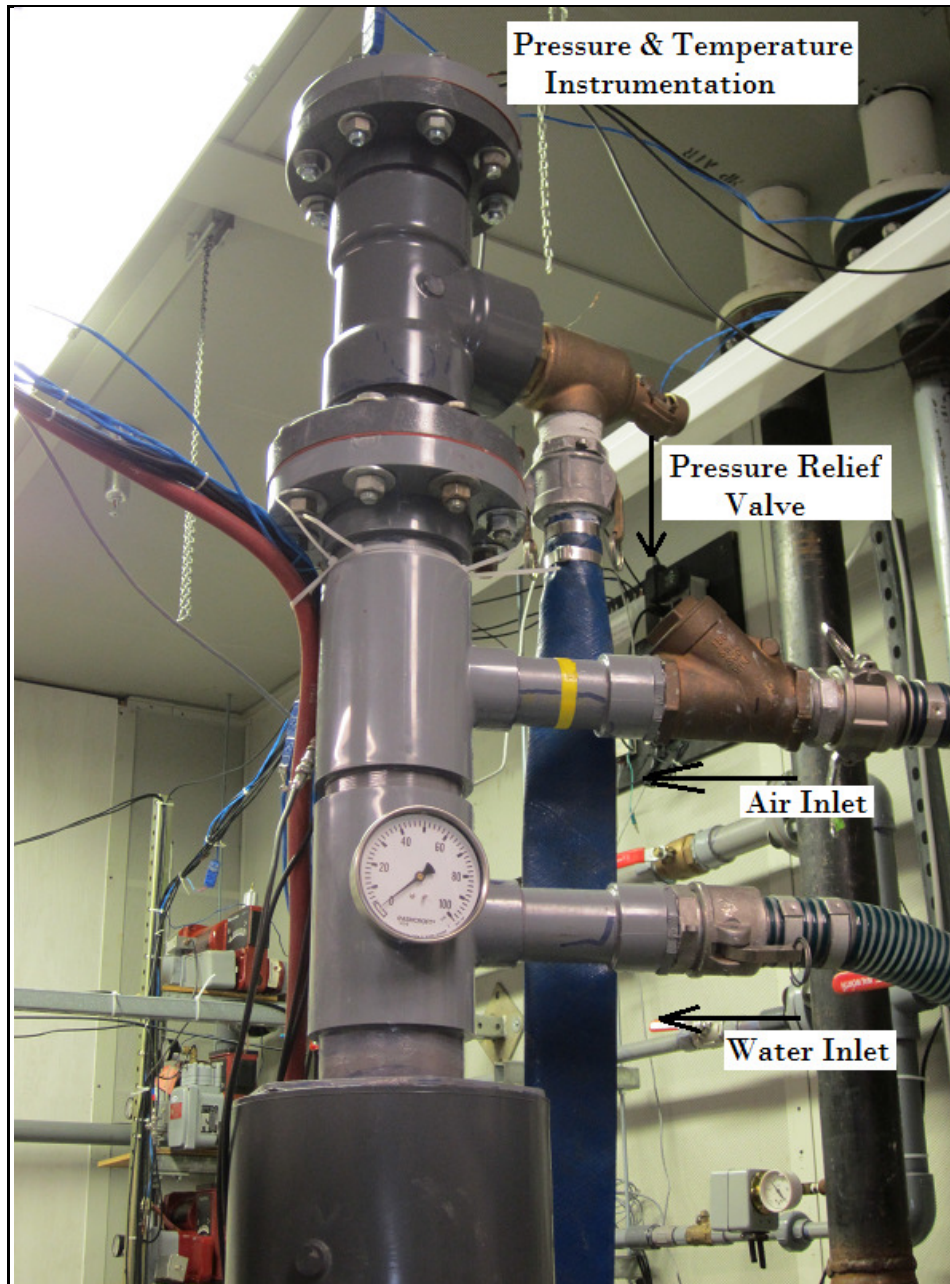
Figure 4.9 : Pump inlet manifold.

Figure 4.9 shows the pump inlet manifold which allows for the simultaneous input of both air and water downstream of their respective control valves. The manifold also contains a

pressure relief valve set to 50 psi to protect the pump from surges in pressure in case of failure of the pressure control algorithm. Pressure and temperature sensors mounted in the manifold allow inlet condition measurements. Two thermocouples were mounted in order to measure both air and water temperatures after it was realized that the two fluids were at different temperatures dependent on the inlet conditions. This also allowed for detailed thermodynamic calculations performed later.
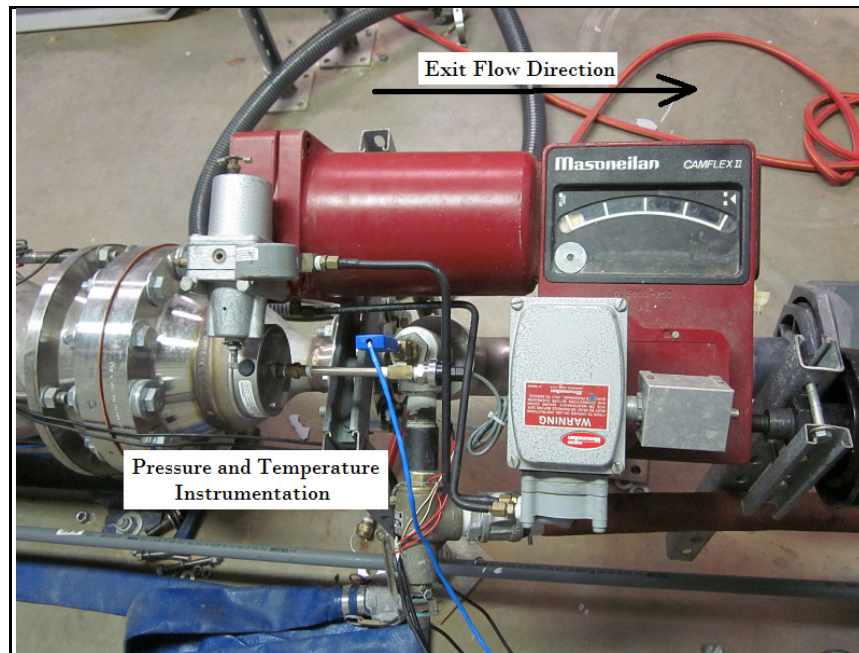
Figure 4.10 : Exit control valve.

The exit control valve shown in Figure 4.10 is also an electronic-pneumatic control valve operated from 4-20 mA. This control valve regulates the exit pressure of the pump via a manual control in the LabVIEW code. The exit pressure was manually controlled based on a DC averaged value. This method was preferred over the PID because of the pulsations involved in the exit. The restriction caused by the control valve simulated the pressure head caused by the pipeline in the real world application. A relief valve was installed in the pump exit too to protect the pump from accidental surges in pressure beyond the capacity of the pump.

The final component that makes up the testing infrastructure at the MPP laboratory is the Dynamatic variable frequency drive that supplied the driven pumps with electricity. This is illustrated in Figure 4.11. The intention behind using a VFD was to be able to run the driver at desired speeds. A VFD is a system for controlling the rotational speed of an AC electric motor by controlling the frequency of the electrical power supplied to the motor. All of the equipment and diagrams presented in this section will be utilized for the analysis being performed on the progressive cavity pump described in the following section.

Figure 4.11 : Variable frequency drive.

4.2   Progressive Cavity Test Pump

The 4-stage BN series progressive cavity pump that was used for the investigation was provided by seepex. Figure 4.12 shows the pump in the test facility integrated with the MPP

facility. The capacity of the pump is 640GPM with an inlet pressure of 50 psi and capable of a differential pressure up to 150 psi. The pump had an 8-inch inlet and outlet and was plumbed into the MPP facility through the inlet manifold and exit valve. The pump specifications are detailed in Appendix A. Figure 4.13 illustrates the interior cross-section of the stator cavity.

Figure 4.12 : Progressive cavity pump.
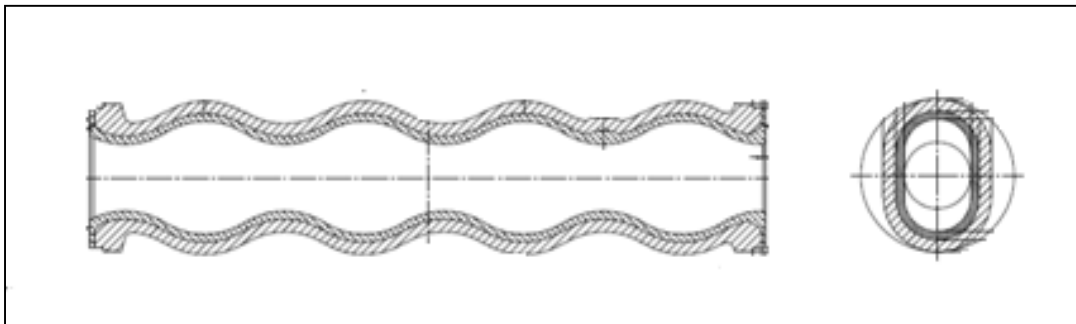
Figure 4.13 : Internal cross-section of the stator.

In order to measure the internal pump performance parameters and the behavior of the stator at varied gas volume fractions, pressure and temperature sensors were mounted along the axial length of the pump.

Figure 4.14 shows the location of the sensors along the pump stator. The sensors were located to measure the pressure build up along each stage of the pump. Beginning from the suction, these sensors were separated by a distance equal to the rotor pitch.
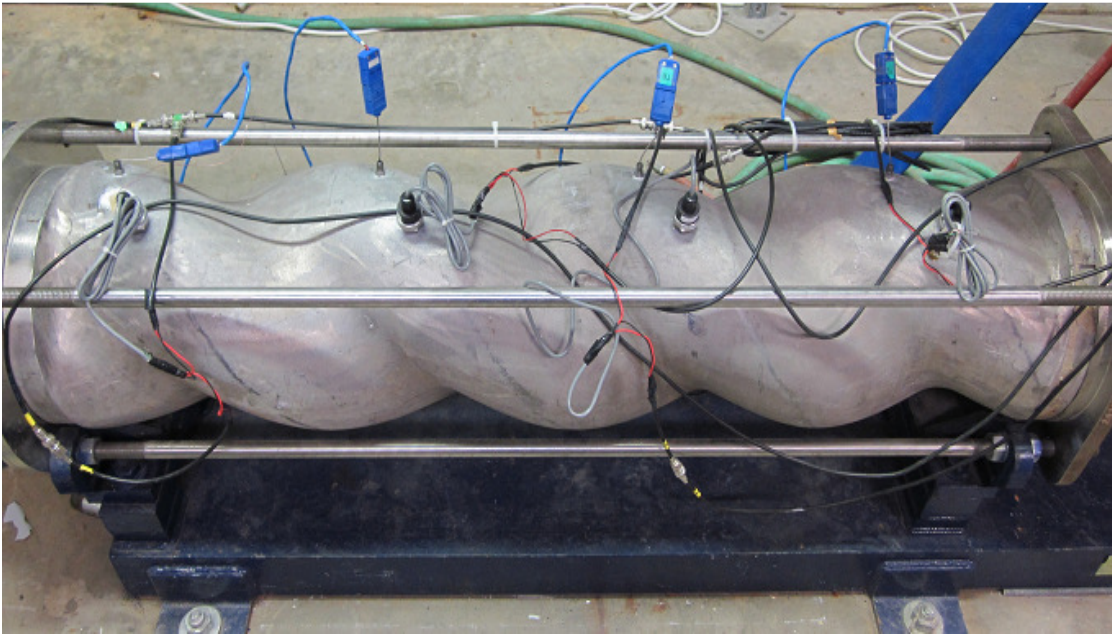
Figure 4.14 : Pressure and temperature sensors mounted on the stator.

Figure 4.15 : Location of a pressure and temperature sensor.

4.3   Sensor Types and Measurement Signals

To study the pump behavior and the flow characteristics for a wide range of GVFs different types of flow meters, pressure, temperature sensors and control valves were used. All the sensors were integrated on National Instruments platform of data acquisition cards and LabVIEW 2010 was used for PID control of flow control and data recording. A list of sensors used is enlisted in Table 4.2. The graphical user interface shown was designed to aid the user to monitor (Figure 4.16) as well as control (Figure 4.17) the parameters in the rig. Minimum manual control was utilized to ensure automated, user friendly control of the rig. These figures are indicative of the GUI and not the details of programming codes used.
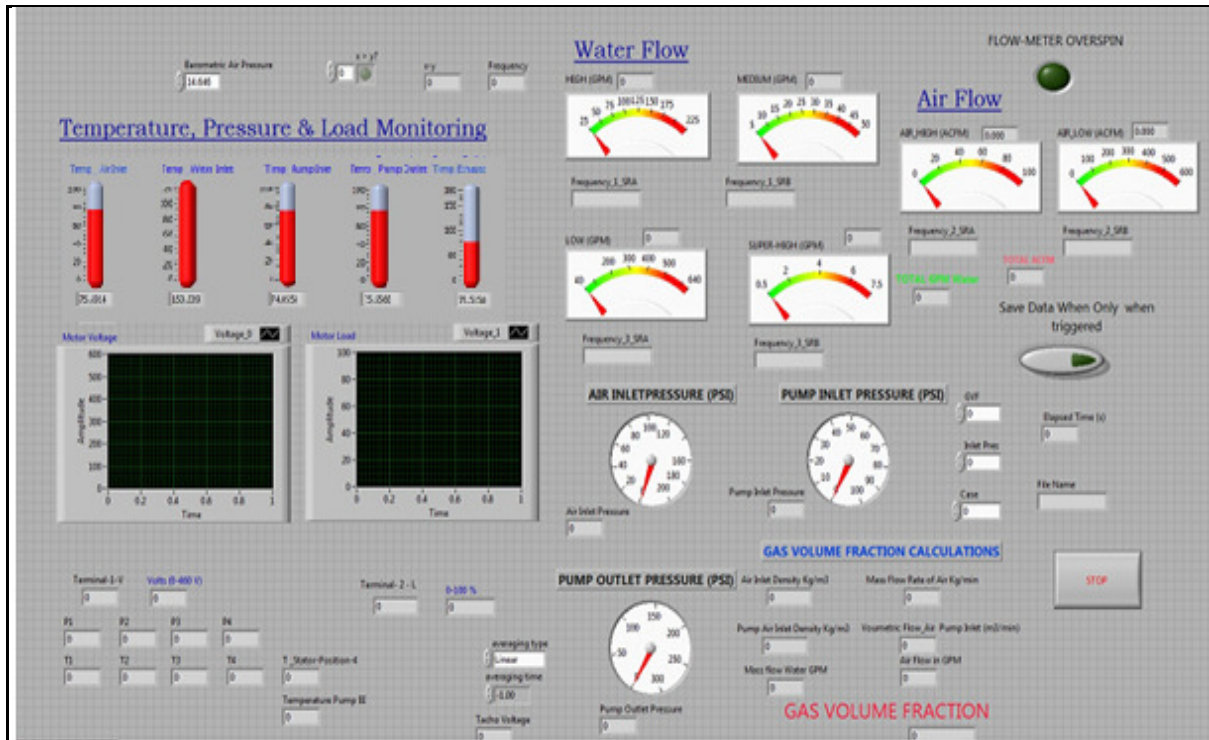
Figure 4.16 : GUI for parameter monitoring of MPP rig.

4.3.1 Pressure Sensors

Solid state pressure transducers from Omega PX-481 A-series were used. The range of pressure measurement depended upon the location of the sensor in the experimental apparatus. The sensors use an excitation voltage of 9-30 volt DC with an output voltage in the range of 1-5 volts. Their accuracy is within a 0.3% BSFL. The ranges used are, air inlet of 0-200 psi, pump inlet of 0-60 psi, pump outlet of 0-300 psi and pump axial location of 0-200 psi.
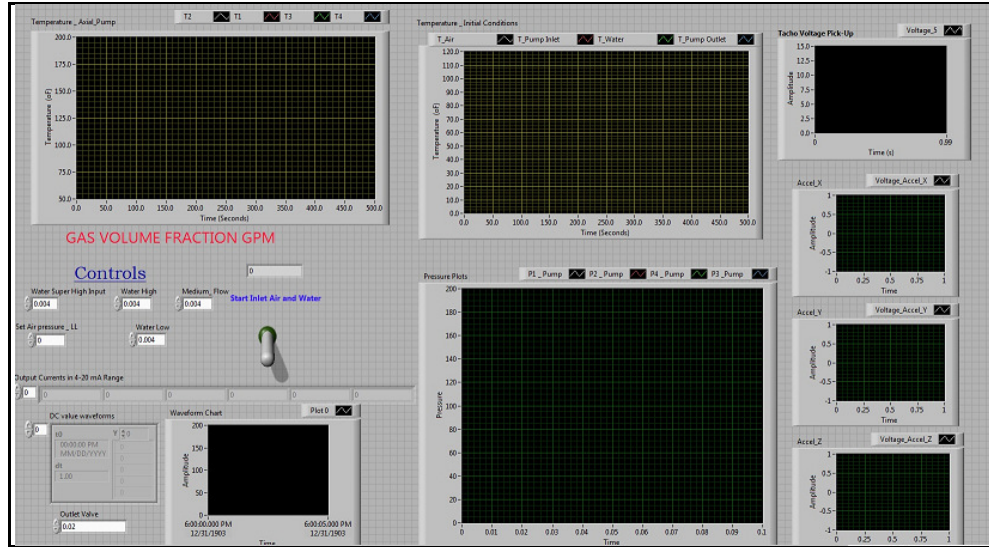
Figure 4.17 : GUI for MPP rig control.

4.3.2 Temperature Sensors

Omega T-Type thermocouples with 304 stainless steel sheath and ungrounded type were used in the experiments. $1/16^{th}$ inch and $1/8^{th}$ inch thermocouples were integrated with NI9213 with built in CJC. The thermocouples have a standard error of 1.0°C or 0.75% above 0°C 1.0°C or 1.5% below 0°C (whichever is greater).

4.3.3 Flow Meters
Air

Principle

Fluid entering the meter first passes through an inlet flow straightener that reduces its turbulent flow pattern. Fluid then passes through the turbine, causing the turbine to rotate at a speed proportional to fluid velocity. As each turbine blade passes through the magnetic field generated by the meters magnetic pick-up, an AC voltage pulse is generated. These pulses provide an output frequency that is proportional to volumetric flow. A minimum pipe length

of 10*D upstream of the flowmeter and 5*D downstream of the pump is utilized to help provide clean flow inside the flowmeter where D is the diameter of the pipe used for fluid transport. Two flowmeters were used primarily to accommodate for the total range of airflow measured.

1. High Flow : Daniel turbine flowmeter 10-100 ACFM .
2. Low Flow: Ball bearing turbine flowmeters – FTB 933 Omega 2-28 ACFM .

Output: 30 mV p-p sinewave min. signal conditioners were used to acquire data.

Water

Liquid turbine flowmeters were used with the same principle of an air turbine flowmeter. Four different flowmeters were used for the entire range of 0.75 to 650 GPM. These flowmeters were installed at appropriate locations in the water inlet manifold with the respective control valves capable of handling the specific range of water flow inlet desired. The ranges of flowmeters used are tabulated in Table 4.1.

Table 4.1 : Flowmeters used in the experimental apparatus.

Range	Type-Make	GPM Measurement
Very High	FTB: 933- Omega	40-650 GPM
High	Daniel Industries	25-250 GPM
Medium	FTB-1425 - Omega	5-50GPM
Low	FTB-1425- Omega	0.75-7.5 GPM

4.3.4 Control Valves

Masonneilan Camflex rotary control valves were used with a electro-pneumatic control to attain desired flow levels in the system. These were controlled by 4-20-ma NI-9265 modules. The air flow control valves were controlled using a PID loop to hold the air pressure at the desired level.

4.3.5 Speed Sensor

An Omron E3X-A11 NPN fiber photoelectric sensor with 200µs response time was used to measure the RPM of the pump. This was done by acquiring frequency of reflection of incident light on a reflective tape glued on to the exposed shaft. This data then was processed in LabVIEW to obtain time difference of subsequent signals. This measurement was key to verifying that the pump RPM did not change with load.

4.3.6 Accelerometers

A tri-axial (Y356M135) PCB piezo-electric accelerometer (Figure 4.18) was used in order to monitor pump vibration characteristics. The sensor was mounted on the non-rotating part of the bearing close to the suction side of the pump. This was done to investigate more into the characteristics of pump vibration and rotor imbalance at suction side when operating at low differential pressures.
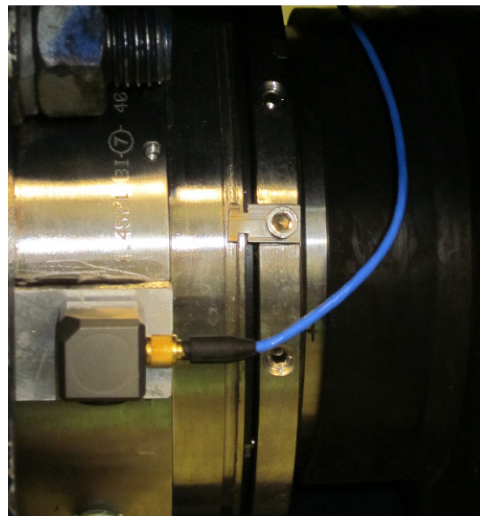
Figure 4.18 : Tri-axial accelerometer.

4.3.7 Data Acquisition

Several National Instruments modules were used to acquire data as well as to control the flow in the system. The modules NI-9205, NI-9215, NI-9213, NI-9265 were integrated on a common NI-9172 cDAQ module (Figure 4.19) and programmed in LabVIEW 2010. The data was mostly acquired in the form of analog signals which were then converted to digital data in the respective ATD convertors to input the data in to the computer. The sampling rate of data was 1000 samples/second.

A **NI-9205** ATD convertor was used for pressure sensors used to monitor air pressure and pump inlet pressure as well as pump outlet pressure. The module is capable of measuring outputs in the range of ±10 V for 16 differential channels with a 16-bit resolution. It was also used to acquire data from the variable frequency drive, accelerometers and the photoelectric sensor. As opposed to **NI-9205** a **NI-9215** convertor was used exclusively to monitor pressure on the axis of the pump. This had the capability of simultaneous data acquisition which allowed study of the internal pump pressure transients.

NI9213 ATD convertor with a built in cold junction and a 1200 S/s (aggregate) capability was used to acquire thermocouple data.

NI9265 4-20 mA used to control the Masonneilan valves for flow control. The modules were integrated in LabVIEW to implement open or closed loop controls. These modules with high sampling rate facilitated successful implementation of real-time PID control for air flow.

4.3.8 PID Pressure Control

The pump performance was investigated for 3 different suction pressures. Maintaining a constant inlet pressure was critical to testing the pump for the given differential pressures. A closed loop PID control system was implemented in LabVIEW which integrated the control valve and the pump inlet pressure transducer using the PID and fuzzy logic toolkit by

National Instruments. Autotuning of the gain constants was done for each suction pressure to obtain precise values for the gains.

Water flow on the other hand was implemented by an open loop system to set the flow rate to a constant value. Figure 4.20 illustrates the LabVIEW code used to control the respective flow rates and pressures in the pump.

The list of sensors, the underlying principle and a brief specification is listed in Table 4.2.
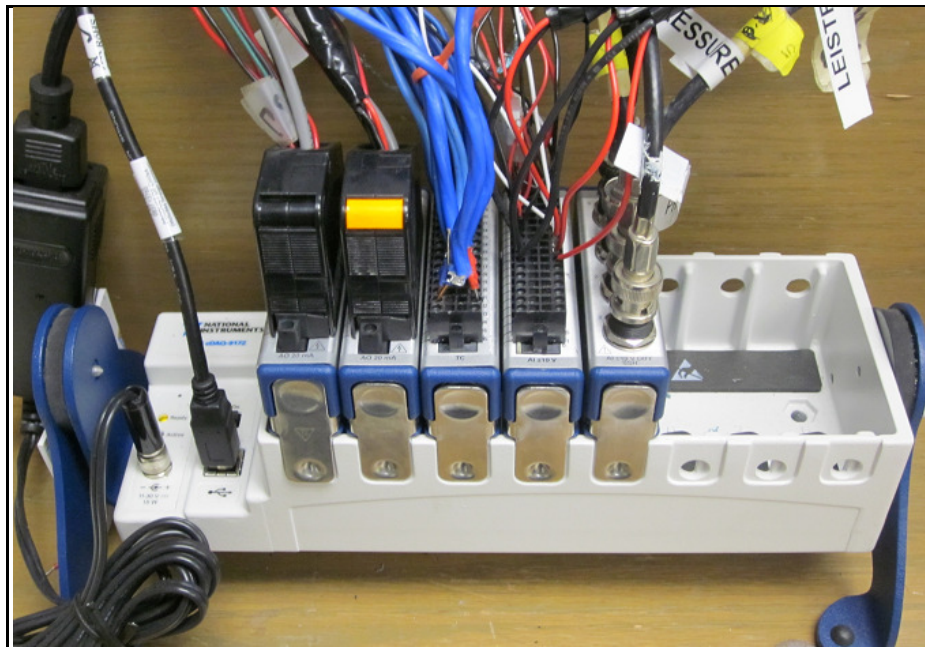
Figure 4.19 : NI-9172 cDAQ module chassis.
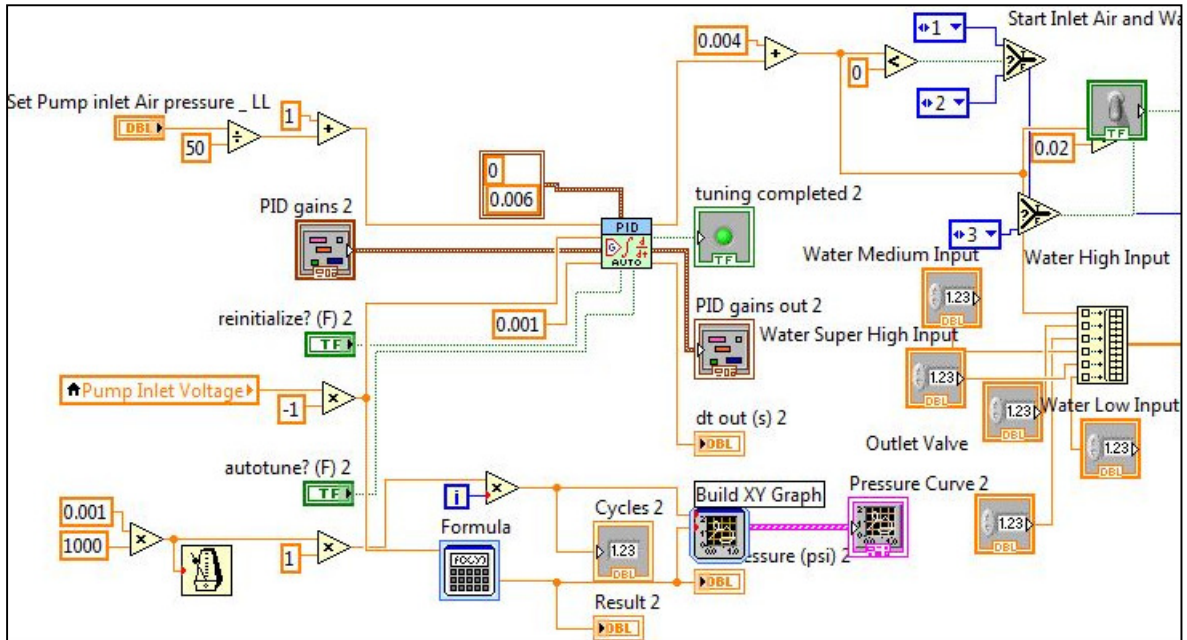
Figure 4.20 : PID and flow rate control algorithm.

4.3.9 Gas Volume Fraction Calculations

The gas volume fraction was calculated on a real time basis in the LabVIEW code which simultaneously controlled the flow rates and also acquired the data from the rig. Figure 4.21 shows the code where local variables were used to track the system parameters and used to calculate the GVF. The inlet volumetric flow rates determined the GVF. A sample calculation that shows the entire process has been shown in Appendix A.
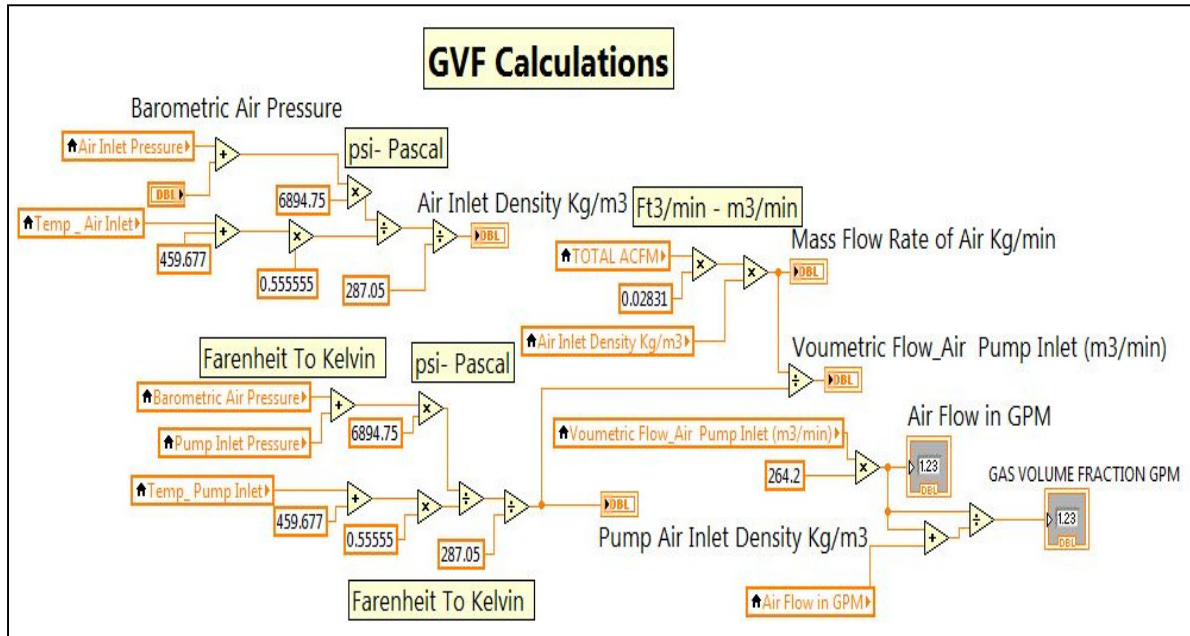
Figure 4.21 : Real-time GVF calculation in LabVIEW.

Table 4.2 : Sensor details used in the rig.

Sl. No	Symbol	Measured Quantity	Principle	Type/Manufacturer
1	P_a	Pressure – Air Inlet	Solid State	Omega- PX 481 series
2	P_i	Pressure– Pump Inlet		
3	P_e	Pressure – Pump exhaust		
4	P_d	Pressure – Pump Exit		
5	P_i- i=1-4	Pressure – Axial position on Pump		
6	T_a	Temperature – Air Inlet	Peltier Effect	Omega-T type Ungrounded
7	T_i	Temperature – Pump Inlet		
8	T_e	Temperature – Pump exhaust		
9	T_d	Temperature – Pump Exit		
10	T_w	Temperature – Water Inlet		
11	T_i- i=1-4	Temperature – Axial position on Pump		
11	Q_{w1}	Flow-Water-Super High	Turbine Meter	Omega FTB-111 Range- 40-650 GPM
12	Q_{w2}	Flow-Water-Super High		Daniel Range- 25-250 GPM
13	Q_{w3}	Flow-Water-Medium		Omega FTB-1425 Range – 5-50 GPM
14	Q_{w4}	Flow-Water-low		Omega-FTB 1425 Range-0.75-7.5 GPM
15	Q_{a1}	Flow- Air High	Turbine Meter	Daniel Range-10-100 ACFM
16	Q_{a2}	Flow- Air Medium		FTB- 935 Range-2-28 ACFM
17	N	Rotational Speed	Optical Fiber Photoelectric Sensor	Omron E3X-A11
18	A_r	Acceleration – Radial(Y)	Piezo-Electric-Accelerometer	PCB –Y356M135 Tri-axial Accelerometer
19	A_θ	Acceleration – Azimuth(Z)		
20	A_z	Acceleration – Axial(X)		

5. RESULTS

This section presents the results of the current study and the interpretation of results. Section 5.1 focuses on the steady state parameters which includes volume flow rates, efficiencies, temperature and pressure build up in the stator. The transient study which emphasizes pressure and temperature variations is discussed in Section 5.2 and the last section is dedicated to discussing the vibration issues in the pump at certain differential pressures.

Table 5.1 summarizes the matrix of the tests performed to analyze the steady state conditions. The current tests were conducted for a GVF ranging from 0 to 90 % and data from Gliers's [18] test matrix (90%-98% GVF) have been used to study the pump performance in detail with more accurate efficiency calculations.

Table 5.1 : Test matrix for steady state performance study.

Speed	GVF	Suction Pressure(psi)	Δ Pressure (psi)
	0		0
157 RPM/30HZ	20	15	30
	40		60
	60	30	90
313 RPM/60 Hz	90		120
	98	45	150

It is to be noted here that in none of these studies the cooling/flush water for the seals and bearing have been taken into account for performance monitoring. This is due to the unique design of the seepex pump which allows for cooling water to circulate without entering the pump's control volume. This way the bearings are cooled without the cooling water being injected into the pump. Consequently there is no energy input into the circulating water other than that from the cooling of the bearings.

The transient studies were performed primarily to observe the pumps response to off-design conditions. In this case, the pump was subject to prolonged periods of dry running i.e. 100% GVF and the temperature profiles were studied. Also the pump was subject to surges of water which simulated real world scenarios where sudden GVF changes can be observed. The load, pressure build-up and temperature response of the pump in these cases are studied. No specific test matrix was followed in this portion of the study. The results shall be discussed on a case to case basis and interpreted based on the pump running conditions.

A different test matrix was adopted to study the vibration issues in the pump. The matrix was selected based on previous observations of vibration and the dependence of rotational speed and differential pressure. Table 5.2 shows the matrix adopted to study the vibration issues.

Table 5.2 : Test matrix for vibration measurement.

Speed	GVF	Suction Pressure(psi)	Discharge Pressure (psi)
157 RPM/30HZ	60	0	0
		10	
	90	20	
		30	
313 RPM/60 Hz		40	
	100	45	

5.1   Steady State Performance Study

5.1.1 VFD Load/ P_{drive} vs ΔP

The power consumed by the pump is a primary concern in pump selection. The load on the motor was measured as a direct output from the VFD and a linear regression was performed

in collaboration with Glier [18] to relate the VFD output to the actual power consumed. Then a curve fit was imposed to investigate into its dependence on the differential pressure. The intention of this study was to look into the variation of the load with GVF, RPM, differential pressure and suction pressure. Table 5.3 shows the values of the multiplier and constant used for HP calculation. These values were determined empirically by computing the power supplied to the motor. This was done by measuring the actual voltage and current through each phase of the three- phase motor. Hence the power was calculated based on Equation 5.1.

$$P_{drive} = a * \left(Load_{VFD\ reading}(volts) \right) + b \quad [hp] \qquad 5.1$$

Table 5.3: Constants for VFD power calculation.

Speed	a (hp/volt)	b (hp)
30Hz/157 RPM	1.01	27.89
60 Hz/313 RPM	1.45	35.45
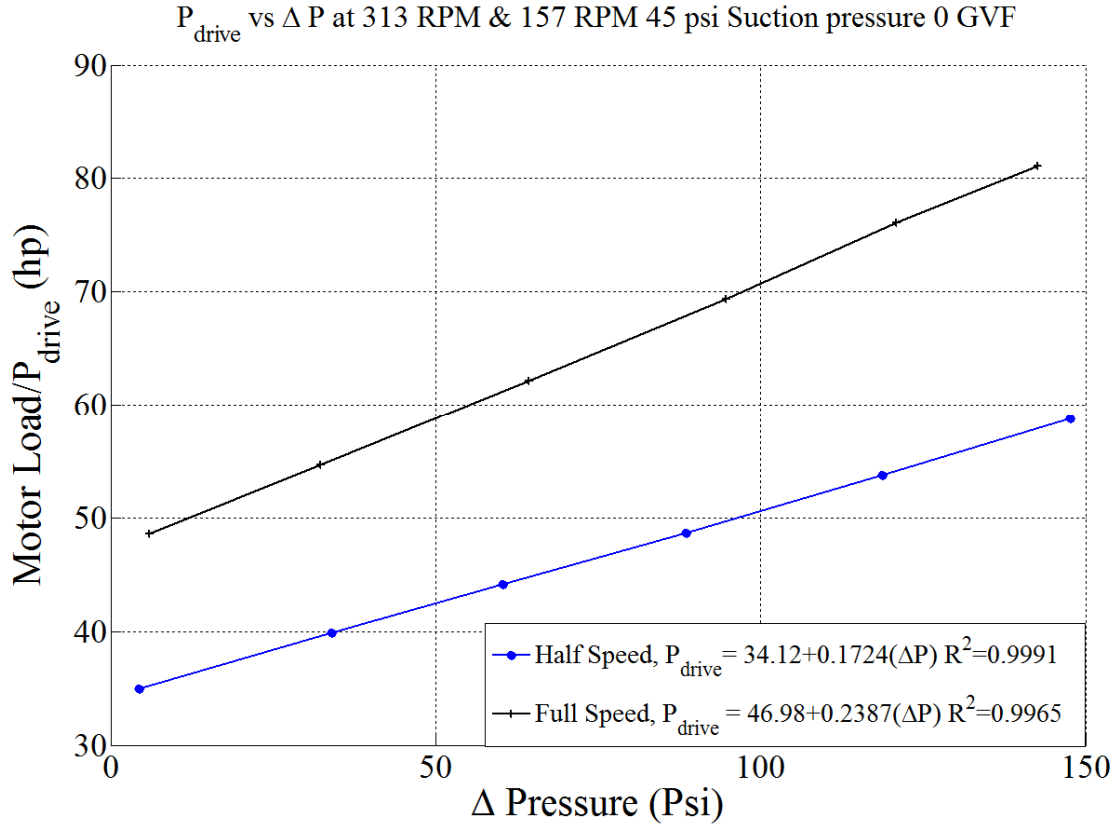
Figure 5.1 : Mechanical load variation for 0% GVF. 313 RPM and 157 RPM.

The electrical power provided to the pump as a function of pressure rise and speed of the pump for 0% GVF and an inlet pressure of 45psig is presented in Figure 5.1. The value of the intercepts for half and full speed are 34.12hp and 46.98hp. These intercepts represent the frictional drag between the rotor and stator at zero differential pressure. As the value of ΔP is increased the curve becomes linear showing a linear dependence of motor load on ΔP after overcoming the initial friction. Figure 5.2 illustrates the same dependence for two different suction pressures and the case of 0% and 98% GVF at full speed. It can be seen that the difference in load is about 1.8 hp for a change in GVF from 0% to 98%. The power consumed for overcoming friction remains fairly remains constant.
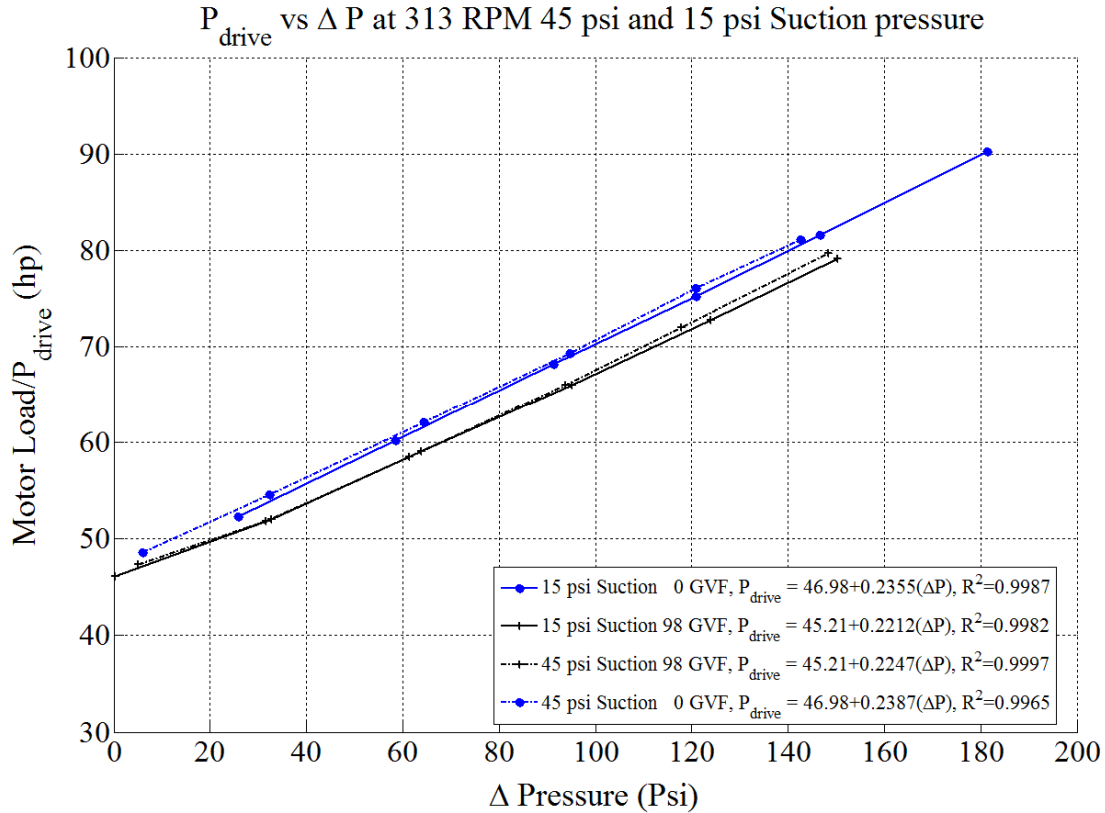
Figure 5.2 : Mechanical load variation for 0% and 98% GVF. 45 psi & 15 psi suction.

This, as discussed in Section 5.1.3, will have a great impact in how the mechanical efficiency varies with GVF and suction pressures. It can also be noticed in Figure 5.2 that the dependence of motor load on suction pressure is minimal. It can be seen that for both 0% and 98% GVF the curves lie on top of each other signifying very low if not zero dependence of motor load on GVF. This is further illustrated in Figure 5.3 for all GVFs. One can see that irrespective of the suction pressure, the power consumed by the motor remains essentially the same.

The suction pressure alters the amount of volume inlet into the pump depending on the operating GVF and this affects the mechanical efficiency. This is further discussed in Section 5.1.3 with the conclusion from this section being the independence of motor load on suction pressure and minimal dependence on operating GVF.
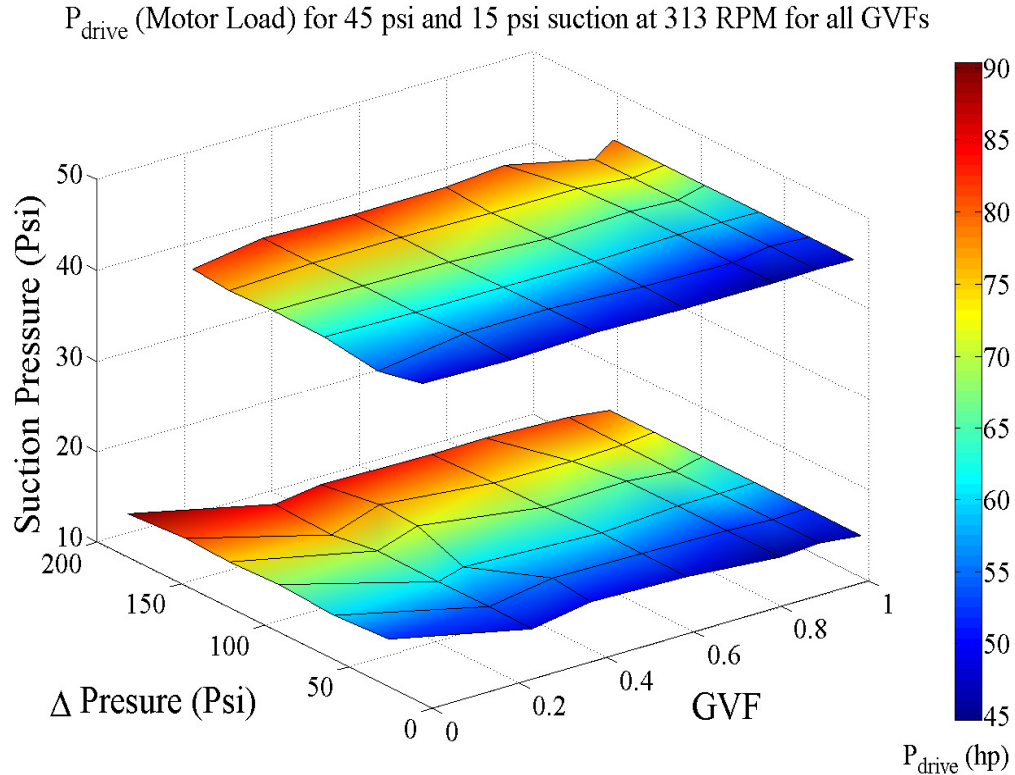
Figure 5.3 : Mechanical load variation for all GVFs. 45 psi & 15 psi suction.

5.1.2 Volume Flow Rates & Volumetric Efficiency

One of the most important parameters to be considered in a positive displacement pump is the volume displaced by it and the effect of parameters on the volume flow rate. As discussed in Section 3.1, the theoretical volume displaced by the pump is calculated based on the geometry of the pump and the speed of rotation. It was found that for a speed of 313 RPM/60Hz the seepex pump had a volumetric displacement of 576 gallons per minute.

The volume flow rate of the pump was studied and the effect of suction pressure, GVF and pressure difference across the pump was interpreted. Figure 5.4 shows the effect of ΔP on volume flow rate delivered by the pump at 313 RPM and 45psi suction pressure at all GVFs. The volumetric flow rate shows very little change in value as the pressure differential varies. Therefore, there is no noticeable slip as the differential pressure across the pump increases.

This is due to the rubber stator which ensures no clearance between the rotor and stator and hence no back flow of the fluid. There is a fluctuation in the inlet volume flow rate which follows no particular pattern. This can be attributed to the uncertainty in measuring the flow rate of the fluid which was determined to be ±5 gpm at full speed and ± 2.2 gpm at half-speed. Figure 5.5 shows a comparative plot of the flow rates at full speed and half speed. It can be noticed again that in both cases there is no slip with increasing ΔP. Also it was noticed that the flow rate across the pump for the higher range of GVFs for half speed is more than the calculated 288.25 GPM. Glier [18] addressed this issue of higher flow rates observed at half speed for higher GVFs. He came up with a relationship

$$\frac{Q_{30}(gpm)}{Q_{60}(gpm)} = 0.5233 - 0.0001(P_{suction}(psig)) \qquad 5.2$$
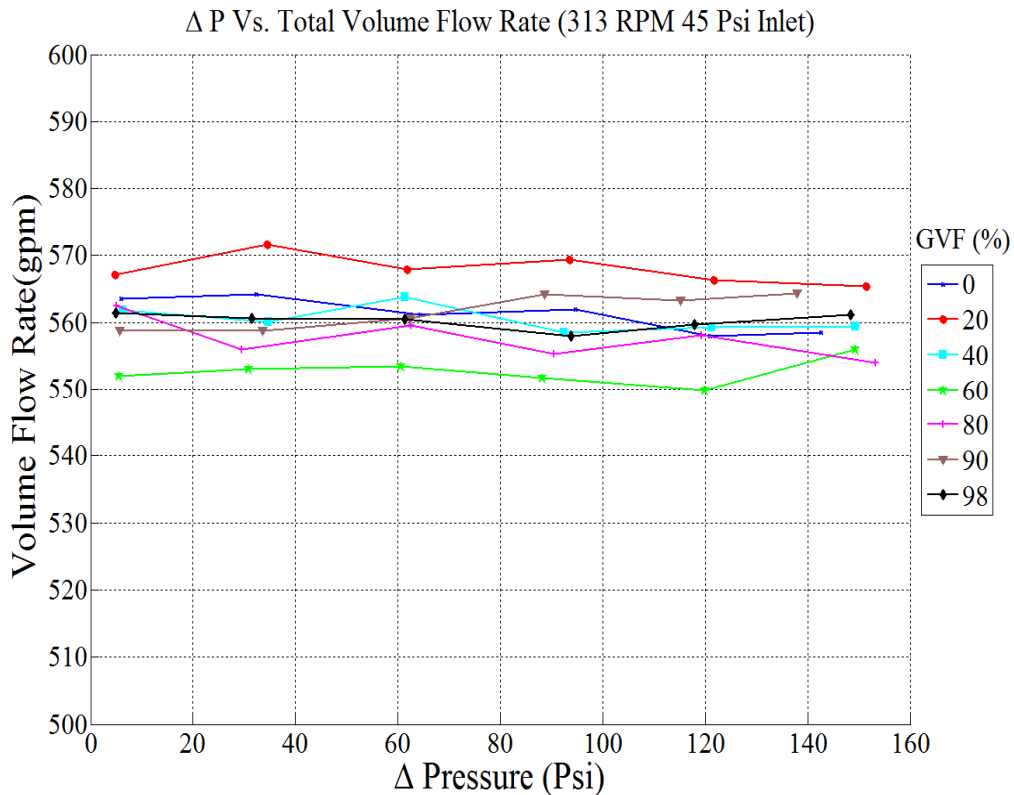
Figure 5.4 : Volume flow rate vs. Δ P at 313 RPM. 45psi Suction pressure.

This relationship has been found to be valid only at high GVFs and at lower GVFs the flow rate nears the calculated value based on geometry. The variation of flow rate at higher GVFs is discussed in detail further but it can be concluded that the flow rate of the pump is independent of ΔP as there is no slip.

As discussed earlier in Section 3.3, the slip varies inversely with the square root of viscosity in a metallic rotor and stator with a fixed clearance as studied by Gamboa et al.[7]. Reduced slip was noticed at higher GVFs. Also at a higher GVF one can expect a better sealing due to the small amounts of water. So the pump would have a better volumetric efficiency at 98% as compared to 100% due to the presence of water.
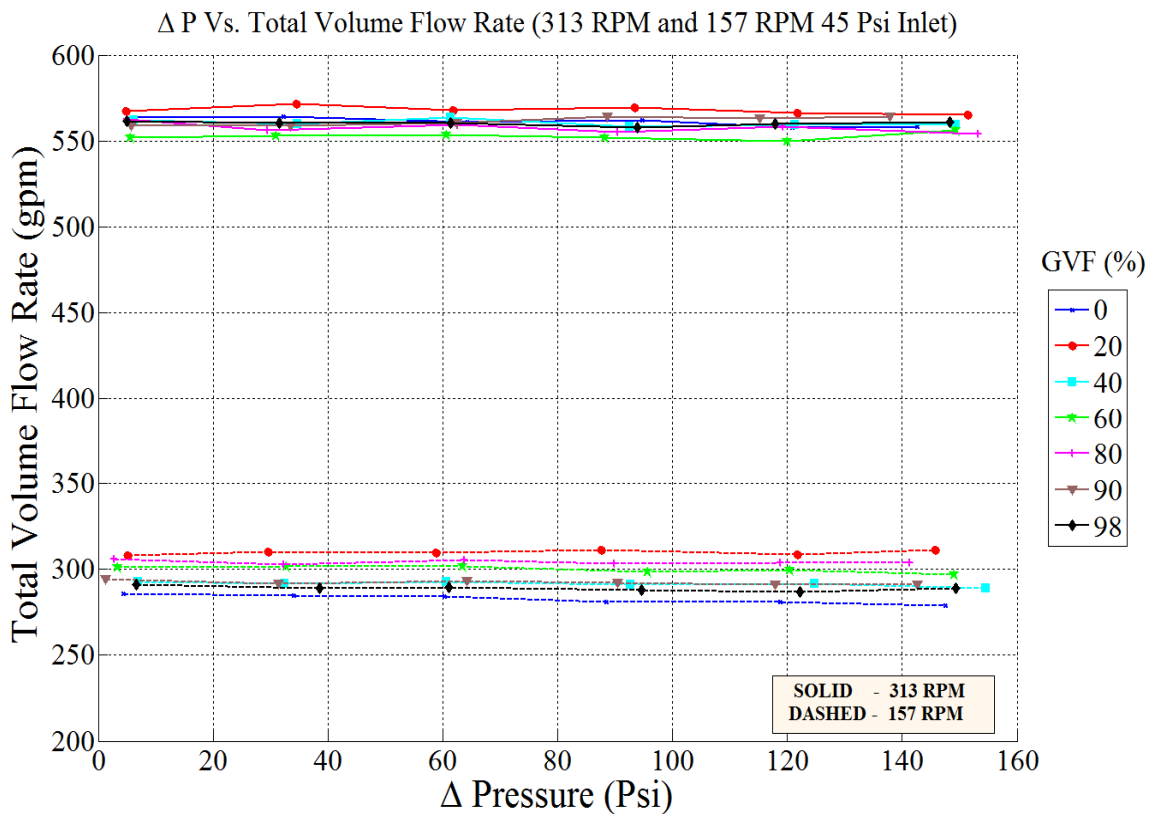
Figure 5.5 : Volume flow rate vs. Δ P at 313 RPM and 157 RPM. 45psi Suction pressure.

It has been noticed that the inlet volume flow rate is dependent on the suction pressure at high GVFs but when experimental data at low GVFs was studied it was noted that there was

no relationship between inlet volume flow rate and suction pressure. Though it was established in Glier's [18] work that the following equation governed volumetric efficiency, this relationship no longer holds for lower GVFs and particularly the 0% GVF case that has been highlighted in Figure 5.6.

$$\eta_{98GVF}(\%) = 92.119 + 0.1175(/psig)(P_{suction}(psig)) \qquad 5.3$$

A higher pressure could cause the stator to expand and hence displace higher volume through the cavities but still does not explain the fact that even at higher ΔPs there was no slip noticed for this pump and hence strengthening our initial assumption that there is zero clearance.

A linear regression was used to study the effect of suction pressure on volumetric efficiency for 0% GVF and it was found that the efficiency can be represented by the following relation.

$$\eta_{0GVF}(\%) = 98.52 + 3.89E - 6(/psig) * (P_{suction}(psig)) \qquad 5.4$$

It was concluded that there was no dependence of this parameter on suction pressure at 0% GVF. The effect of suction pressure for 98% GVF has been illustrated in Figure 5.7. It is important to understand the inter dependence of these parameters as the volume flow rates of air and water in multiphase mixtures greatly influence the efficiencies in the pump and also the pressure build-up. The efficiencies are calculated as discussed in Section 3.6. A more accurate method was used to calculate the power input to the air and a very important dependence of mechanical efficiency on GVF was noticed.
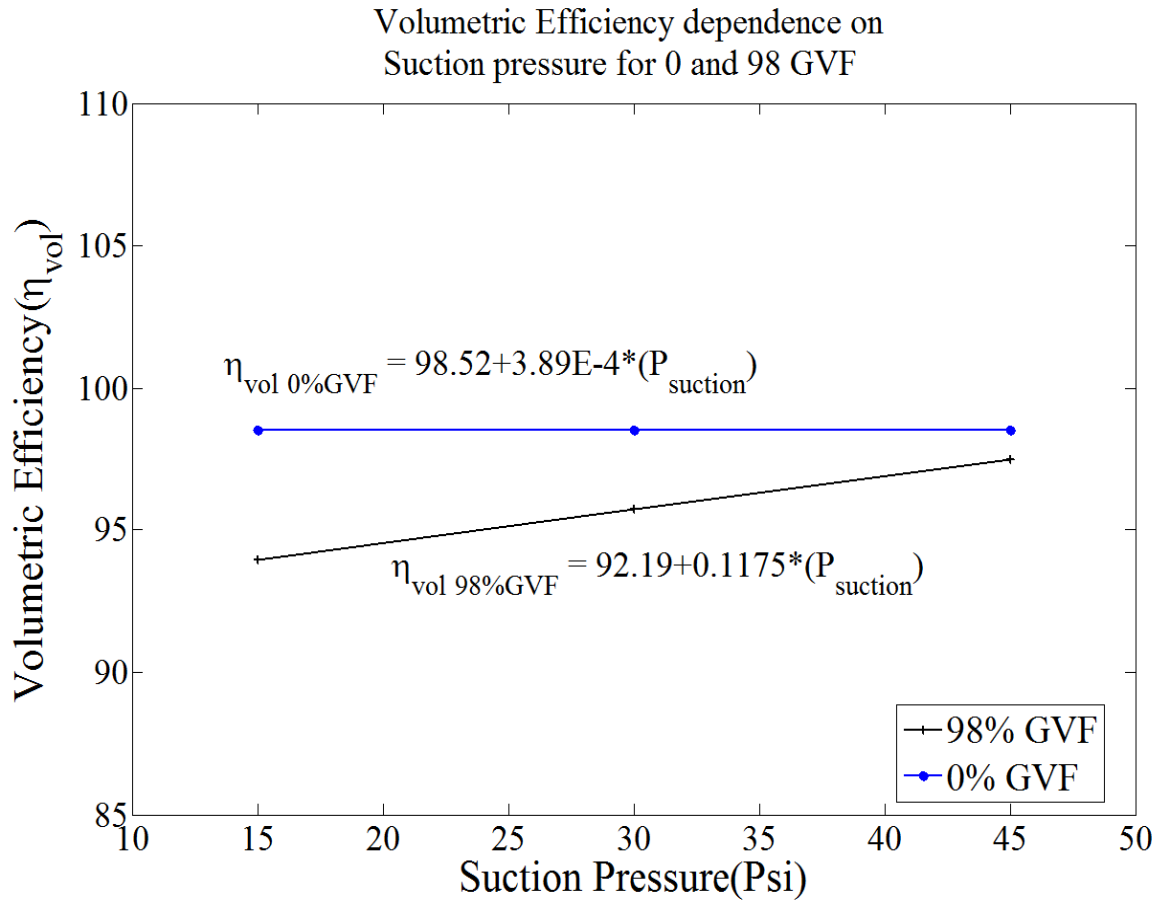
Figure 5.6 : Volumetric efficiency dependence on suction pressure. Low & High GVFs.
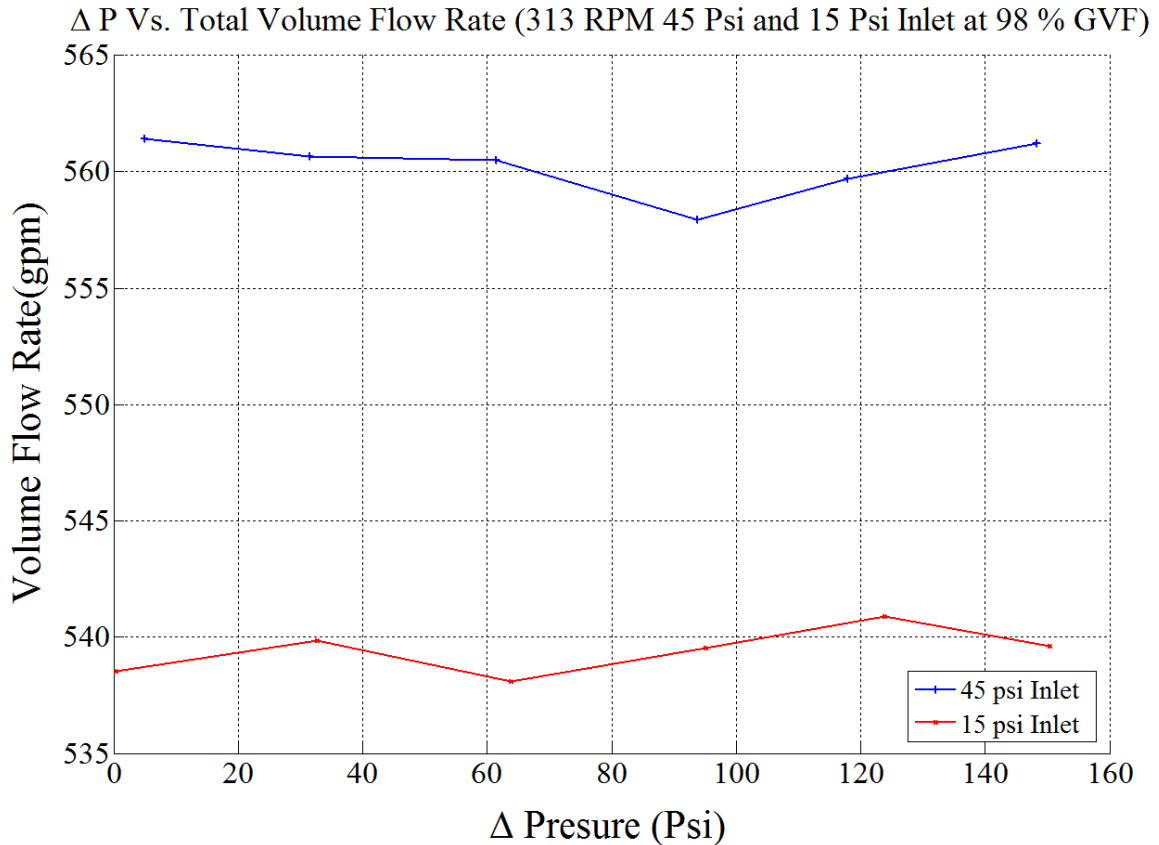
Figure 5.7 : Total volume vs. ΔP at 98% GVF.

Figure 5.8 shows the dependence of volumetric efficiency on suction pressure for all GVFs. At low inlet pressure, the volumetric efficiency at 98% GVF is the lowest observed at 92.25%. As the GVF is decreased to 20% the efficiency remains between 93% and 94%. The efficiency then increases to 98% as the GVF goes to 0%. The volumetric efficiency shows little dependence on ΔP. At the larger inlet pressure, the volumetric efficiency varies from 96% and 98% showing a minimum value at 60% GVF and maximum values at 0% and 100% GVF. At a higher suction pressure the volume of air pumped is higher and hence the volumetric efficiency increases. It can be stated that the suction pressure can have a significant impact on volumetric efficiency at higher GVFs.

When a similar comparison was made for RPMs, as illustrated in Figure 5.9 it was seen that the volumetric efficiency was high for the case of a lower RPM. This was due to a non-linear

dependence of inlet volume flow rate on RPM as observed by Glier [18]. The relationship given by him was justifying a higher volumetric efficiency at lower RPMs. As for the higher RPM case, the volumetric efficiency does not depend on ΔP as observed for the lower RPM.

$$\frac{Q_{30}(gpm)}{Q_{60}(gpm)} = 0.5233 - 0.0001(P_{suction}(psig)) \qquad 5.5$$
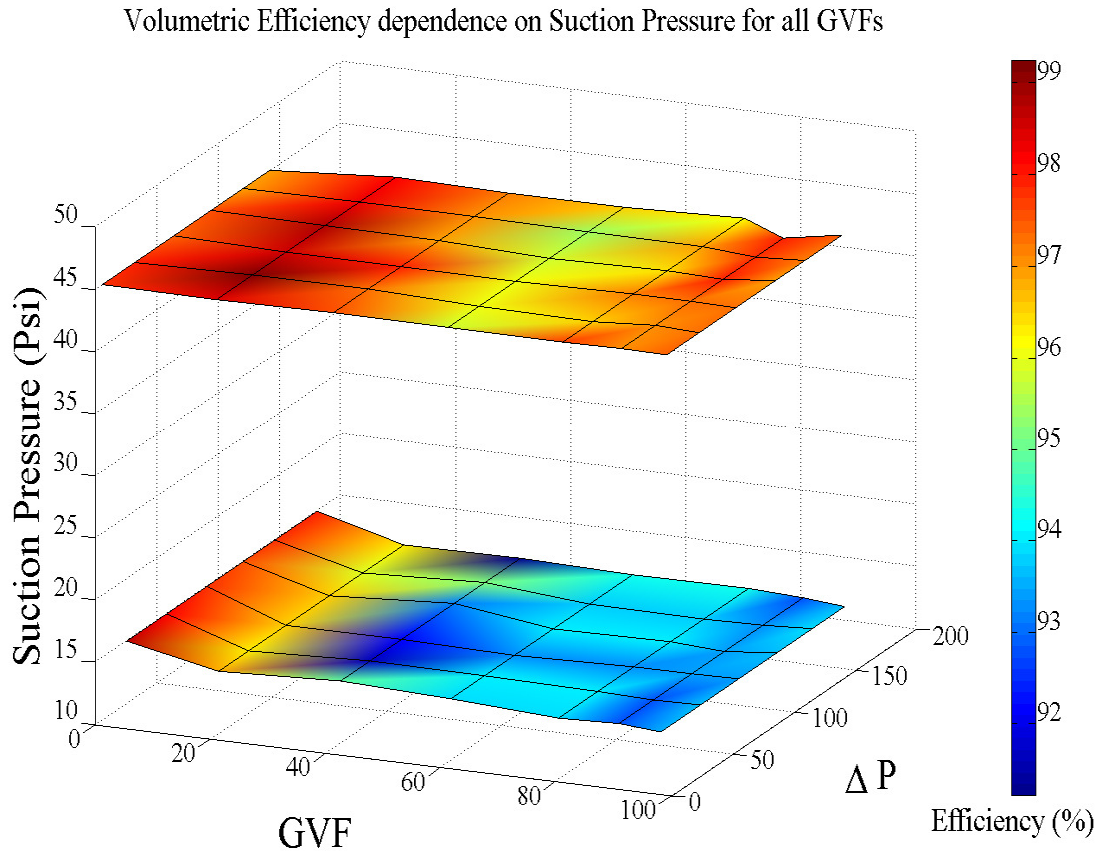
Figure 5.8 : Volumetric efficiency dependence on suction pressure for all GVFs.

These data illustrate that for a PCP only the inlet conditions of pressure and GVF affect the volumetric efficiency at a given pump speed. The pump speed has a significant effect upon the volumetric efficiency.
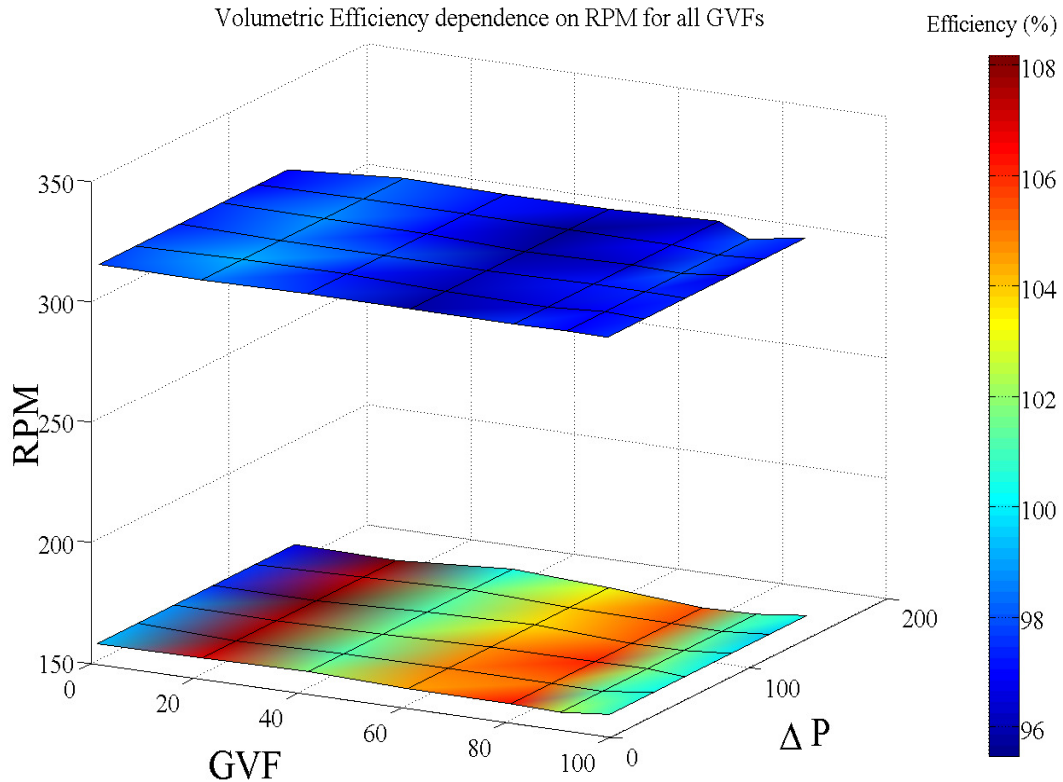
Figure 5.9 : Volumetric efficiency dependence on suction RPM for all GVFs.

5.1.3 Thermodynamic and Mechanical Efficiency

Figure 5.10 shows the dependence of mechanical efficiency upon ΔP for the entire range of GVFs assuming isothermal compression. A steep reduction in mechanical efficiency is noticed as GVF increases. At 98% GVF there is a 30% reduction in efficiency for a 150 ΔP at 313 RPM. It is interesting to note that irrespective of the GVF, the mechanical efficiency is lower than 20% for differential pressures below 20 psi. This is due to the rotor/stator drag being a set value and P_{drive} increasing linearly with ΔP. Hence at low ΔP most of the power is consumed in overcoming friction. The efficiency peaks and asymptotes at 150 psi for the high GVF case. The low efficiency at high GVFs suggests that the motor could be sized smaller if the pump is expected to run only at high GVFs. The dashed lines show the same data for half the rotational speed. Comparing the efficiencies at full and half speed the

reduction of efficiency for a given GVF reduces with increase in GVF. The half speed efficiencies are lower than the full speed efficiencies since the power required to overcome the rotor/stator drag is 73% of the full speed drag and not 50% as illustrated in Figure 5.1. However the power required per psi of pressure rise is only 72% of the full speed case. Hence the actual compression at half speed is more efficient than at full speed but the power required to overcome the rotor/stator drag dominates the compression power resulting in lower efficiencies.
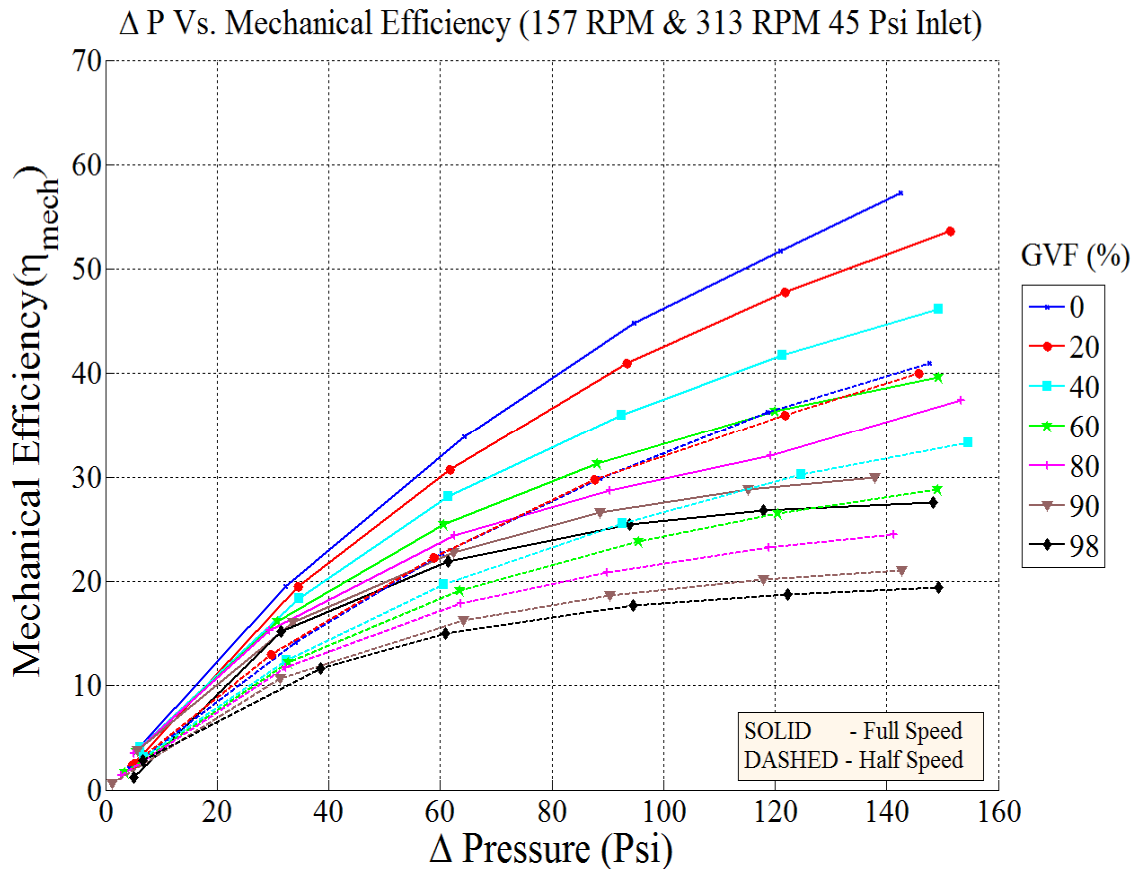
Figure 5.10 : Dependence of mechanical efficiency vs. ΔP at 313 and 157 RPM. 45 psi inlet.

Figure 5.11 shows the dependence of efficiency on suction pressure. This is directly affected by the volumetric efficiency dependence upon inlet suction pressure. One can notice that irrespective of suction pressure, the efficiency follows the same pattern for the 0% GVF but the difference becomes distinct when there is air in the mixture. The air volume displaced by

the pump depends on the suction pressure and at a higher suction pressure there is a larger volume displaced and hence the mechanical efficiency increases greatly at higher GVFs with differential pressure. This is not the case at 0% GVF due to the incompressibility of water. A significant reduction of 12.36 % is observed in the efficiency for a reduction of 30 psi in suction pressure. This difference reduces as the GVF is reduced until it gets to zero for full water. It was concluded in Section 5.2 that the volumetric efficiency is dependent on suction pressure as well as GVF as at a lower suction pressure and a higher GVF the volume flow rate of the pump is lower and this is reflected in the pumps mechanical efficiency. In conclusion, the mechanical efficiency of the pump is lower at high GVF and lower suction pressure. This is due to the reduced volume flow rate and not the change in P_{drive} as the reduction in P_{drive} for a 98% GVF compared to that of a 0% GVF case is small.
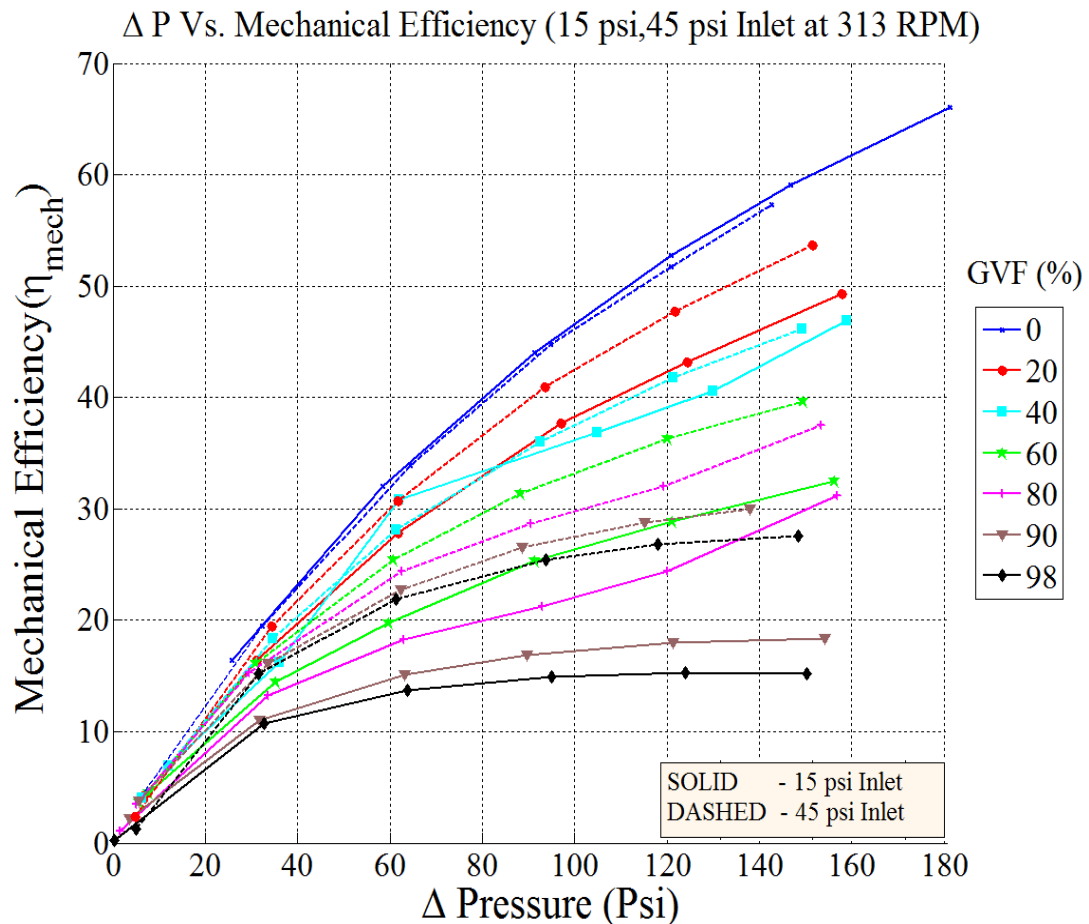
Figure 5.11 : Suction pressure dependence on mechanical efficiency.

A similar observation can be made for the thermodynamic efficiency as shown in Figure 5.12. The thermodynamic efficiency tends to reduce with increase in differential pressure. It is a measure of the ratio of the power input to the fluid to a reference power which is a measure of power input to the fluid if it were pure liquid. Hence this efficiency would be 100% for full water. Due to reduced intake of air at low suction pressure the thermodynamic efficiency lowers down to a mere 26.34% at full differential pressure whereas this value is 47.32% at 45 psi suction indicating that the pump has better thermodynamic efficiency at higher intake pressure provided it is running at a high GVF. This can be interpreted as the effectiveness of the pump as a compressor. At 0% GVF for all cases as the ΔP approaches 0 the flow is incompressible and thermodynamic efficiency is near 100% since it is incompressible. For higher gas volume fractions an incompressible nature of flow is attained with higher suction pressures and hence at higher suction pressures a better thermodynamic efficiency is observed.

It is interesting to note that the thermodynamic efficiency does not vary with rotational speed as compared to mechanical efficiency. The curves lie exactly on top of each other as shown in Figure 5.13. For all the GVFs the efficiency curve is the same starting at a very high value of about 98% and reducing with differential pressure where the reduction is higher for a higher GVF. This also confirms Glier's [18] observation of a constant ratio of flow rates at full and half speeds.
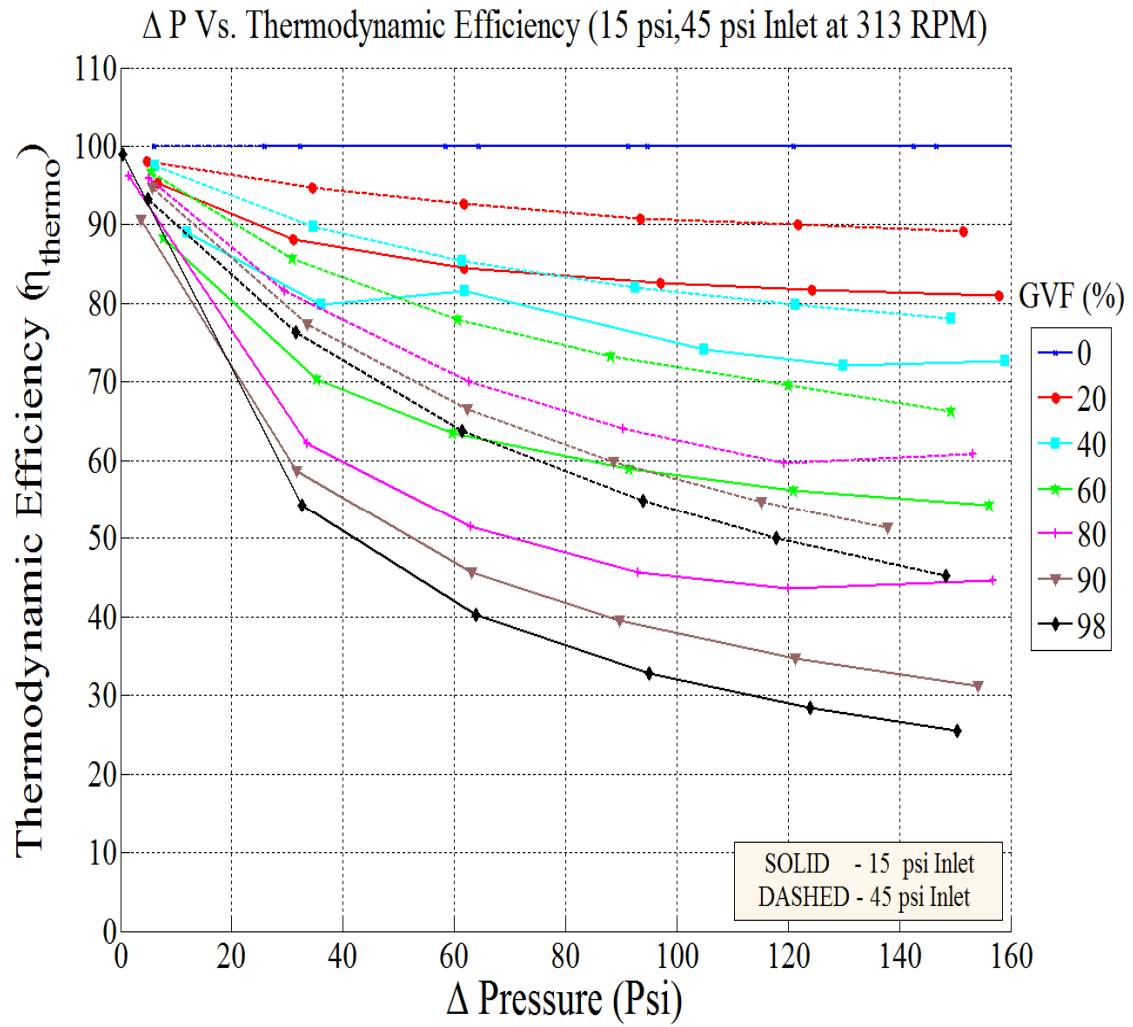
Figure 5.12 : Suction pressure dependence on thermodynamic efficiency.
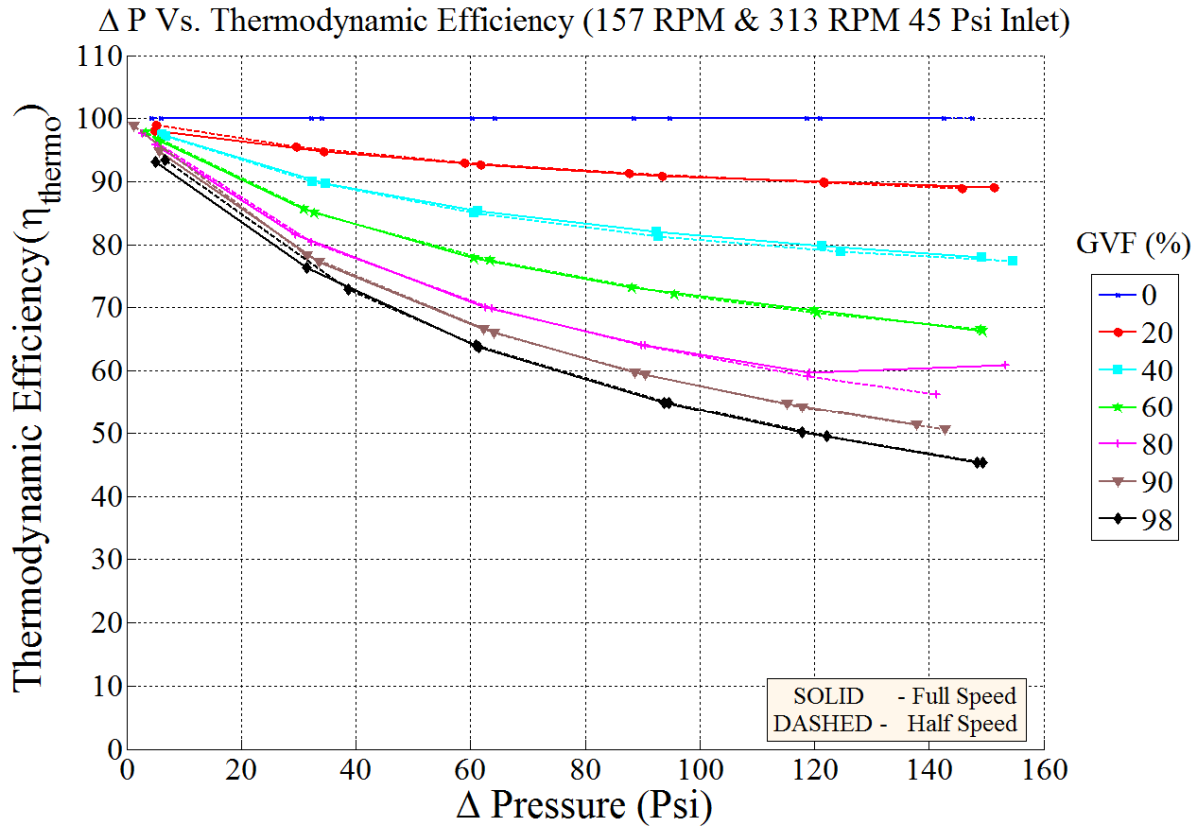
Figure 5.13 : Thermodynamic efficiency at full and half speed at 45 psi suction.

Figure 5.14 and Figure 5.15 show the comparison of mechanical and thermodynamic efficiencies for full and half speed and their dependence on half and full speed. It is obvious that the 0% GVF case has the highest efficiencies for both speeds and also the curves follow the same trends for both speeds. And one more interesting observation is that for both speeds, the efficiency seems to attain a constant value faster for higher GVFs but shows no signs of stabilizing for low GVFs indicating that better efficiencies could be expected at higher differential pressures but this could not be validated as the maximum pressure that the pump was designed for was 200 psi and any pressure above that would potentially damage the pump discharge.
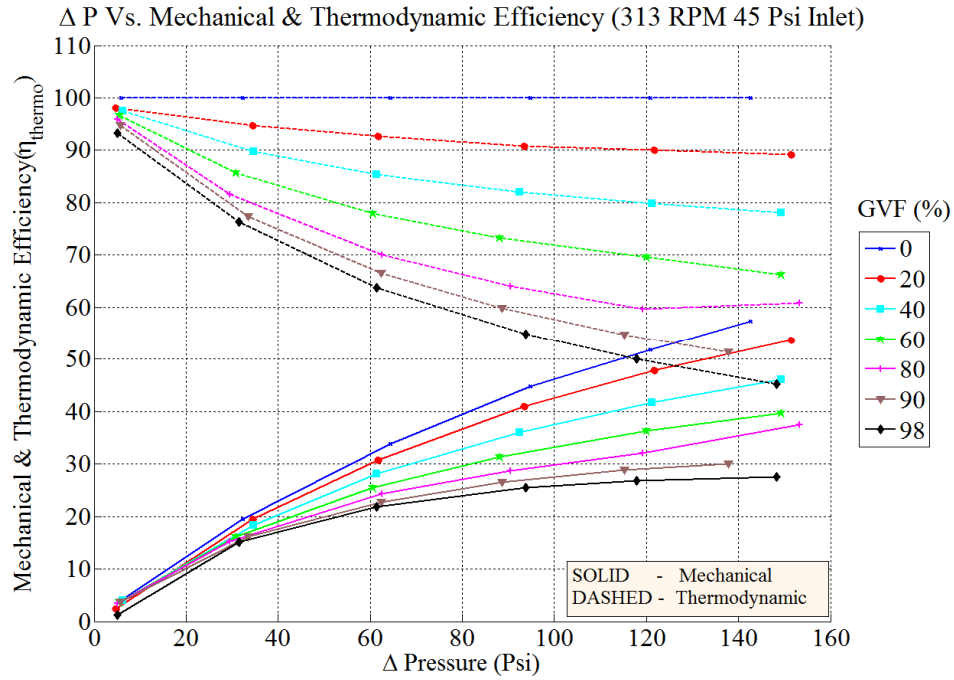
Figure 5.14 : Mechanical and thermodynamic efficiency at 313 RPM.
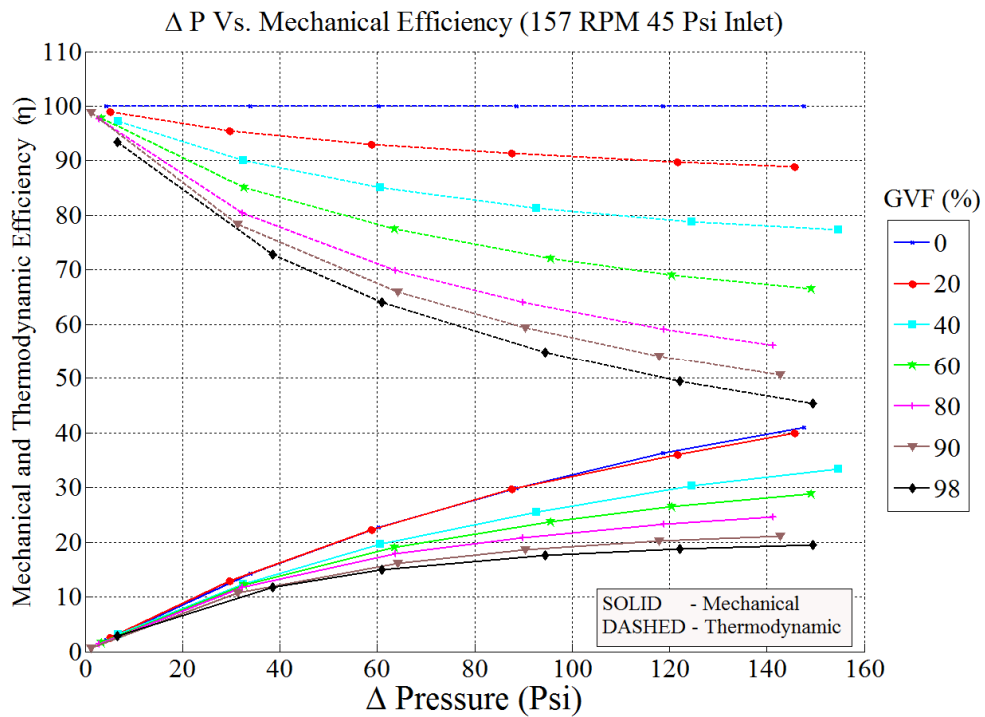
Figure 5.15 : Mechanical and thermodynamic efficiency at 157 RPM.
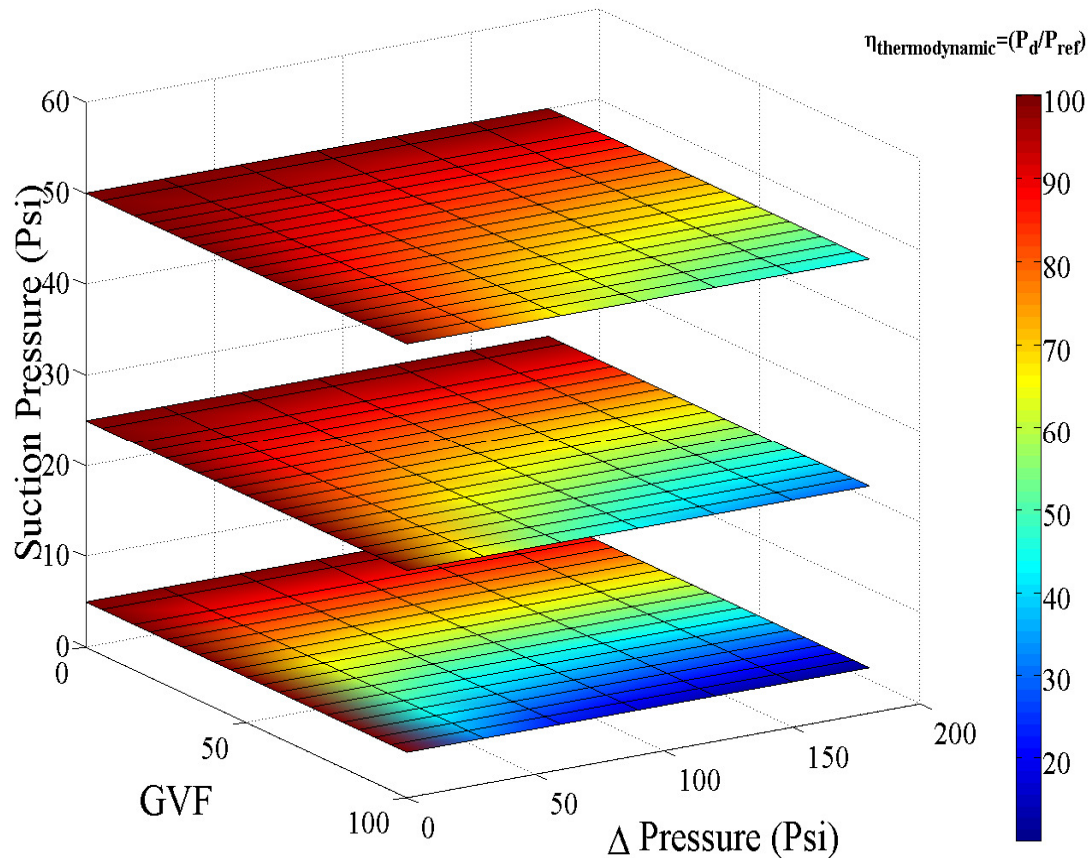
Figure 5.16 : Dependence of thermodynamic efficiency. Suction pressure, differential pressure and GVF.

Figure 5.16 shows the affect of suction pressure, GVF and ΔP on thermodynamic efficiency. This further emphasizes the importance of suction pressure and the incompressible nature of air at higher suction pressures. It is observed that at a higher suction pressure, better thermodynamic efficiency is noticed suggesting a better operation of the pump at higher suction pressures.

To summarize, a higher GVF means the pump designed for liquid is working as a compressor and hence the thermodynamic efficiency is reduced. The reduction is even larger with increasing ΔP as the gas is compressible. Hence, mechanical efficiency reduces at higher GVFs as the percentage of power used to overcome the rotor/stator friction (a constant value) decreases with increase in liquid in the mixture.

5.1.4 Pressure and Temperature Distribution

The sensors installed along the length of the stator allowed for measuring the temperature and pressure distribution across the pump stator. The data were recorded for 15 seconds and averaged over the time period to account for the fluctuations in pressure. These fluctuations were studied in Section 5.1 which discusses instantaneous pressure distributions measured locally at the stator and their significance to stator design. Axial mean pressure variations were first studied for a 0% GVF case and varying differential pressures. Figure 5.17 shows this observation at half pump speed. The pressure rise was linear through the last three stages of the stator. The first stage had a smaller pressure rise due to the time it was open to the inlet plenum. Each stage contributes significantly to the rise of the final pressure rise in the pump. This linear behavior is noticeable in Figure 5.17. Points 0 and 5 henceforth shall refer to the suction and discharge of the pump. A similar plot was made for 98% GVF (Figure 5.18) and the pressure rise was observed only between the 3rd and 4th stages. This non-linear behavior can be primarily attributed to the compressible nature of the gas. The pressure rise is only due to the back pressure present at the discharge. These observations strengthen the fact about constant volume positive displacement pumps do not generate pressure but purely react to the system change which is the discharge value in this case.
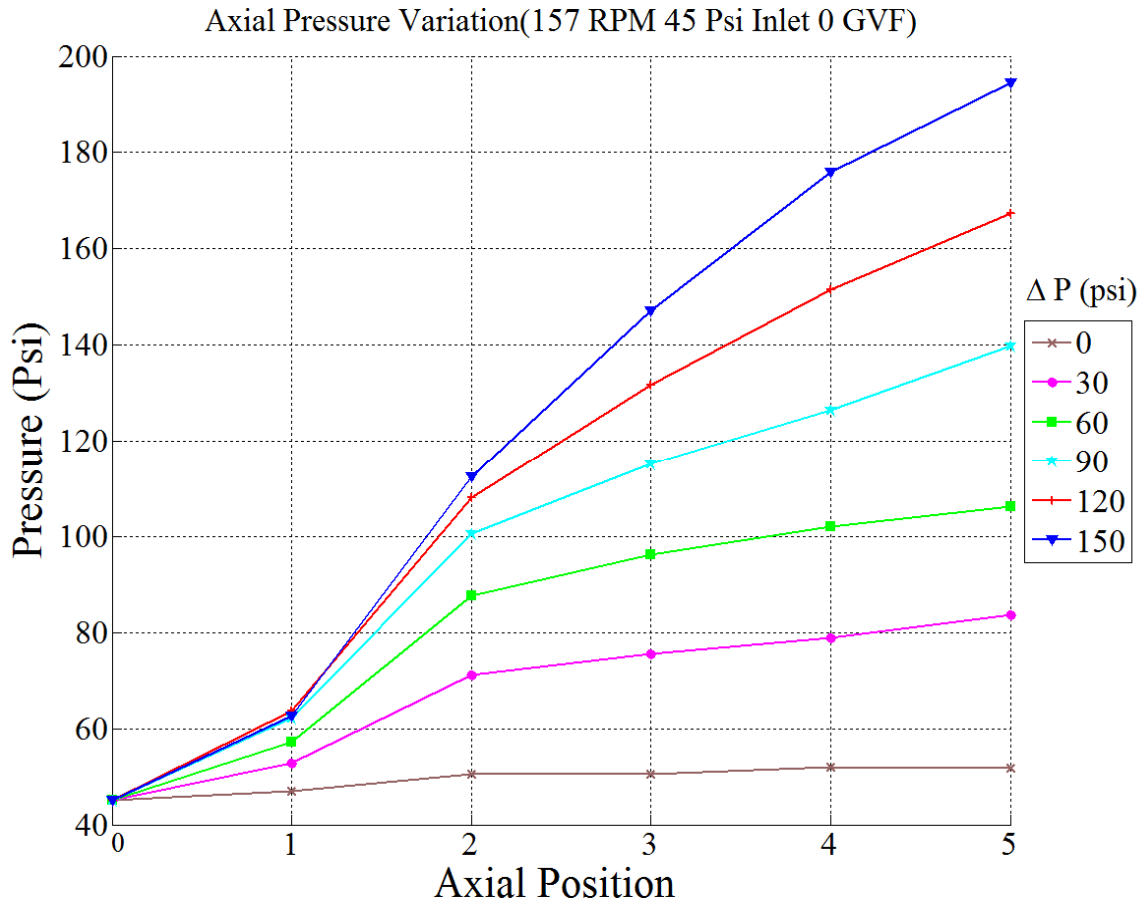
Figure 5.17 : Axial pressure variation with ΔP at 0% GVF 157 RPM.

Figure 5.19 elaborates on the axial distribution of pressure in the stator for all GVFs at full speed. At this higher speed, the pressure in the first cavity shows a larger increase as compared to the half speed case. In fact for GVFs ranging from 20% to 80% the pressure in the first cavity is higher than the second cavity. This observation can be compared at some levels in Bratu's [8] analytical model where the pressure rise is linear for the case of a 0% GVF but in case of high GVFs the pressure rise is concentrated towards the pump discharge. We can see in the plot that the pressure rise for cases above 80% GVF occurs in the last stage of the pump stator. But in case of 0% GVF the pressure rise is nearly linear across the pump. Another interesting observation here is that for low GVFs, the pressure rise is steep between the inlet of the pump and the 1st stage of compression. This is clearly noticed in cases of 0%,

20%, 40%, 60% and 80% GVFs. This cannot be explained by the current analytical model and is attributed to the sudden contraction in suction area of the pump into the first stage.
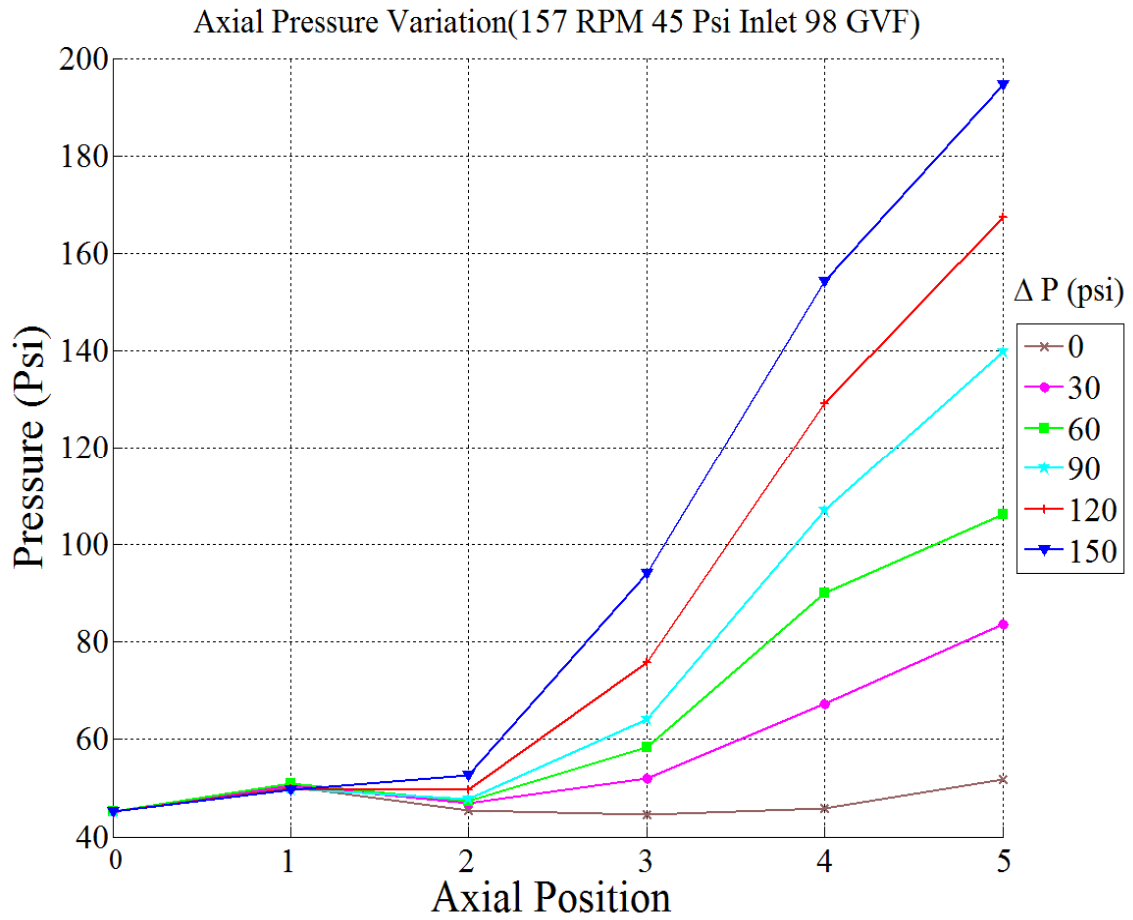
Figure 5.18 : Axial pressure variation with ΔP at 98% GVF 157 RPM.
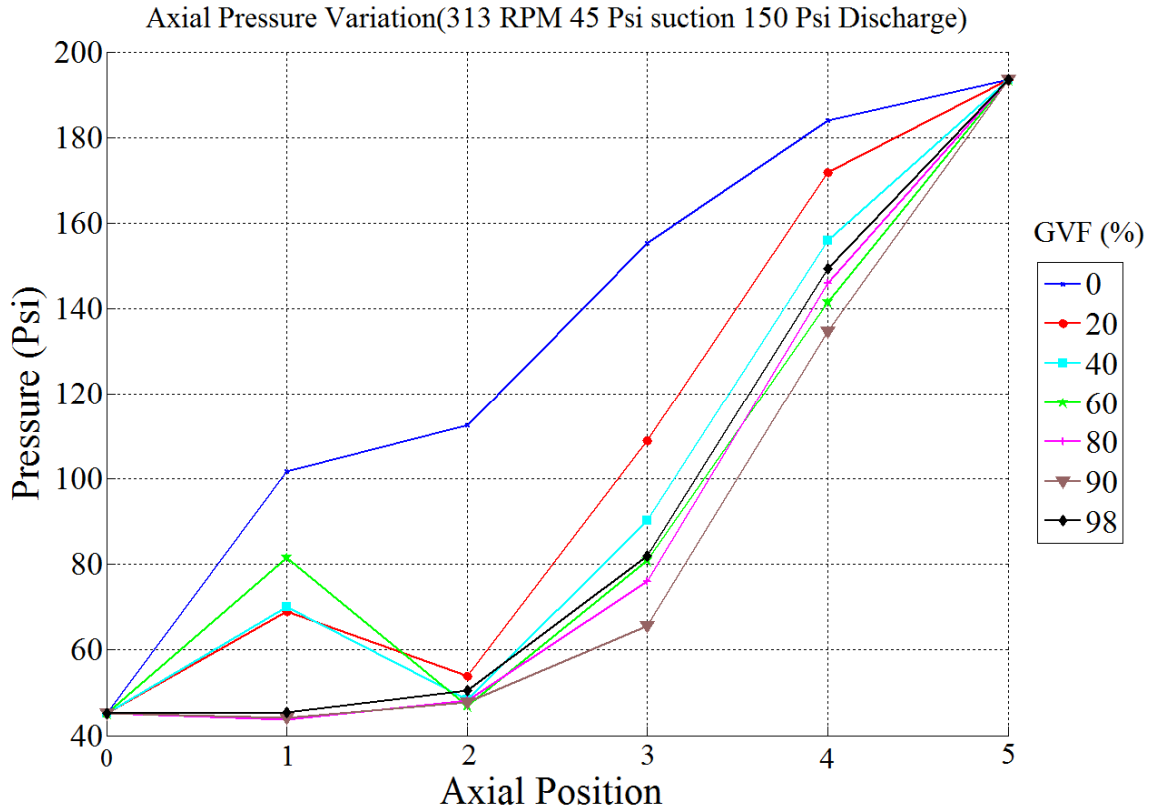
Figure 5.19 : Pressure distribution in the pump stator at 45 Psi suction. 313 RPM and 150 Psi discharge.

Though Glier [18] in his work suggests a smaller stator length, the conclusion can be valid only for high GVFs. The linear pressure rise for low GVFs obviously makes the stator length justifiable. For universality of discussion a dimensionless parameter, the normalized pressure has been introduced. It is defined as

$$P_{normalized} = \frac{P_i - P_{suction}}{P_{outlet} - P_{suction}}$$ 5.6

Figure 5.20 illustrates the normalized pressure distribution at full speed highlighting the pressure spikes at the first stage for low GVFs. This is characteristic of the full speed case. As we can see in Figure 5.21 this sudden pressure rise cannot be observed for the half speed.

This pressure spike is indicative of the speed dependence on the pressure rise of the first stage

Another interesting observation is that the exit pressure is always greater than the value of P4 but P4 oscillates from a value near P3 to the exit pressure depending on the opening and closing of the cavity 4 to the exit. That is why P4 is essentially a mean of P3 and exit pressure as shown by the linear variation from P3 to Exit pressure which is observed in most operating conditions.
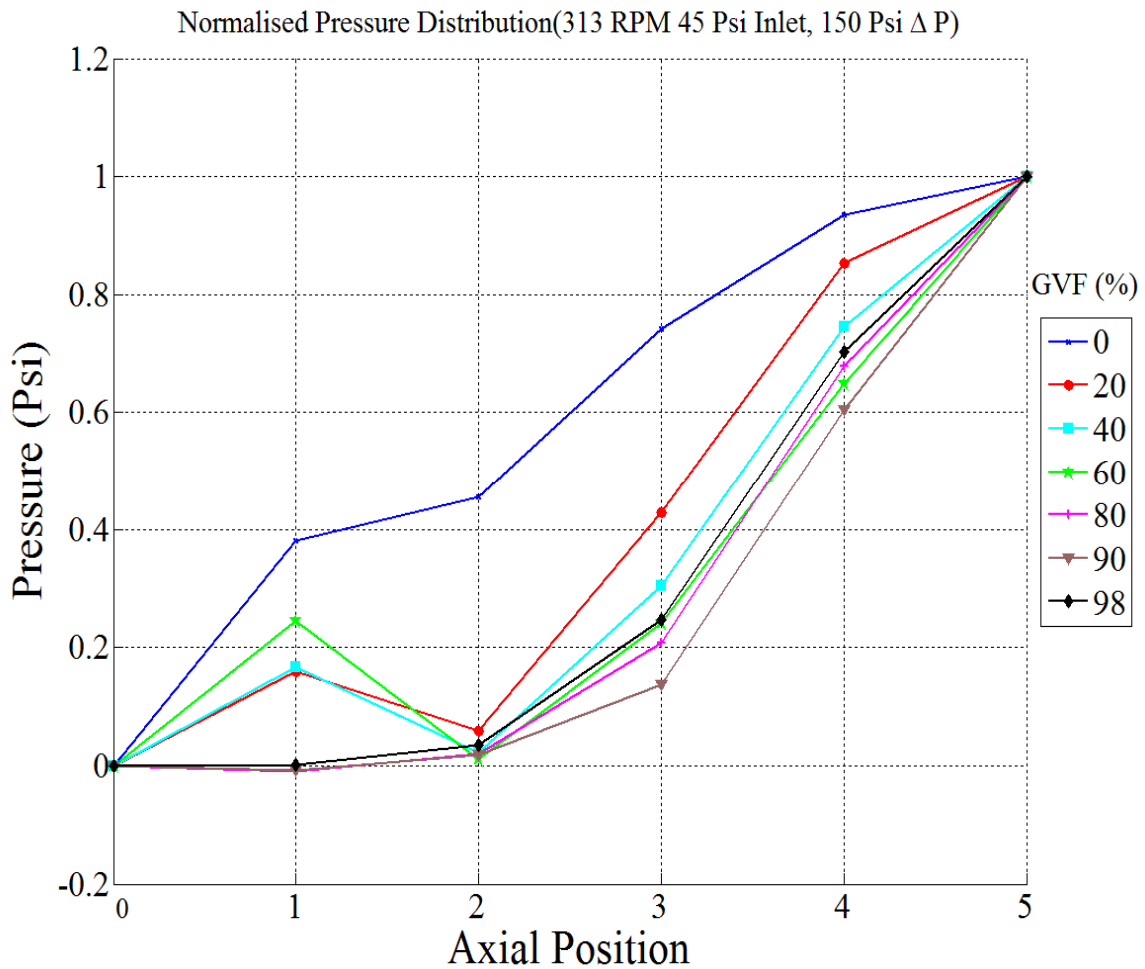
Figure 5.20 : Normalized pressure distribution at full speed.

These observations in pressure distribution do show some agreement to the analytical model developed by Bratu [8] but some observations are not in agreement. The pressure spike in the first stator is strongly suspected to be due to the sudden contraction of flow path of the fluid from an 8 inch flange to the smaller rotor side. Inlet suction area has been completely ignored in this analytical model and could be the reason for the unusual pressure spike. These pressure rises are studied in detail in the transient studies of pressure distribution. The intake pressure was always kept above the calculated critical intake pressures and was considerably low due to the low viscosities of air and water. However, since they are present only at high rotor speed, the speed at which the first cavity fills and is shut off from the inlet must have a factor in the phenomena.

Theoretically at 0% GVF and a no leakage condition the pressure rise would be observed only at the last stage when the discharge opens to the high pressure downstream. All these cases clearly indicate that the back flow is very minimal and only in the last stage of the pump. The leakage does not make it to the inlet of the pump hence maintaining a volumetric efficiency near 100% irrespective of ΔP or the GVF.

In the case of 0% GVF even a small leakage greatly increases pressure in the previous cavity due to the incompressible nature of the fluid. For any GVF>0 the flow is compressible and hence more leakage is required to increase the preceding cavity's pressure. Hence at a higher GVF the initial cavities show very little rise in pressure.
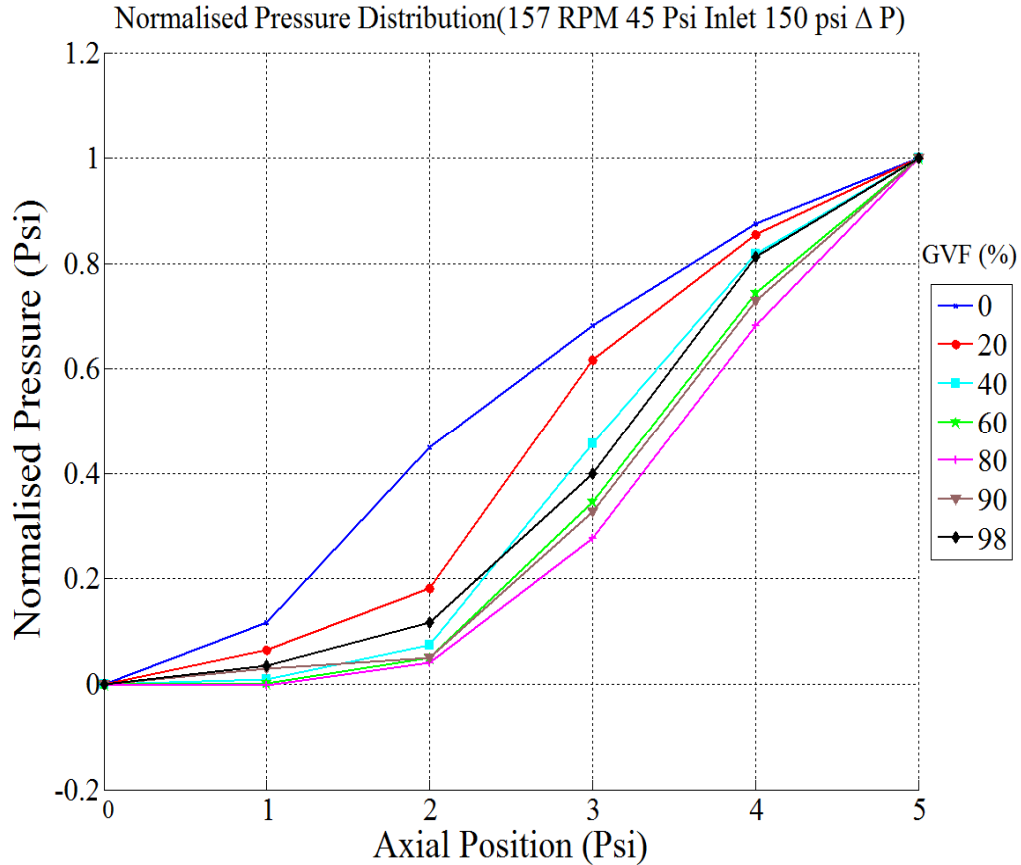
Figure 5.21 : Normalized pressure distribution at half speed.

The pressure distribution, the sonic velocity, back flow and the flow rates are interrelated. It is observed in Figure 5.21 that the pressure rise is steeper for GVFs of 60%, 80% and 90% as against the expected steeper pressure rise for 98% GVF. The backflow leakage is through a very small clearance. If the flow is incompressible, the leakage rate between all cavities is equal. Hence the pressure drop between adjacent cavities will be the same for all cavity pairs resulting in a linear pressure distribution. This is not the case for a compressible flow. In the case of air, approximately a pressure ratio of 2:1 between adjacent upstream and downstream cavities will choke the flow limiting the leakage rate. This appears to be the case for cavities 2-3 and 3-4. This is a phenomenon which can be better explained by the multiphase flow equations in choked flow conditions. The sonic velocity in a mixture is much lower than that in single phase conditions. The sonic velocity for pure gas i.e air is 1100 fps and that for pure

water is 3000 fps. For the case of a homogenous mixture, the compressibility wave velocity would be given by the expression

$$v_1'^2 = \left\{ [\alpha\rho_2 + (1-\alpha)\rho_1] \left(\frac{1-\alpha}{\rho_1 c_1^2} + \frac{\alpha}{\rho_2 c_2^2} \right) \right\}$$ 5.7

where ρ_1 and ρ_2 are the densities of the constituents of the mixture. Figure 5.22 shows the dependence of wave velocity on the GVF. It can be seen that the wave velocities can be very low for mixtures and a choked flow condition would result in a very low flow rate as compared to very high or very low GVFs. This logic helps explain that at the GVFs of 60%, 80% and 90% one can partially notice the effect of reduced flow rates. This effect would be more prominently noticeable if the pump was capable of attaining higher discharge pressures.
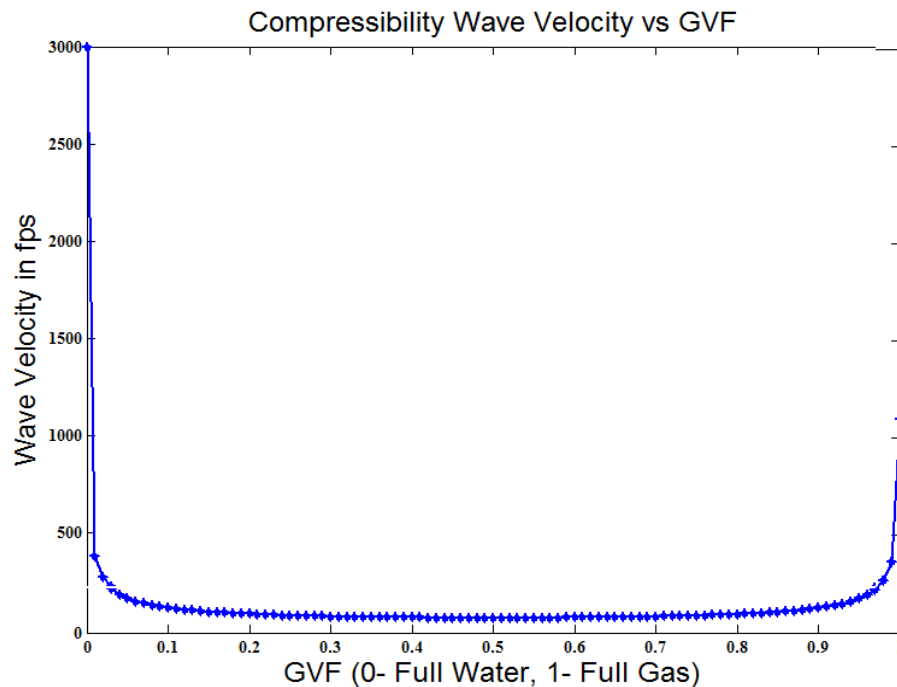
Figure 5.22: Wave velocity dependence on GVF.

The next important parameter which was studied and is of major importance to pump users is the temperature distribution across the stator of the pump. Unlike pressure measurement the temperature measurement is a little more complicated due the temperature variation across

the rubber stator. The thermocouple location and the corresponding measurement are questionable due to its location. The temperature measured is a combined effect due to the conduction from the rubber stator as well as the fluid flow across the stage. Hence the temperature measured cannot be purely attributed to a single phenomenon. Also the stator temperature depends on the rubbing friction which is more for the case of a drier mixture which again has a higher temperature after compression. This interdependence of factors motivated temperature prediction using the stator surface temperature and heat transfer model. The heat transfer model developed in Section 3.7 approximates the stator as a hollow cylinder. The convective heat transfer from the surface of the stator to the ambient air is equated to the conductive heat transfer from the rubber surface to the metal stator. This model predicts a 40^0 F difference between the interior stator rubber surface and the exposed metal surface at the highest allowable temperature the stator can be subjected to at full speed. Figure 5.23 shows the axial temperatures at different GVFs for the same running conditions at full speed. One can make several observations. Firstly, the temperature distribution seems very arbitrary at lower GVFs with no noticeable pattern but this was found to be due to its dependence on the temperature of the fluid at the pump suction.
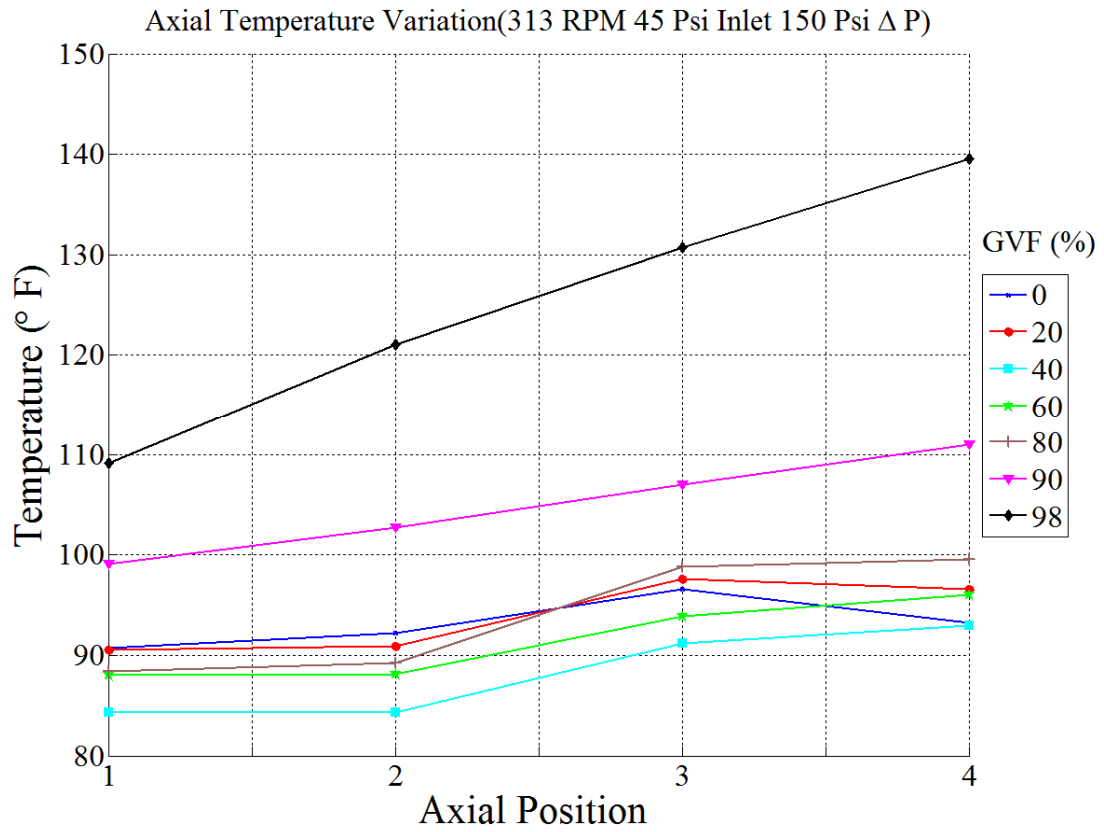
Figure 5.23 : Axial temperature distribution at 313 RPM.
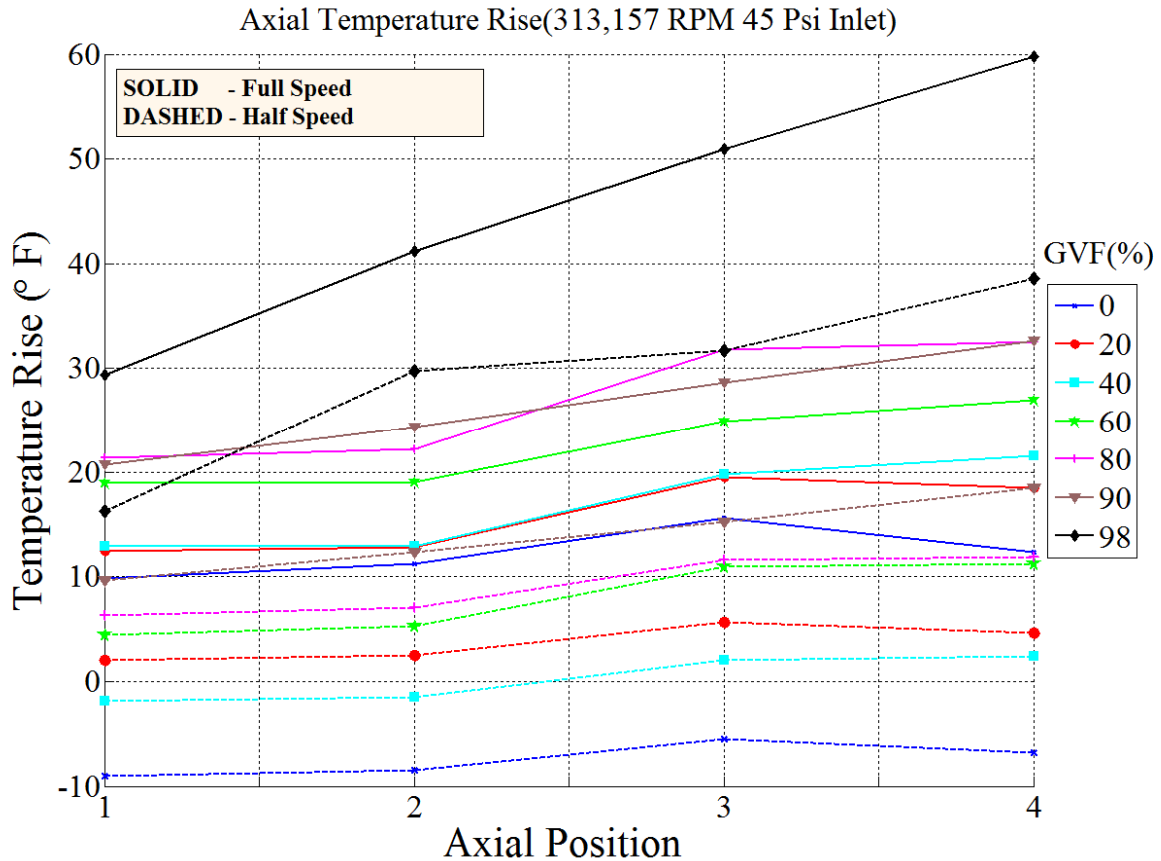
Figure 5.24 : Axial temperature rise at 313 RPM and 157 RPM.

For this reason a better parameter, the temperature rise with respect to the fluid inlet temperature was studied. Figure 5.24 shows the temperature variation with GVF. There seems to be an obvious pattern in the temperature rise, the lowest rise being in the case of a 0% GVF and the highest when the GVF was 98%. The slope of the temperature rise seems steep for the case of 98% GVF. As we discussed earlier, this temperature rise is due to a combined effect of the gas compression as well as the rubbing friction with the rotor. This can be seen clearly as the temperature of the discharge was much lower in case of 98% GVF as noticed by Glier [18] (Figure 5.25) and this measurement was purely of gas. This strengthens our hypothesis of the rubbing friction and the conduction effect to be an important contribution factor in the measured temperature.

The temperature rise of the final stage is more complicated and not explained by the existing models. Mirza et al. [19] claims of the temperature rise following a polytropic compression is obviously insufficient. Figure 5.26 and Figure 5.27 illustrate the temperature rise across the pump for different GVFs at all differential pressures. Here we notice another important contributing factor to the temperature at the final stage. The temperature also is a function of the discharge conditions. As we can see the temperature is lower at the 4th stage which is closer to the discharge temperature.
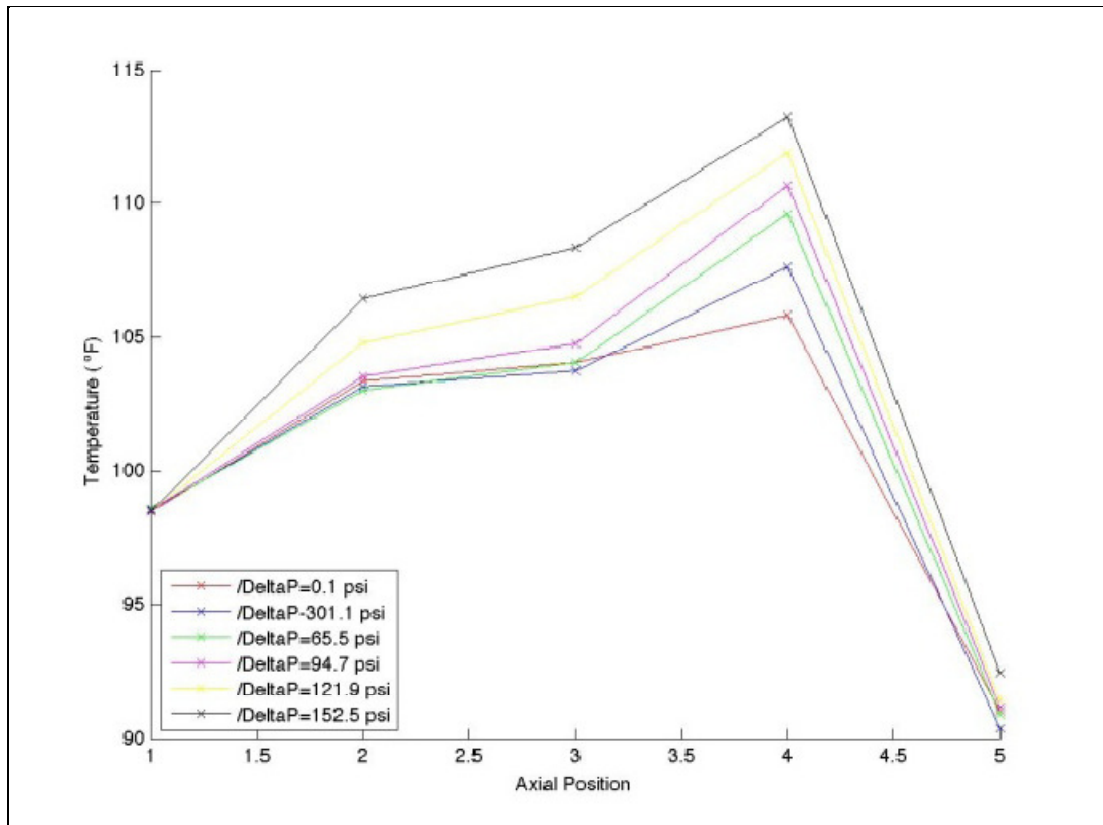
Figure 5.25 : Axial temperature distribution at 157 RPM. 96% GVF [18].

One cannot purely predict the temperature measured using one parameter. The analytical model has to take into account the speed of rotation, discharge conditions which is a function of discharge area, the GVF, the differential pressure, and the viscosity of the fluid. The temperature of the 4th stage seems to rise higher as the differential pressure increases at a higher GVF. There is a direct bearing of the GVF and ΔP on the absolute temperature. These

are fluid dynamic interpretations of the observations but from a purely manufacturer and end user point of view the only concern is the stator temperature as a high stator temperature could lead to swelling of the stator leading higher rubbing friction between the rotor and stator surface resulting in a lower mechanical efficiency(Figure 5.26 and Figure 5.27).

Figure 5.28 shows the variation of stator surface temperature with GVF and ΔP. A 40^0 F temperature difference at the highest differential pressure and GVF predicted the limiting running condition of the pump.
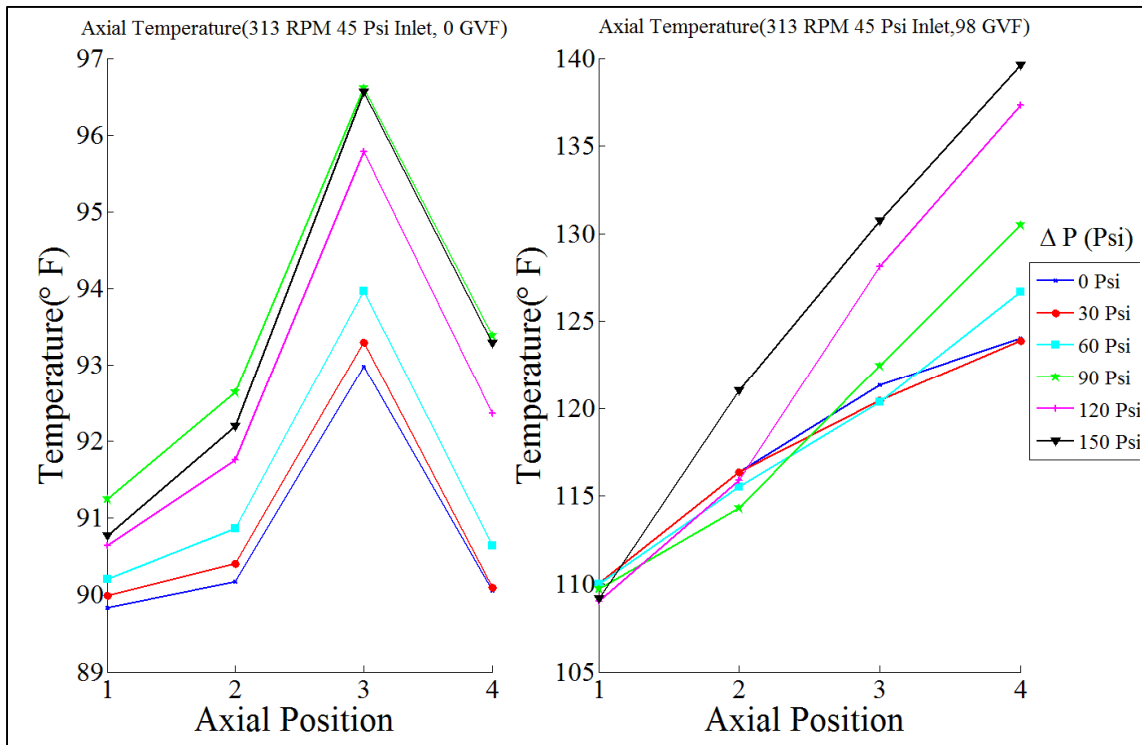
Figure 5.26 : Temperature distribution at 0 and 98% GVF.
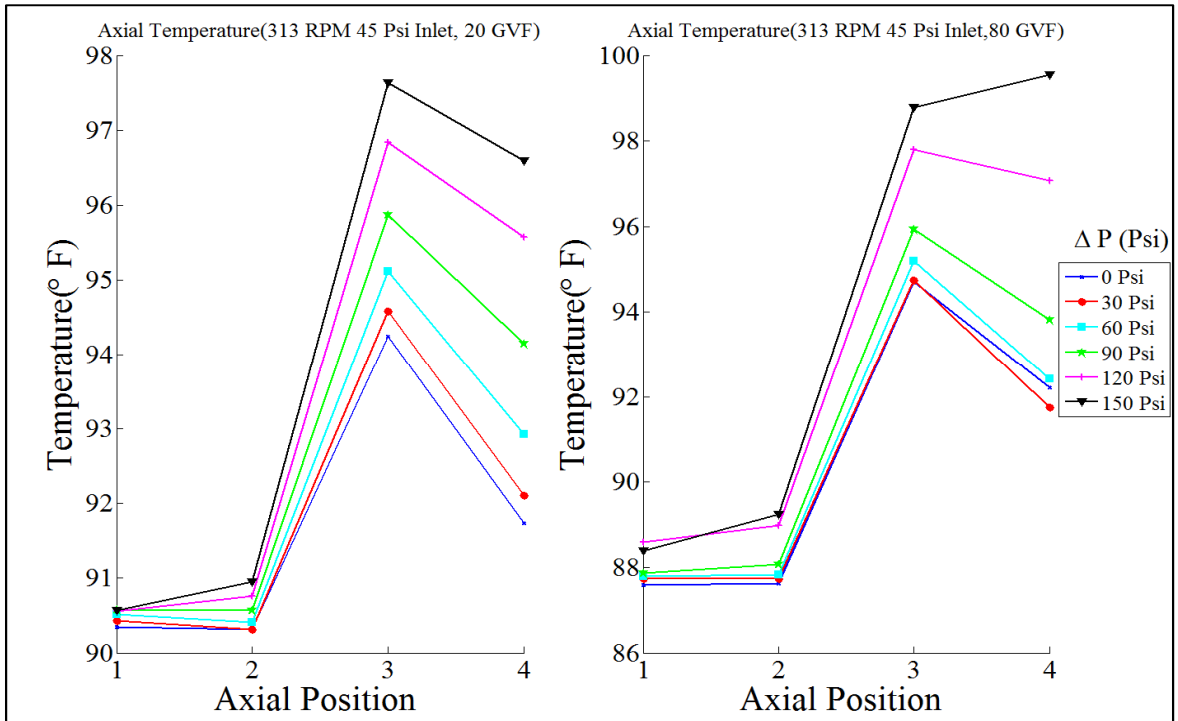
Figure 5.27 : Axial temperature distribution at 20% and 80% GVF.

But this conclusion was insufficient as the temperature rise never attained a steady value. The rubbing friction kept increasing at high GVF (96%-98%) never reaching a steady value. This deemed a transient study of the pumps response to a high GVF condition. The transient study focused on the temperature rise, the instantaneous pressure profile and also the dependence of temperature on load and rubbing friction.

Stator Surface Temperature Variation with GVF and Δ P at 313 RPM
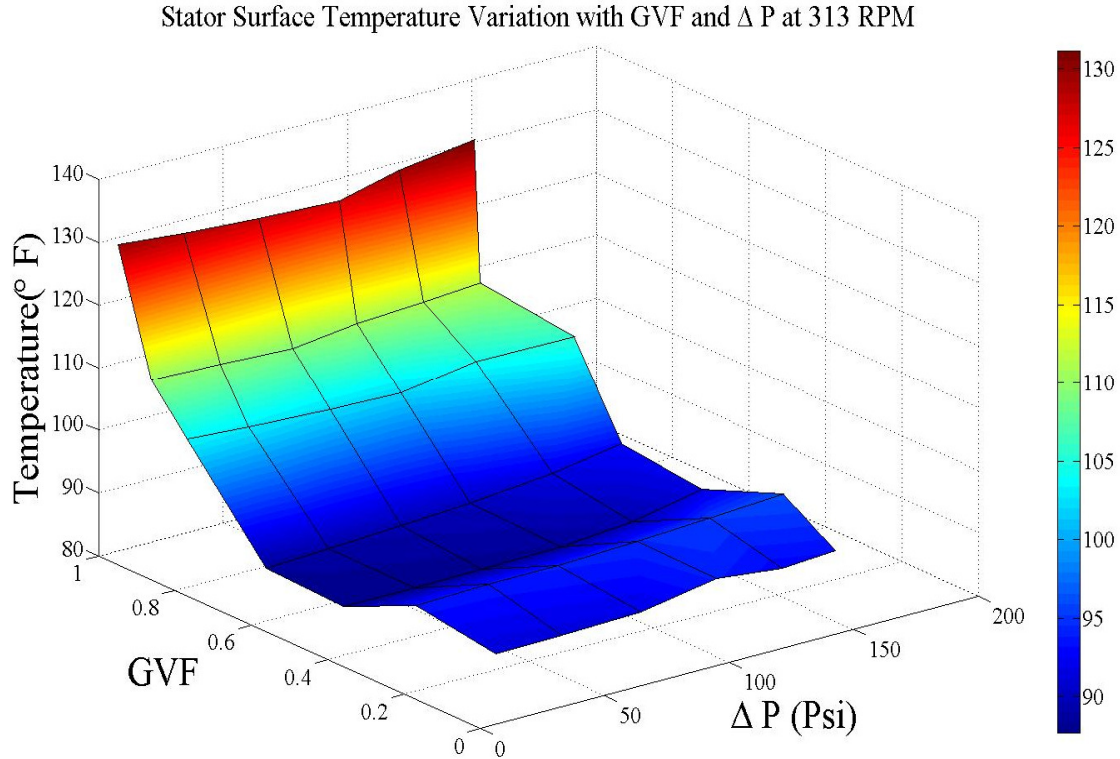
Figure 5.28 : Stator surface temperature at 313 RPM.

The co-relation obtained by Glier [18] for 90% ≤ GVF ≤ 98 % for this pump operating at full speed based on multiple regression i.e

$$T_{60} = -184.9 + 0.0792(\Delta P) + 0.1616(P_s) + 308.8(GVF) \qquad 5.8$$

would not be sufficient to predict a steady state temperature. The relations developed based on heat transfer model would give an approximation of rubber surface temperature. The following relation co-relates the stator surface temperature at the 4th stage to rubber temperature. The derivation of this has been discussed in Section 3.7.

$$T_{rubber\ surface} = T_s + \frac{t}{K}\left[\frac{CRa_D^n}{k}(T_s - T_\infty)\right] \qquad 5.9$$

where K is the effective conductivity of rubber-metal stator.

5.2 Transient Performance Study

5.2.1 Instantaneous Pressure Profiles

The pressure profiles and the pressure rise along the stator can provide valuable information in terms of pressure rise between stages, leakage between stages, the effect of compressibility on the pressure rise, and the fluctuations in pressure inside the pump. Transient data was recorded using a simultaneous data acquisition DAQ card so as to have synchronous data for all the four sensors. The sensors located at each stage of the pump recorded data at a 1 kHz sampling rate and were triggered by the photo-sensor installed at the bearing to shaft interface. Figure 5.29 shows the profiles of the 4 sensors for the case of a 0% GVF full speed condition at 45 psi suction.
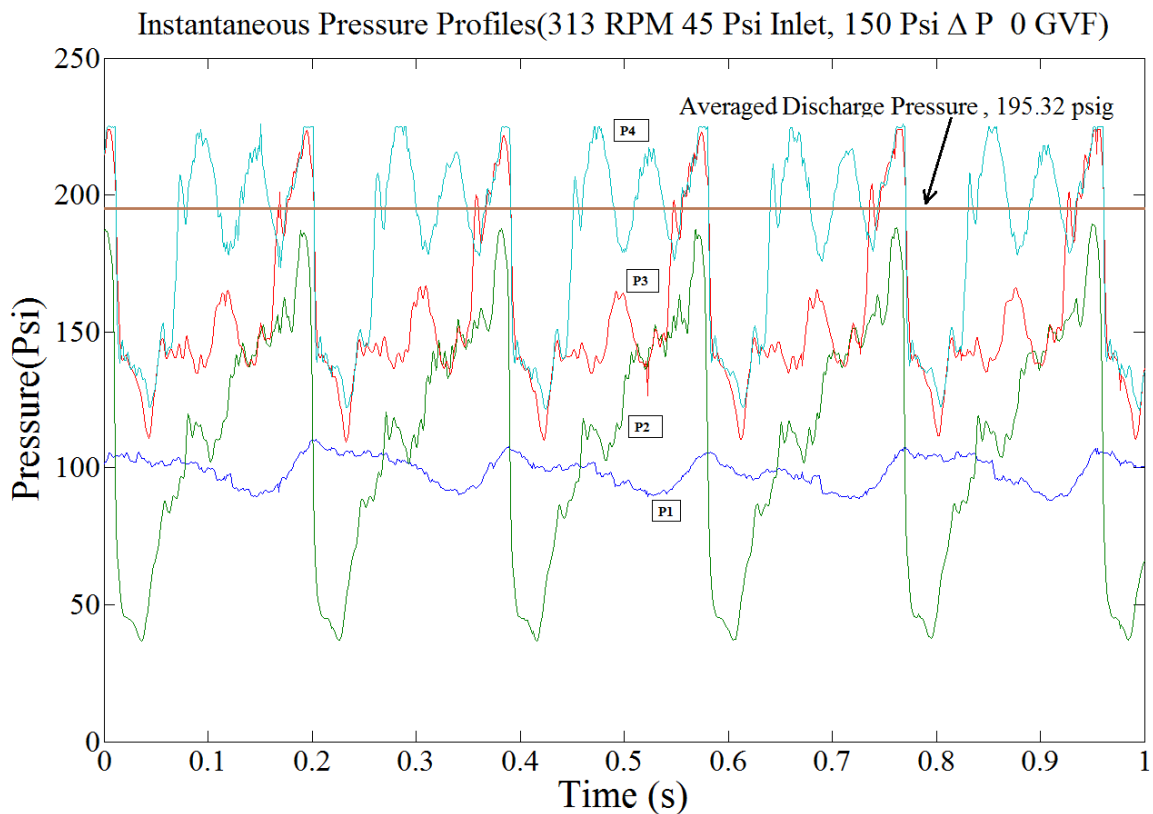
Figure 5.29 : Instantaneous pressure profiles at 0% GVF, 313 RPM.

It was observed that the pressure rise at sensor 1 was very significant relative to the inlet pressure. The difference was more than 50 Psi making the first stage very important at low GVFs. This finding is very different from those observed by Gamboa et al.[7] for a metal stator with a positive clearance. This pressure rise is observed for all GVFs less than 60% for full pump speed. This can be attributed to the incompressibility of water and the sudden contraction of fluid path area after its entry from the 8 inch flange. This is detailed for a 1 second time period for all GVFs in Figure 5.30. All GVF cases above 60% report a minimal pressure rise from 45 psi unlike those noticed by Gamboa et al.[7] who noticed this rise for all GVFs. This shows a significant dependence of pressure rise at Location-1 on rotor-stator clearance. One can only conclude that the importance of design of the first stage is very important for low GVFs and also the pressure profiles are different from the case of a positive clearance because of no leakage at stage-1.

The low pressure regions in each time trace represents the stator passing over the pressure tap. The pressure in the second and the third cavity increases with time as fluid from the downstream cavity leaks back into pressure cavity. This pressure rise is more pronounced for the second cavity. Both the third and fourth cavity pressures exceed the average exit pressure. However, the exit pressure has a large fluctuation level due to the pulsation of flow rate inherent to a positive displacement pump.

Comparing the profiles for low and high GVFs in Figure 5.29 and Figure 5.31 the first and foremost obvious observation is the non-linear pressure build-up across the stator for 98 % GVF case. Also one can notice that for both the cases, the surges in pressure are higher towards the 3rd and 4th stage as the pump responds to a constriction at the discharge. This is typical of a positive displacement pump.
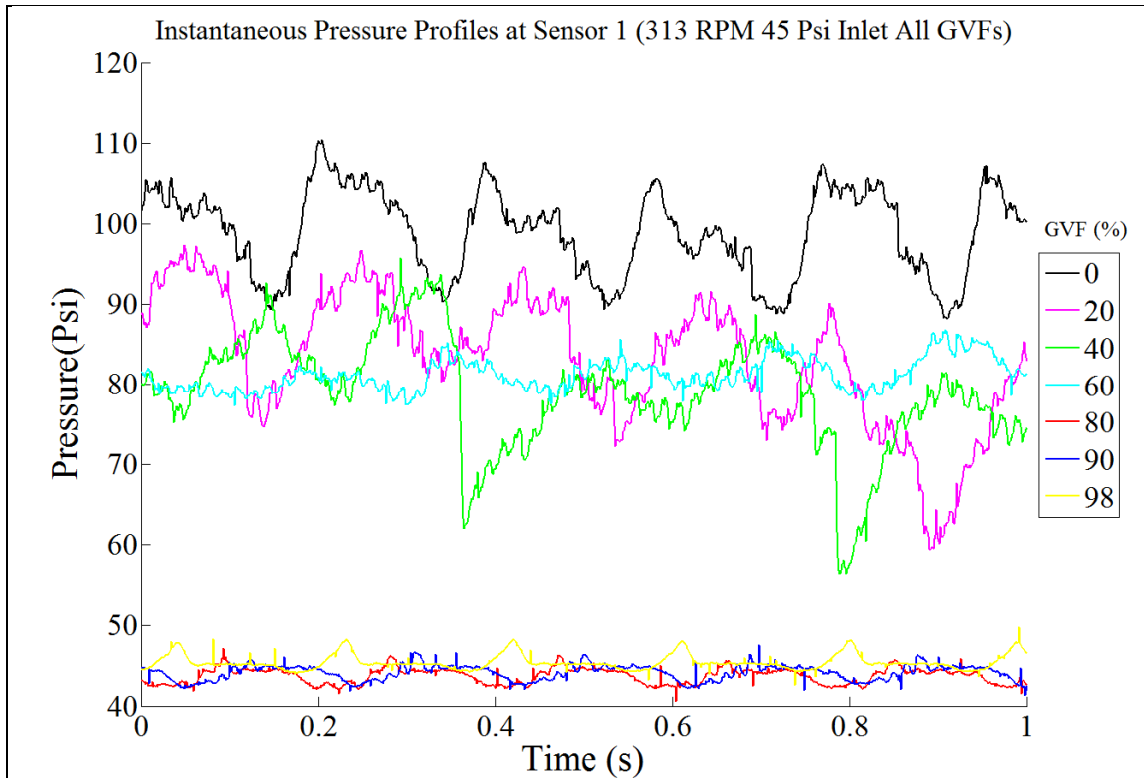
Figure 5.30 : Pressure profiles at sensor location 1 at 313 RPM.

Secondly the pressure profile at the 4th stage has a characteristic plateau or flattening effect. This happens when the cavity is open to the exit plenum. This value is more constant and equal to the exit pressure since the compressibility of the liquid in the downstream pipe damps the pressure pulsations due to the pulsating flow rate. The steep decrease in pressure happens simultaneously in all sensors which is indicative rotor-stator contact area end transient effect. There is a transient rise in pressure until the rotor is touching the stator at the pressure tap. The rise is due to the leakage to downstream cavities. This is observed in all cavities 2, 3 and 4 and the increase in pressure reflects an increase in backflow leakage. As the pressure rises downstream the leakage increases, reflecting in the rising pressure levels as we move from cavity 2 to cavity 4 shown in Figure 5.31. The pressure rise level in cavity 4 is higher than that at cavity 3 which in turn is higher than that of cavity 2 signifying higher leakage with higher pressure downstream. The understanding of this effect is key to understanding the leakage. This can prove as very good diagnostic to better understand the

stator wear and the resulting clearance generated in the 4th stage. The curves bear similarity to pressure curves of a piston air compressor curve.
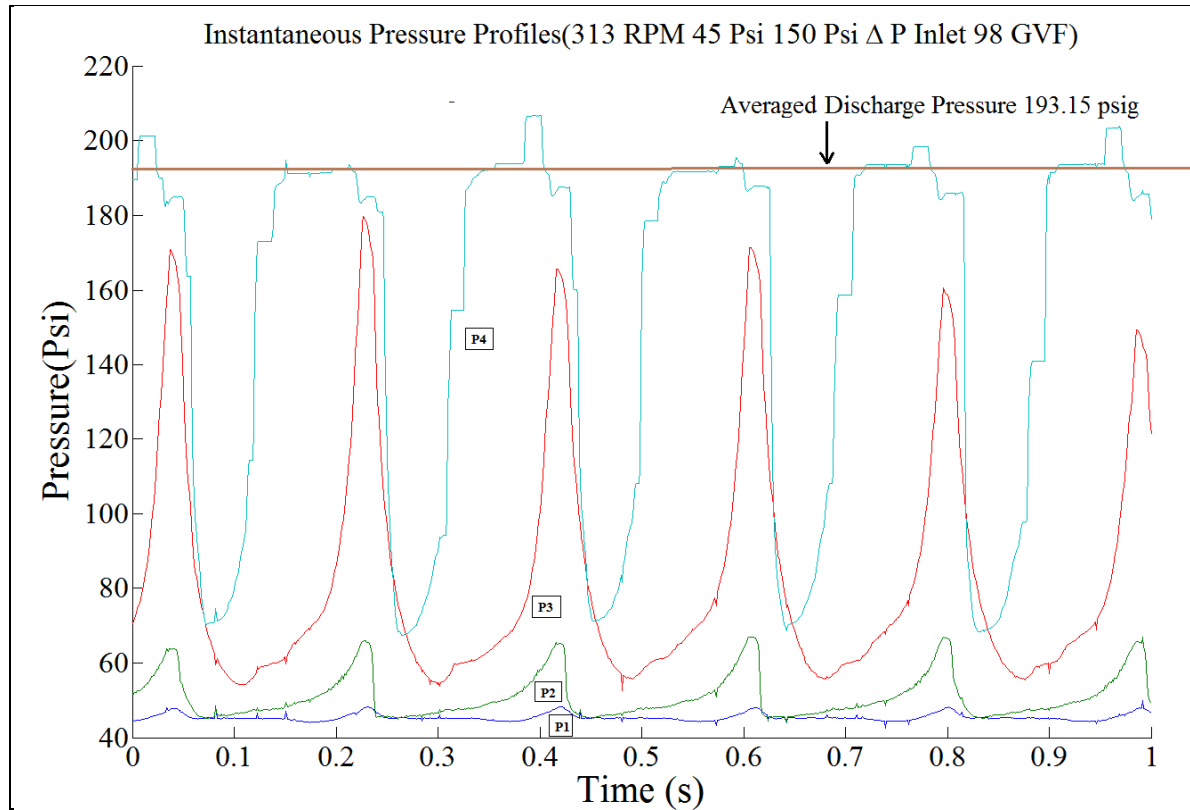
Figure 5.31 : Pressure profile for 98% GVF, 313 RPM.

To better understand the profiles a plot similar to that made by Gamboa et al.[7] was studied (Figure 5.32, Figure 5.33). The only difference in this case was that the profiles were studied for the 4th and 3rd stages. Surprising similarities were found. For instance, close points (earlier defined as the position attained by the rotor when the pressure recorded by the sensor increased instantaneously) were observed earlier at 0% GVF case as compared to higher GVFs and not only did the close points occur at a later angular position in this case but the pressure rise was also lower. These observations are analogous to the findings for a metallic stator with clearance. This strengthens our finding of the leakage at the 4th stage but in spite of this leakage there is minimal back flow from the 3rd to 2nd or so-on. So the pump does seal itself and hence maintaining a volumetric efficiency above 95%.

These findings could be used to study the pressure and velocities inside the pump to design the stator for less leakage and wear. Not only does this study acts as a diagnostic for understanding pump wear but can also be used to study the effect of compressibility of the fluid on leakage.
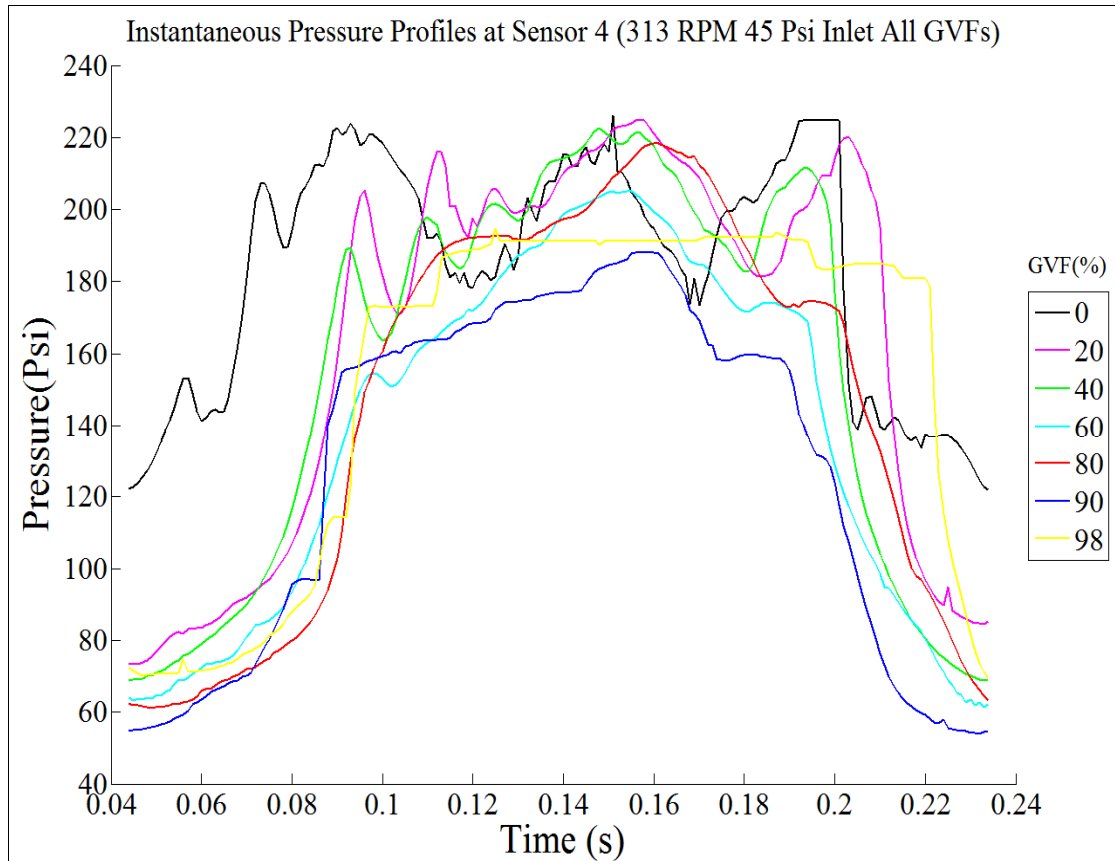
Figure 5.32 : Pressure profile at sensor location 4 for all GVFs.
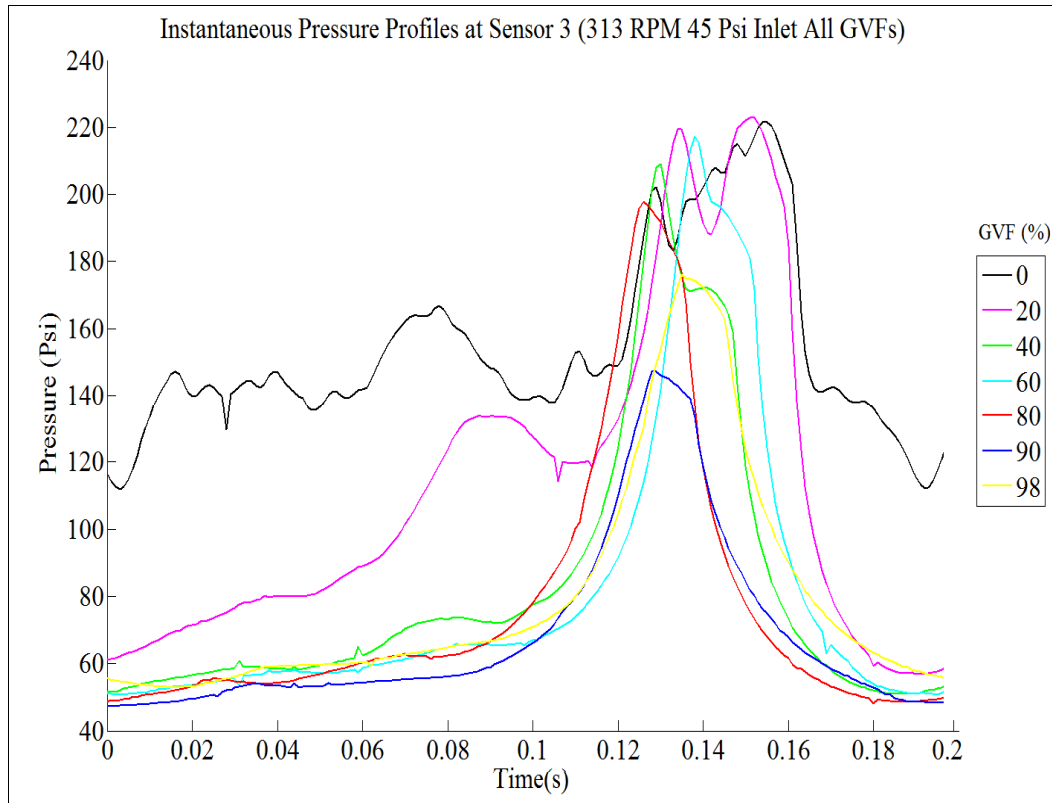
Figure 5.33 : Pressure profile at sensor location 3 for all GVFs.

The steep rises in pressure levels are due to back-flow to the previous cavity. It is also noticed that the peak locations vary with GVF ranging from 140 psi to 220 psi for 90% GVF and 0% GVF respectively. The pressure peak is above the averaged discharge pressure for GVFs above 80%. As discussed earlier the pressure rise for high GVF cases was towards the discharge of the pump unlike that for lower GVF cases.

5.2.2 Temperature and Pressure Study at GVF Surges

The transient studies are very critical to running the pump at off-design conditions. A 100% GVF is an extreme condition to which the pump could be subjected to in case of a dry run out. These situations are very common in the field where oil producing wells can experience

a dry spell of only natural gas. Hence understanding the pump's response to these conditions can provide valuable information for a manufacturer to design them for such situations. Also, running these pumps at 100% GVF conditions for prolonged periods can alter its volumetric efficiency as there can be changes in geometry due to rubber wear. Methods have been suggested to ensure minimal damage to the pump when run at these off-design conditions.

Apart from the 100% GVF study it is also important to understand the opposite effect, that is, when a pump running at 100% GVF is subjected to a surge of water. This in oilfield terms would be referred to as water cuts. Understanding the pumps response to water-cuts is important as this may damage the pump if the pressure surges are not controlled.

The following study takes an in-depth look at the temperature rise associated with steady state pump operation at 100% GVF for an extended period of time. To characterize the heat rise, different conditions were studied. To prevent pump damage due to dry running the pump was first run at half speed and the GVF was surged from 80% to 100% and the temperature monitored. This was done in steps of 75 Psi ΔP to closely monitor the temperature rise and to exercise caution not to burn the rubber. On noticing a very steep increase in temperature the pump was not subject to a 100% GVF at full speed. Instead it was surged only up to a 98% GVF and the temperature monitored. This led to key insights and suggestions to run the pump at these high GVFs which shall be discussed. Also the pump outlet temperature was studied to monitor the effect of pressure rise on the temperature of the compressed gas.

The next step was to study the effect of water cut in the pump. This was done by subjecting the pump to a surge of water when running at half and full speed. The key to these set of experiments were keeping the inlet conditions constant and surging the pump but controlling the inlet pressure at the same time. The pump outlet was constricted to maintain a significant differential pressure and the effect of surge was studied. This study is important for two reasons. One is to keep the pressure rises within the design limits of the pump.

As we know a positive displacement pump cannot be subject to pressures higher than its design because if the pump outlet is constricted beyond a limit the pressure rise could be infinite damaging the components. Secondly, it is also important to keep a track on the load to which the motor or drive is subject to. A sudden increase in water could put an unprecedented load on the motor which could damage it.

These studies are very important to understand both in terms of design and installation. As there are no recommended design limits existing for this pump these results could quantify and set running conditions and aid in prognostics.

Figure 5.34 represents one of the worst off-design conditions at which the pump could be run, an 80% to 100% GVF transient. The rubbing friction between the rotor and stator increases drastically with increase in GVF. Though the load on the motor is supposed to lower by a significant amount, the reduction is not that high because of the increase in rubbing friction. This rubbing friction generates a lot of heat and the stator surface temperature was monitored. At these conditions, for both differential pressures, the temperature rise was rapid reaching up to 9.22^0 F/min. This could be very disastrous to the pump if allowed to run even for a couple of minutes as the data suggests the temperature will rise above the 200^0 F limit for the stator recommended by seepex. It was concluded that this pump should not be run at 100% GVF even at lower speeds. The heat transfer model predicts a temperature of more than 180^0 F at the highest point. So it was decided to conduct the full speed experiments with more caution and the pump was subject to only 98% GVF which was surged from 80%.
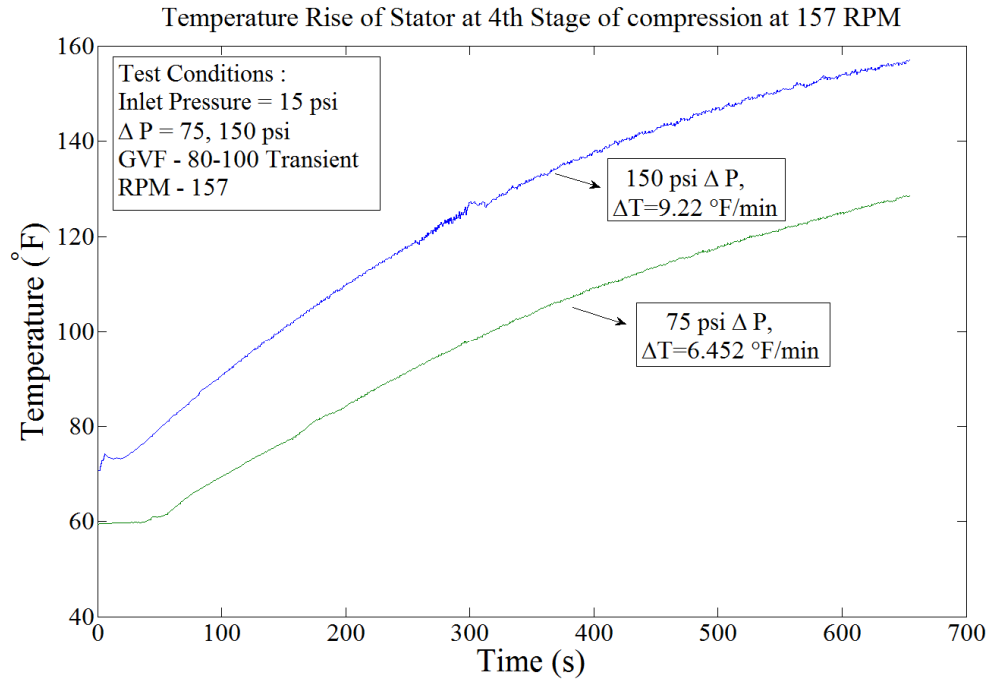
Figure 5.34 : Transient temperature rise of the stator at 4th stage at 157 RPM.
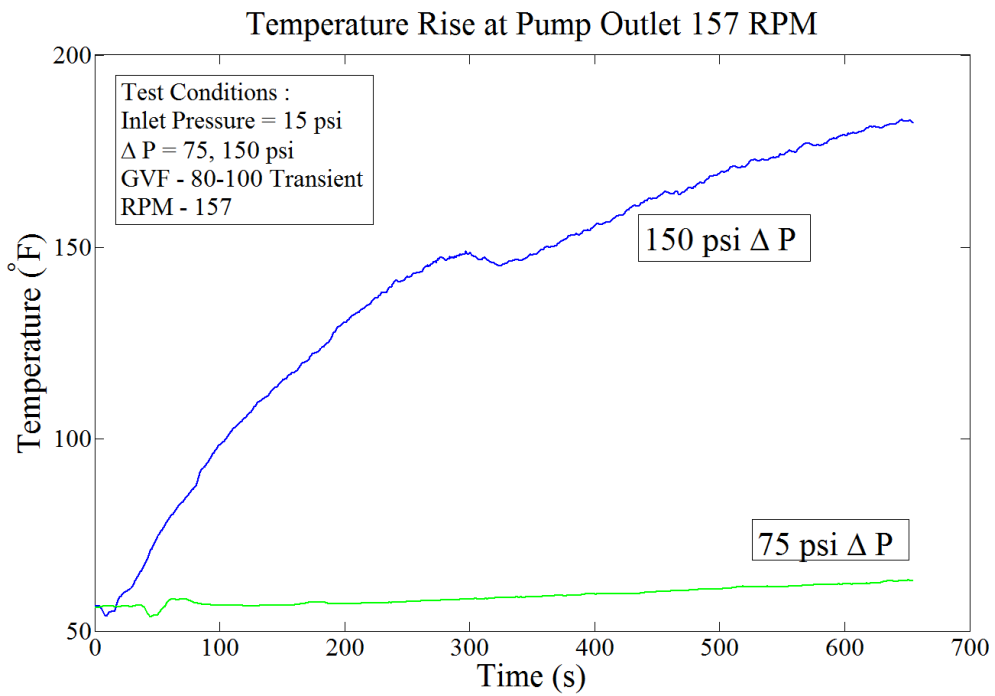
Figure 5.35 : Temperature rise at pump outlet at 157 RPM. 100% GVF.

The temperature at the pump outlet was monitored at the same given conditions at half speed to better understand the dependence of temperature rise on rubbing friction as against gas compression. The findings are plotted in Figure 5.35 for both differential pressures. At 75 Psi ΔP the temperature rise at the outlet was not significant. This suggested a larger dependence of the stator temperature rise on rubbing friction rather than heat generated due to gas compression. At 150 Psi ΔP the temperature rise is significantly higher. The rubbing friction plays a key role in temperature rise and if the co-efficient of friction could be maintained to minimize this friction the pump could be run at a 100% GVF. This possibility was explored at full speed where the pump was never subject to a 100% GVF. Instead the surge was only up to a 98%. The temperature at the 4th stage of compression as well as the temperature at exit is plotted in Figure 5.36. Unlike the half speed case there is a correlation between the T_{exit} and T_4 once the steady state values were attained. Irrespective of pressure rise the ratio of T_4 to T_{exit} remained constant within the 1.022 to 1.025. This relationship is true only for the full speed and fails for the case of half speed. This is due to a non-linear relationship between rubbing friction and speed of rotation as discussed in Section 5.1.3. The rubbing friction is a 73% percentage of the full speed value at half speed hence a major contributing factor in the temperature of the 4th stage. In case of higher speeds the temperature rise has a higher percentage contribution from gas compression as compared to rubbing friction and hence constant temperature ratios can be observed.

A 98% GVF transient study (Figure 5.36) at full speed could be a key take away from this study. It was noticed that at 98% GVF the temperature reaches a steady state value and the increase is minimal. This would mean that with a 2% recirculation, the PCP could manage a higher GVF above 98% for prolonged periods. A 2% liquid re-circulation would mean 12-15 GPM at full speed for this PCP. The study of a PCP with recirculation is recommended as the PCP exhibits higher mechanical and volumetric efficiencies than a twin screw pump at high ΔP.

Temperature Rise of T_4 and T_{exit} at 4th Stage of compression 313 RPM
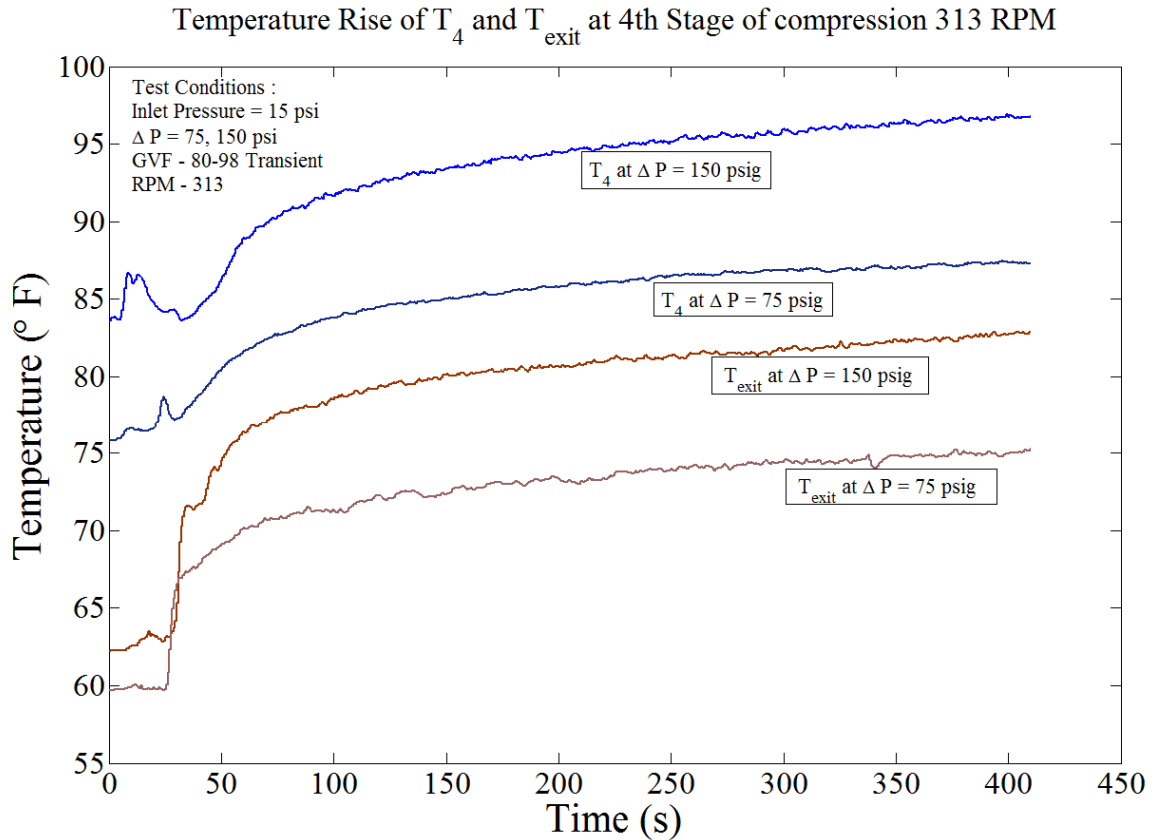
Figure 5.36 : Transient temperature rise of the stator at 4th stage at 313 RPM.

The study of high water cuts was the last test to be performed in the transient study. Water cut is defined as the ratio of water produced compared to the volume of total fluids produced. One of the main reasons why this study is important is that it influences the pressure surge at the pump outlet and this is very critical to the safe functioning of the pump. As discussed earlier, a positive displacement pump cannot be dead headed as this would cause severe damage to the pump internal parts. The response of the pump is different for a fixed valve position at the outlet for air and water. This is due to the compressible nature of air. Due to this important difference the pump outlet pressure can surge when subject to large water cuts. Though the PCP was installed with a pop-off valve at the outlet, the pressure at the outlet must be monitored and controlled to avoid damages to the rotor. Figure 5.37 shows the pressure rise when the pump is subject to a transient drop from 98% to 75% GVF. The pump was maintained at a discharge pressure of 15 psi prior to the surge. The discharge

valve setting was not varied, the pump inlet pressure was maintained at 15psig and the GVF was varied from 98% to 75%. It was observed that irrespective of the speed, the surged outlet pressure reached up to 140 psig. This observation can lead to a conclusion that even a small drop in GVF can surge the pump outlet pressure. The magnitude and time constant of the pressure rise will vary with the volume in the piping between the pump exit and the valve. A larger volume will reduce the rate of pressure rise.
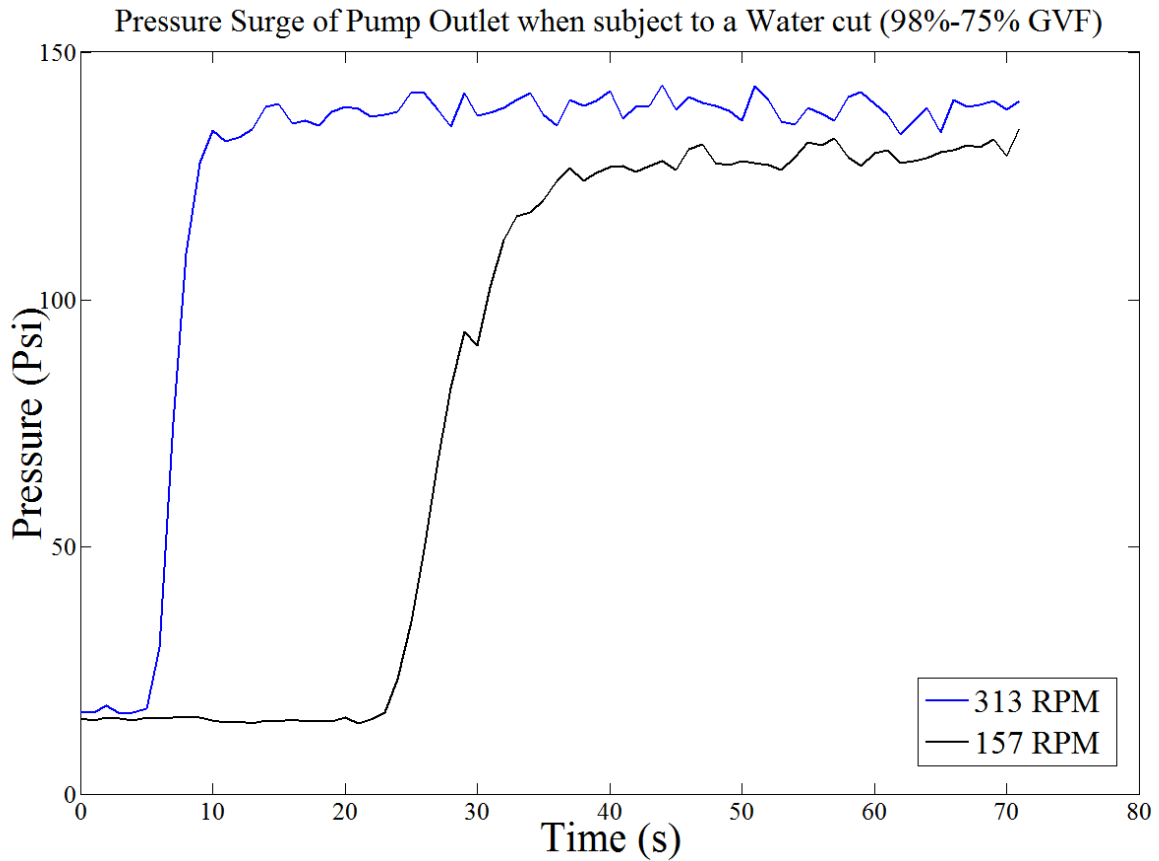
Figure 5.37: Pressure surge when subject to a transient rise in GVF from 98% to 75%.

Considering the fact that the maximum pressure which this pump can be subject to is 200 Psi, the user needs to exercise extreme caution when handling unexpected drops in GVF. A fast response closed loop control at the pump discharge is a possible solution to this problem. Also a switch control could be established connecting the discharge to the VFD where the VFD could control the motor speed based on the pressure rises. The programming of such loops would have to be based on existing empirical data. The rate of response required can be reduced by adding an accumulator at the pump exit.

Figure 5.38 shows the rise in the load of the motor in the same conditions. It would be difficult to isolate the effect of GVF and ΔP but the load is well below the maximum rating of the drive. The difference in times of rise is solely a delay on the part of the user in triggering the surge. Though it may not be critical to monitor the load on the motor one has to make sure the pressure surge is not beyond the maximum rated capacity of the pump. The averaged load increase is 6.59% and 5.78% for full and half speed respectively.

Figure 5.39 illustrates the temperature response of the rubber stator. The last stage temperature is most influenced in this water cut. The temperature dropped down more than 5° F and the lower temperature of the last stage was due to the low water temperature at inlet. The non-conformance of the third stage temperature with other stages is possibly due to the dislocation of temperature sensor. It can also be concluded that the temperature of the last stage can be controlled easily by introducing large volumes of water at short intervals. This is a good motivation to study the effects of liquid recirculation or seal flush injection on temperature rise along the axis of the pump.
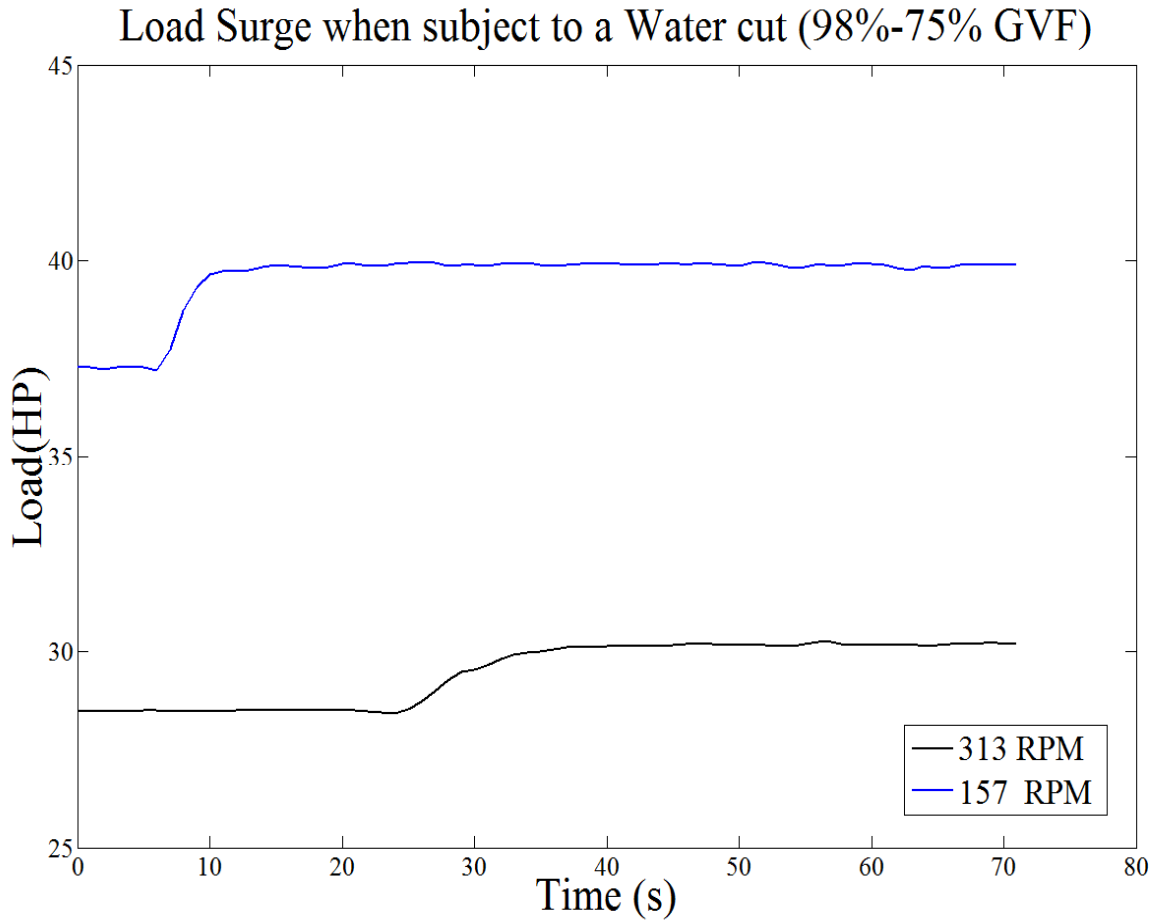
Figure 5.38: Load variation at 98%-75% transient drop.
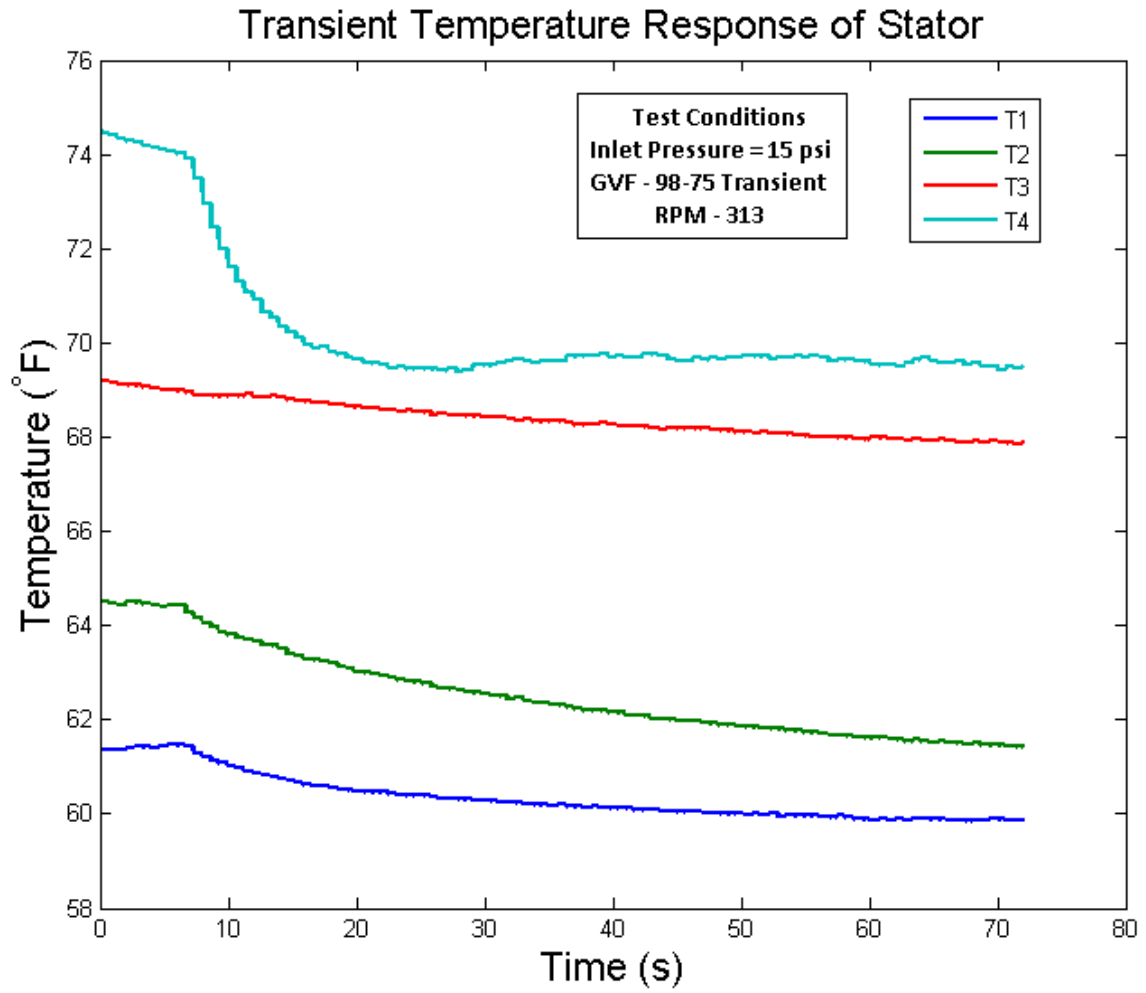
Figure 5.39 : Temperature response of stator (98% to 75%).

5.3   Vibration Measurements

Vibration is defined as mechanical oscillations or the repetitive motion of an object about an equilibrium point. The importance of studying the vibration issues in this pump was realized when unusual mechanical noises due to vibration were noticed at certain differential pressures. These observations made it impossible to run the pump at these conditions as it would result in loud clanking noise at the bearing housing. Vibration problems in pumps are a result of interactions among a system's pump, motor, fluid, piping, and structure. The interaction of these parameters is complex and it can be difficult to isolate the parameters to study the effects of individual parameters on the overall vibration of the system.

A tri-axial accelerometer was mounted at the bearing housing as shown in Figure 4.18. The intention was to study the axial and radial vibration when the pump was subject to the test matrix as detailed in Table 5.2. The discharge pressure was always set to be zero by ensuring a fully open electro-pneumatic control valve. At 80% GVF and a zero discharge pressure the suction pressure was increased from 0 to 45 psi.

Figure 5.40 shows the maximum vibration limit encountered in these conditions. One can see that the vibration levels increase with increase in suction pressure. This increase with increase in suction pressure can be concluded as the imbalance caused in the rotor due to a negative pressure distribution. The rotor in case of a PCP acts a cantilever and when one end which is supported by the coupling near the bearing is subject to a high pressure it responds with high amplitude. This effect is reflected by the radial acceleration measurement and seems to diminish after a certain threshold pressure for both half and full speed. The peak is higher for the half speed scenario. The axial vibration measurements on the other hand don't exhibit such a pattern. The maximum vibration seems to be at the highest suction pressure and does not seem to be very dependent on the speed of operation of the pump.
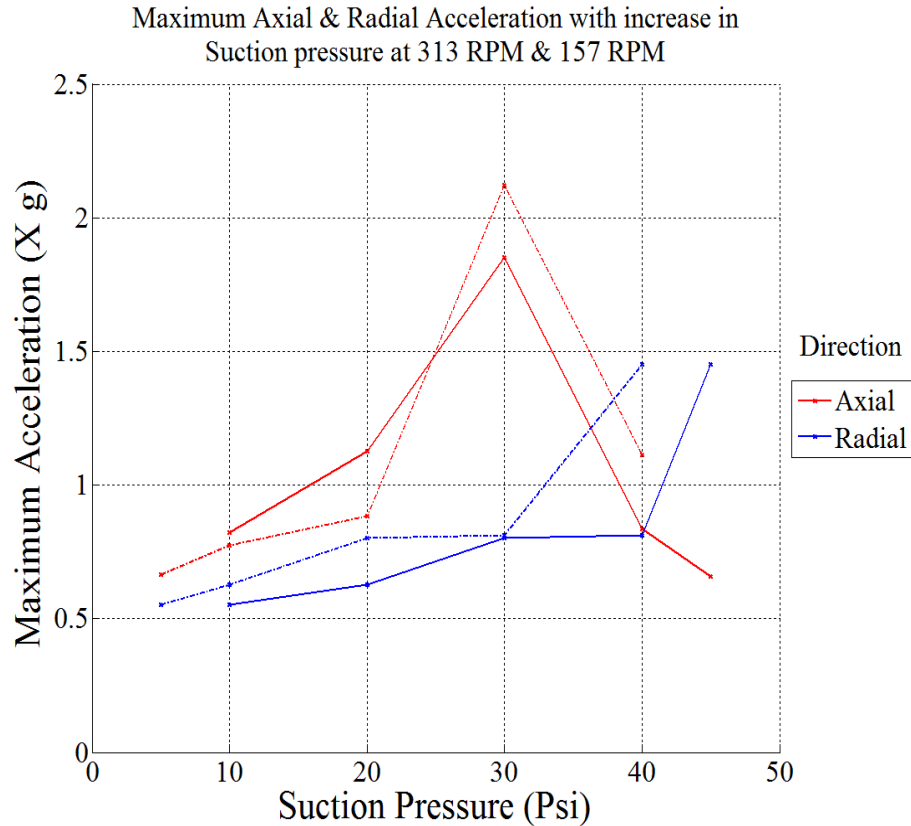
Figure 5.40 : Maximum vibration at zero discharge pressure.

To understand the vibration issues in detail an FFT was performed at these points of maximum radial acceleration and at half speed one could notice peaks at 180 Hz and 360 Hz. There were also a few peaks around the 60 Hz. The 180 Hz peak is an indication of the vibration in the gear box as the PCP in our study uses a 1:6 speed reduction gear box. The gears are obviously subject to a load imbalance in this condition causing a peak in our FFT analysis. The one times operating speed vibration is usually present and a good indication of proper operation which is clearly noticeable in Figure 5.42.

The vibration effects on the PCP obviously need to be studied in more depth. This is intended to be just an introductory study to a potentially serious problem and to warn the user from subjecting the pump to certain test conditions. This could severely damage the bearing leading to its failure.

Radial and axial clearances between rotating and stationary surfaces are important physical parameters. They are usually expressed as "maximum allowable," and should not be exceeded. Other types of OEM criteria may include limits on pressure, differential pressure, speed, temperature, etc.
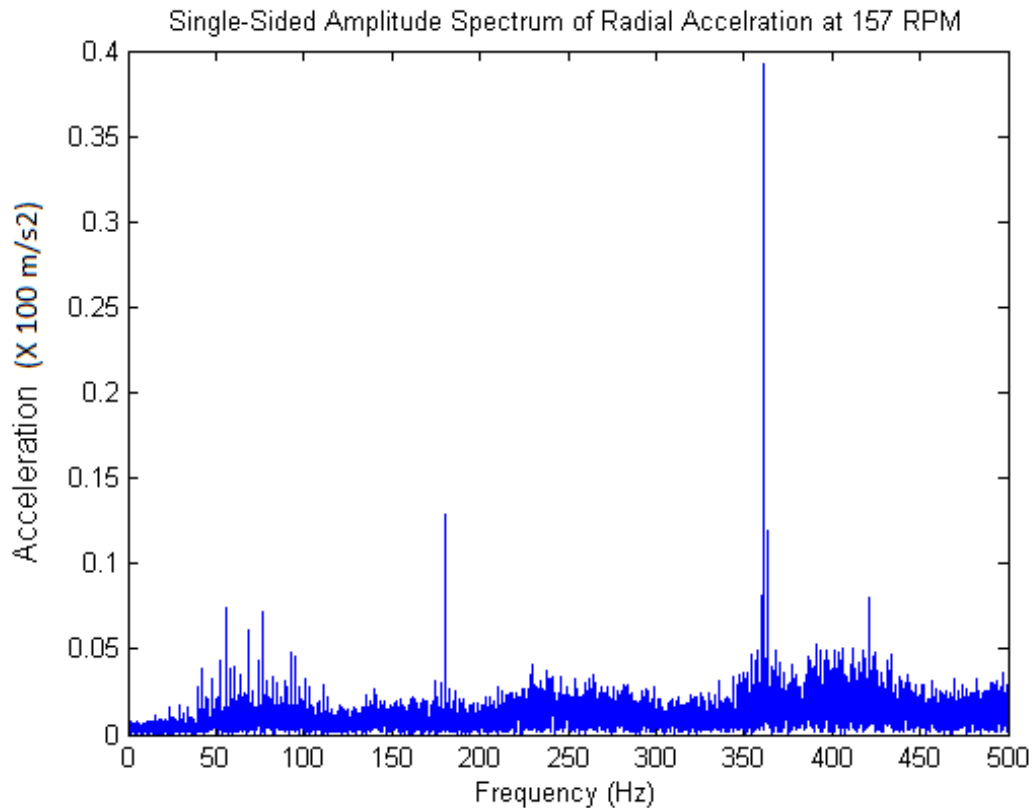
Figure 5.41: Radial acceleration FFT at 157 RPM.

Acceleration measurements are not used for trending, but are most useful for diagnostic work. Acceleration signals accentuate the low amplitude, high frequency signals for diagnostics.

Standards for vibration limits [20] are published by industry groups, and by national and international standards organizations including:

- the American Petroleum Institute (API),
- the American Gear Manufacturer Association (AGMA),

- the National Electrical Manufacturers Association (NEMA), the American National
- Standards Institute (ANSI),
- and the International Standards Organization (ISO).
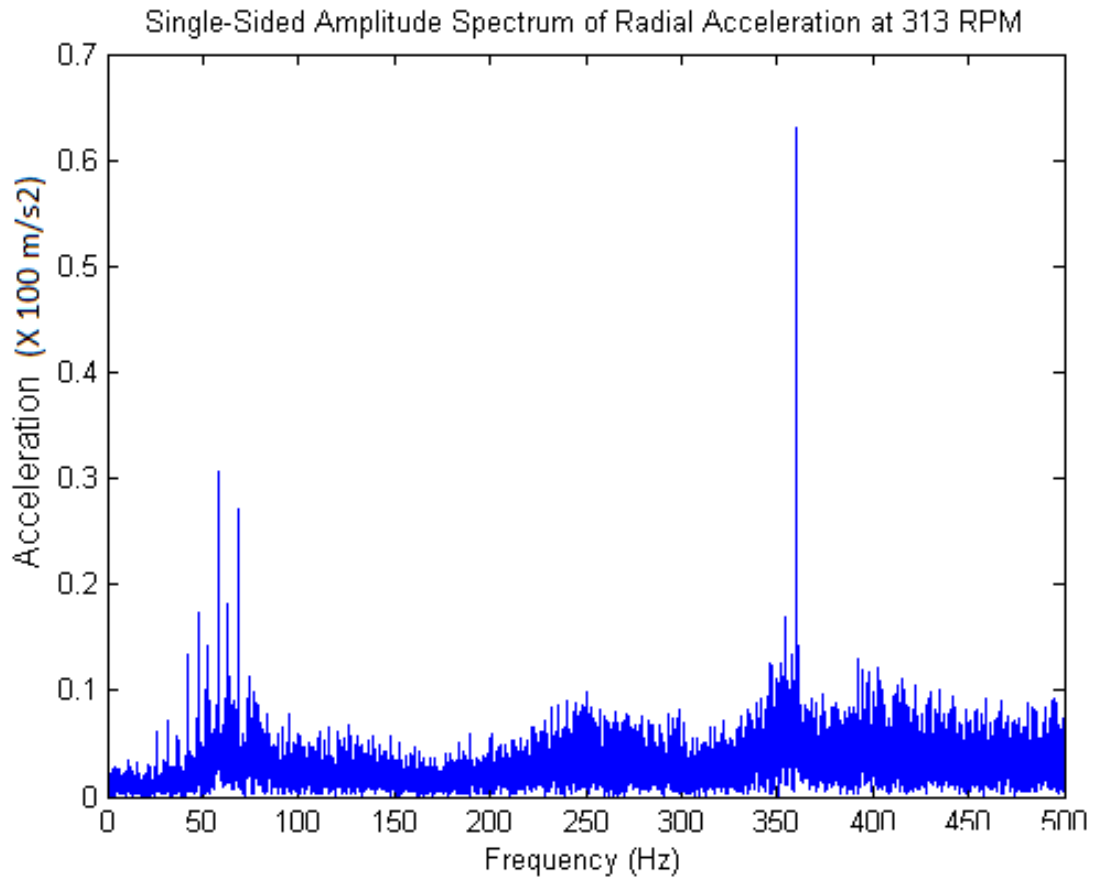
Figure 5.42 : Radial acceleration FFT at 313 RPM.

A more detailed study of the vibration consisting of comparing the existing data to industry specifications is deemed necessary for better understanding of the PCPs response to different conditions.

6. CONCLUSIONS

The objective of this investigation was to study the progressive cavity pump with an elastomeric stator by simulating a range of field conditions within the Turbo-machinery multiphase flow facility. The intentions of this study are three fold. One was to aid Shell to make an informed choice in the field when selecting this pump for a multiphase pumping application. The main concerns of the end user would be the flow rate, efficiency and the mean time between failures (MTBF). The failure of the seepex pump is mainly governed by the failure of the elastomeric stator which can swell due to the high temperature build up when subject to high GVFs. This has been addressed in depth in this study. Other possible reasons for failure would be seal wear, bearing failure and high discharge pressures. The second intention would be to suggest design changes in the pump based on its performance. These changes have been suggested based on the pump's response to the steady state and transient experiments conducted. The third and fundamental objective of this project is to understand the fluid dynamic behavior of multiphase flow in this pump. The effect of GVF on the fluid flow was studied by measuring the parameters at fixed stator location points. The observed behavior was compared with available analytical results as well as two-phase flow equations.

Section 6.1 summarizes the results from the steady state pump performance characteristics. Section 6.2 summarizes the results from the transient on pump performance while operating at 98% GVF, 313 RPM, and the 45 psi inlet condition. The following sections will also include specific recommendations for further characterization of the steady state pump performance and recommendations to improve the MTBF of the pump by introducing liquid recirculation. Section 6.3 details the vibration results.

6.1   Steady State Performance

The steady state performance led to very important results. One of the most important results being the very high and consistent volumetric efficiency of the pump. Due to a no clearance

fit between the rotor and the stator, there was no overall slip in the pump. The slip was only in the last stage and it was clearly established that there was no slip in the pump as a whole. This could be used to reduce the number of stages in the pump especially for high GVF applications. The PCP easily outperforms the conventional twin screw, Archimedes screw pumps or a PCP with a metal stator as they have a positive clearance and hence a finite fluid backflow. While previous studies by R & M systems shows a reduced volume flow after running the pump for long hours, this could only be possible because of the wear of the elastomeric stator with time and in our case we can safely assume that the rubber had a tighter fit with no clearance or wear even after running the pump for the amount of hours it was tested. Also the pump was tested right out of the factory ruling out any chance of wear.

The mechanical efficiency of the pump increased drastically with ΔP due to the fact that the power required to overcome the friction was independent of ΔP and was a set value. The mechanical efficiency was also higher for higher suction pressures at higher GVFs. This was due to the increased suction volume at higher suction pressures. The efficiency is independent of suction pressure at low GVFs and the difference was zero at 0% GVF due to the incompressibility of water. This gives the end user an optimum range of operation to attain highest mechanical efficiency. Thermodynamic efficiency on the other hand was purely a measure of the gas in the fluid being pumped, the value being higher for higher suction pressures for the same reasons as before. Hence the thermodynamic efficiency was independent of RPM but reduced drastically with ΔP due to the fact that lesser energy was input to pressurize air than water. Volumetric efficiency remained constant with changes in RPM due to minimal back flow and showed an increase at higher GVFs at higher suction pressures. Glier's [18] relationship of flow rates at half and full speed justified the observed higher volumetric efficiency at half speed.

It can be recommended that the best operating point would be at high differential pressure. As mentioned earlier the reduced mechanical efficiency at low differential pressures is due to the energy input into the pump to overcome the rubbing friction between the rotor and stator. Hence there is an increase in pump efficiency as the pressure rise increases. It would be very challenging to design a rotor stator combination such that there is a finite clearance, improving the mechanical efficiency and yet not compromising on the volumetric efficiency

of the pump. Also a rubber stator with very low co-efficient of friction can be installed to minimize the rubbing friction enhancing the mechanical efficiency.

The study of dependence of inlet pressure, rubbing friction and temperature rise of the stator surface could be of greater value in understanding the pump better but limited instrumentation stopped us from investigating this in depth.

The load dependence on GVF was very evident in these experiments. Though the load on the motor was lower for a lower GVF, the reduction was not low enough to compensate for the very low mechanical efficiencies at these high GVFs. The drive size could be reduced for a high GVF case but other factors like water cuts, pressure surges need to be considered too before making such a decision. Another problem faced during this study is the inability to maintain a constant pressure at the outlet. Due to the low RPM of the pump and the drastic reduction in the discharge piping volume causes large fluctuations in discharge pressure. An accumulator can help reduce these fluctuations and hence enabling evaluation of the pump at higher and steadier discharge pressures.

The pressure profiles along the stator provided a better understanding of the GVF effects on the pump's behavior. A non-linear profile was observed for a high GVF as predicted by the existing analytical model but it was also noticed true, that this effect was not as simple as predicted. At very high and low GVFs, the predictions hold but in mid GVF's, the pressure profile approaches choked flow conditions and a reduced flow rate is observed. Though a distinct choked flow was never established the effects were clearly seen for mid GVF ranges. The pump could never be subjected to steady state100% GVF running conditions. This has been detailed in the next section with appropriate recommendations for the end user. But again, designing the pump with a positive clearance may solve this problem to a large extent.

In summary the pump has been subject to the range of operating conditions which a user could encounter during its life time and the best operating points for a two phase flow have been identified. The next step would be to study the effects of a third phase in the mixture namely sand. Sand would have erosive effects on the stator and rotor surface and this may lead to performance degradation. The next step in this project would be to take up this study and investigate the effects of this phase on bearing life, stator wear and vibration. Also it

would be useful to study the pump with an accumulator at the discharge. This would give as mentioned before steadier discharge pressures.

6.2   Transient Performance

The transient study has been of more practical significance in the eyes of the end user i.e in the application of the oil extraction. In the field the equipment is never subject to a steady state field condition. The study was first focused on the instantaneous pressure profile of a single sensor on the stator. This study helped in realizing a fluid backflow in the final stage of the pump. This was indicated by comparing the pressure rise with Gamboa et al.[7] data which was performed on a stator with positive clearance. This slip did not hamper the volumetric efficiency of the pump as there was no back flow in the earlier stages.

To study the effects of dry running, the pump was surged to a 100% GVF when running at 75 %. The temperature never reached a steady value at half speed. The presence of a small amount of liquid in the circulation was deemed necessary for the safe running of the pump. It was concluded that at 98% GVF the temperature reaches a steady state value and the increase is minimal. It was concluded that at a 2% recirculation the PCP could manage a higher GVF of 98% for prolonged periods. A 2% liquid i.e 12-15 GPM at full speed for the PCP was found ideal for long running hours. The study of PCP with recirculation could be of good value as the PCP exhibits higher mechanical and volumetric efficiencies than a twin screw or a Archimedes screw pump.

The pressure surge at the discharge due to a water cut could severely damage the pump. It was noticed that the surge was same irrespective of the speed. Some of the recommendations to avoid such a surge are detailed below:

- A closed loop control which senses an incoming surge from the load variation in the VFD and controls the electro-pneumatic valve at the discharge.

- A control switch governed by the pressure sensor in the discharge which would shut down the VFD in case of an unexpected surge. In this case the switch's time response needs to be very fast.

- A conventional pressure relief valve which will redirect the fluid to the pump inlet in case of a pressure surge.

It is very important to make sure a positive displacement pump is not subject to a pressure more than it's designed operating pressure and implementing one of the above choices would ensure safe operating of the pump.

6.3 Vibration

The pump was subjected to the test matrix defined for the vibration studies and high acceleration limits were observed at certain differential pressures. At half speed the maximum limit was observed up to 2.2g. This is unacceptable according to API standards and the pump should not be subject to such conditions for prolonged periods. The FFT clearly showed gear-box interference at low as well as high speeds. These vibrations can be reduced to a great extent by designing a pump with multi-lobes. A multi-lobed pump would have a lower eccentricity and hence a reduced rotor imbalance.

The effects of flow rate on the observed vibration were not studied in this investigation and is suggested for further study. Also it is highly recommended to study the pumps vibration w.r.t to the current API/ANSI standards as satisfying these criteria is important to proper functioning of the pump in the field.

REFERENCES

[1] Alemaskin.K, Nandakumar, K., Sundararaj, U., 2006, "Progressive thinking for pumps, " Article in Fluent Newsletter, Volume XV, Fall 2006.

[2] Karassik, I.J, Messina J.P, Cooper P, Heald., 1991, *Pump Handbook*, Third edition, McGraw Hill, New York.

[3] Nesbitt, B., 2006, *Handbook of Pumps and Pumping*, First Edition, Elsevier, Amsterdam.

[4] Cholet, H., 1997*, Progressive Cavity Pumps*, Editions Technip, Paris.

[5] Delpassand, M.S., 1997, "Progressive Cavity Pump Design Optimization for Abrasive Applications," Paper SPE 37455 presented at the 1997 SPE Production Operations symposium held in Oklahoma City, 9–11 March.

[6] Gamboa, J., Olivet, A., Espin, S., 2003, "New Approach for Modeling Progressive Cavity Pumps Performance," Paper SPE 84137 presented at the 2003 SPE Annual Technical Conference and Exhibition held in Denver, Colorado, 6–9 October.

[7] Gamboa, J., Olivet A., Gonzalez P and Iglesias J., 2002, "Understanding the Performance of a Progressive Cavity Pump with a Metallic Stator," Proceedings of the 2002 20th International Pump Users Symposium held in Houston, Texas, 17-20 March.

[8] Bratu, C., 2005, "Progressive Cavity Pump Behavior in Multiphase Conditions," Paper SPE 95272 presented at 2005 Annual Technical Conference and Exhibition held in Dallas, Texas, 9-12 October.

[9] Egashira, K., Shoda, S., Tochikawa, T., 1996, "Backflow in Twin-Screw-Type Multiphase Pump," Paper SPE 36596 presented at the 1996 SPE Annual Technical Conference and Exhibition held in Denver, Colorado, 6–9 October.

[10] Belcher, I., 1991, "An Investigation into the Operating Characteristics of the Progressive Cavity Pump," Doctoral Thesis at the British Library 1991, Cranfield Institute of Technology, United Kingdom.

[11] Zhou, D and Yuan, H., 2008, "Design of Progressive Cavity Pump Wells," Paper SPE 113324 presented at 2008 SPE Progressing Cavity Pumps Conference held in Houston, Texas, 27-29 April.

[12] Dillon, M., Vullings, K., 1999, "Applying the NPSHR Standard to Progressing Cavity Pumps," *Pumps Magazine* , 1999.

[13] Räbiger, K. E., 2009, "Fluid Dynamic and Thermodynamic Behavior of Multiphase Screw Pumps Handling Gas-liquid Mixtures with Very High Gas Volume Fractions," Ph.D. Dissertation, University of Glamorgan. Germany.

[14] Incropera, F.P., DeWitt, D.P., 2007, *Fundamentals of Mass and Heat Transfer*, 6th edition, John Wiley & Sons Inc, New Jersey.

[15] Matthews, D.L, Zahacy, T., 1994, "Progressing Cavity Pumping Systems: Design, Operation and Performance Optimization," Course manual 1994, Centre for Frontier Engineering Research (C-Fer). Alberta.

 [16] Robello, G.S., Ken, K., 1998, "Progressive Cavity Pump (PCP): New Performance Equations for Optimal Design," Paper SPE 39786 presented at the 1998 Permian Basin Oil and Gas Recovery Conference, Midland, Texas, 25-27 March.

 [17] Bratu, C., Seince. L., 2005, "New Progressing Cavity Pump (NPCP) for Multiphase and Viscous Liquid Production," Paper SPE 97833 presented at the 2005 International Thermal Operations and Heavy Oil Symposium, Calgary, Alberta, 1-3 November.

[18] Glier M., 2011, "An Experimental Examination of a Progressive Cavity Pump at Very High Gas Volume Fractions," M.S Thesis, Texas A & M University 2011, USA.

[19] Mirza, K.Z., Wild, A.G., 1997, "Key Advantages of the Progressing Cavity Pump in Multiphase Transfer Applications," Paper SPE 38812 presented at the 1997 SPE Annual Technical Conference and Exhibition, San Antonio, Texas, 5-8 October.

[20] Ecker, T, Hooker, M., 2005, *Engineering Technical Training Modules for Nuclear Plant Engineers Mechanical Series: Module #14*, Palo Alto, California.

APPENDIX A

GAS VOLUME FRACTION CALCULATIONS

Inputs

Air Inlet Pressure = P1 (psi) - Transducer Output – 111.29 psi

Pump Inlet Pressure = P2 (psi) – Transducer Output – 30.1664 psi

Air Inlet Temperature = T1 (^{o}F) – 81.95 ^{o}F

Pump Inlet Temperature = T2 (^{o}F) – 76.47 ^{o}F

Flowmeter Air Reading = F1 (Pulses/Second) – 509 Pulses/Second   (K-Factor - 2385)

Flowmeter Water Reading = F2 (Pulses/Second) – 462 Pulses/Second   (K-Factor - 911)

Calculations

1. Density of Air Inlet = {(P1 + 14.7) *6894.75}/[287.05* (T1+459.67)*5*0.111111] = 10.05 kg/m^3

   Pressure Conversion →Psi to Pascal

   Temperature Conversion → F to K

2. Density of Pump Inlet = (P2 + 14.7) *6894.75}/[287.05* (T2+459.67)*5*0.111111] = 3.618 kg/m^3

   Pressure Conversion →Psi to Pascal

   Temperature Conversion→F to K

   Gas Constant = 287.05 J/Kg-K

3. m$^{3/}$Min_Air = (((F1*60)/2385)*0.0283168466); = 0.362598 m$^{3/}$min

   Flow Conversion→Cubic feet to m^3

4. m_air = $m^{3/}$Min_Air * Density of Air Inlet = 3.644 Kg/min

5. Volume Flow Rate Air (GPM) = (m_air/Density of Pump Inlet)* 264.172052358 = 266 GPM

Flow Conversion → m^3 to Gallons

6. Volume Flow Rate Water (GPM) = (F1*60)/911) = 30.428 GPM

GVF = Volume Flow Rate Air (GPM) /(Volume Flow Rate Water (GPM) + Volume Flow Rate

Air (GPM)) = **89.86 %**

APPENDIX B

MULTIPHASE PRESSURE DISTRIBUTION (BRATU 2005)

A schematic hydraulic flow is proposed to understand the pressure distribution. The multiphase mixture of the cavity moves from inlet section (i) to discharge section (d) while there is a leakage flow (S) in the opposite direction. The pressure distribution is a function of the leakage flow S, which in turn depends on gas compression volume. Fluid mixture momentum and mass conservation describe slippage flow. Assuming negligible kinetic energy we have

$$(1 - \alpha)\rho_L \int dP \ + \ \rho_g b\alpha \int P.dP = C \int_x^0 S^2(x, P, \alpha).dx$$

where b and C are system co-efficient (pressure drop co-efficient, hydraulic diameter of flow section). This equation shows that the pressure distribution is primarily due to slippage flow while S varies with compensated gas compressed volume (ΔW). Therefore it is necessary to solve the relationship between the gas compressed volume (ΔW) and slip S.

Mass conservation of pump flow rate, including compressible gas volume, gives the volume ΔW_x that have to be compensated in section x as

$$\Delta W_x = \ \alpha * W_i * \left(1 - \frac{P_i}{P_x}\right)$$

Assuming a linear approximation of pressure distribution, the compressed volume is a part of initial gas volume (αW_i). Therefore the slip flow rate q_x that compensates ΔW_x in section x is given by

$$\frac{q_x}{q_d} = \frac{\Delta W_x}{W_i} = \alpha * \left(1 - \frac{x}{L}\right)$$

Considering the total slippage flow rate consumed between the discharge d and the section x

$$S_{cx} = \int q_x . dx = \alpha * q_d * \left(1 - \frac{x}{2L}\right) * x$$

The slippage flow in section x is given as

$$S_x = S_d - S_{cx}$$

Indicating that flow through the section x is the difference between the discharge initial flow rate S_d and consumed one S_{cx} to compensate the compressed gas volume. In multiphase flow the entire slippage flow S_d compensates few cavities, the flow rate takes the form

$$S_x(x) = S_d * \left[1 - \frac{2\alpha}{L}\left(1 - \frac{x}{2L}\right)x\right]$$

The integral for the pressure drop expression from discharge to x-section is given by

$$h_x = C * S_d^2 * F\left(\alpha, \frac{x}{L}\right)$$

where F is a polynomial. For α =0 the pressure drop function is linear and the overall liquid pressure drop can be expressed as

$$h_{0,l} = C * S_d^2, \qquad x = L$$

And the pressure drop for multiphase flow becomes

$$h_x = h_{0,l} * F\left(\alpha, \frac{x}{L}\right)$$

The pressure distribution equation can be expressed as

$$(1 - \alpha)\rho_l (P_d - P_x) + \alpha\rho_g \frac{1}{2P_i}(P_d^2 - P_x^2) = h_x$$

After simplification and substituting F as a pressure drop function

$$\frac{P_x}{P_d} = 1 - F\left(\alpha, \frac{x}{L}\right)$$

giving a linear pressure distribution for 0% GVF.

APPENDIX C

CRITICAL PUMP INTAKE PRESSURE (DEZHENG ZHOU 2008)

As discussed before, the stator is a spiral circle. Once the rotor is assembled the chamber is divided into two sealed chambers in 180° by the rotor. These two chambers alternate as the suction and discharge as the rotor rotates and with each rotation the two cavities travel one pitch length of the stator. One cavity volume is given by

$$V_c = \frac{Q_t}{2} = 2edP_s$$

If a PCP's pitch is unfolded from the stator center line, the dimensions can be approximated as shown in Figure C.1. The spiral length is the maximum fluid length.

$$l_s = \left(P_s^2 + \left(\pi(d + 4e)\right)^2\right)^{\frac{1}{2}}$$

The average cross sectional area of the cavity is given by

$$A_c = \frac{V_c}{l_s} = \frac{2edP_s}{l_s}$$

The average cross sectional area of the cavity is as shown in Figure C.1. Unfolding the crescent to give a slot the length of which can be defined as
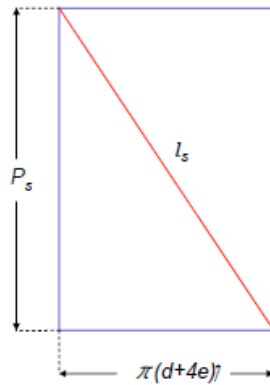
Figure C.1 : Unfolded view of a PCP stator from stator line.

$$w = \frac{\pi d}{2}$$

The slot thickness is

$$t = \frac{A_c}{w} = \frac{4eP_s}{\pi \left(P_s^2 + \left(\pi(d + 4e) \right)^2 \right)^{\frac{1}{2}}}$$
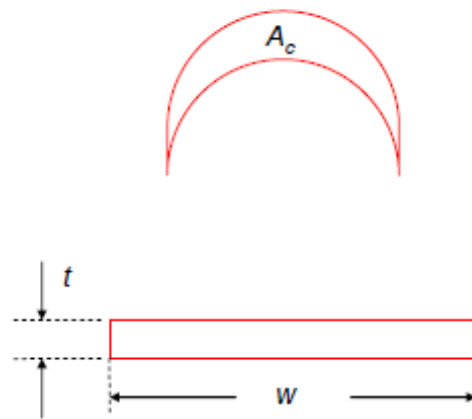
Figure C.2 : Cross-sectional area of suction cavity.

The flow co-relation in a slot for the laminar flow is given by Bourgoyne.

$$\frac{dp}{dL} = \frac{12\mu q_a}{wt^3}$$

Using the appropriate unit conversions for field units this equation is written as

$$\frac{dp}{dL} = \frac{1}{5.118E6} \frac{12\mu q_a}{wt^3}$$

where dp is in psi, L in inches, μ in cP, q_a in BPD, w and t are in inches.

Substituting the value of w we have

$$\frac{dp}{dL} = \frac{1}{8.04E6} \frac{\mu q_a}{dt^3}$$

Using an average viscosity and integrating over the length of the spiral the differential pressure can be calculated as

$$\Delta P = \frac{1}{8.04E6} \frac{\mu q_a l_s}{dt^3}$$

Assuming zero exit pressure and taking account the slip we can write the expression fr critical intake pressure as

$$P_{in} = \frac{1}{8.04E6} \frac{\mu l_s (nQ_t - q_{s\_\mu})}{dt^3}$$

APPENDIX D

UNCERTAINITY ANALYSIS

This section is dedicated to study the uncertainty associated with the results reported in previous sections. The analysis details the estimation of the error of each individual measurement, as well as the error propagation associated with parameters that are a function of other measurement variables.

In general, experimental data is processed to generate results. The relationship between the primary measurements and the results is always a mathematical function, i.e. if R is a result and $a, b, c ....$ are mathematically independent primary measurements of known uncertainty used in calculating R then we have

$$R = f(a, b, c \ldots)$$

The uncertainty associated with the quantity R is given by

$$U_R = \left[\left(\frac{\partial R}{\partial a} U_a \right)^2 + \left(\frac{\partial R}{\partial b} U_b \right)^2 + \left(\frac{\partial R}{\partial c} U_c \right)^2 \ldots \right]^{\frac{1}{2}}$$

D.1 Water Flow Rate

$$Q_{water} = WFM_a * \frac{60}{42} + WFM_b * \frac{60}{116.5} + WFM_c * \frac{60}{911} + WFM_d * \frac{60}{10603}$$

$$U_{Q_{water}} = \sqrt{\left(U_{WFM_a} \frac{60}{42} \right)^2 + \left(U_{WFM_b} \frac{60}{116.5} \right)^2 + \left(U_{WFM_c} \frac{60}{911} \right)^2 + \left(U_{WFM_d} \frac{60}{10603} \right)^2}$$

The uncertainties in the water flow meters are tabulate below and the net uncertainty of the water flow measurement was given by

Table D.1 : Flow meter ranges and uncertainty.

Range	GPM Measurement	Uncertainty
Very High	40-650 GPM	±0.5%
High	25-250 GPM	±0.25%
Medium	5-50 GPM	± 1%
Low	0.75-7.5 GPM	± 1%

The uncertainty in the measurement of the frequency by the DAQ itself was ±0.3%. The total uncertainty in the measurement of the water flow was calculated as ±0.7897%. This converted to 4.425 GPM at full speed and 2.212 GPM at half speed for full water case.

D.2 Air Flow Rate

The flow rate of air inside the pump is a function of more parameters. The flow rate is measured at the source of the compressed air system and it expands as the pressure at the inlet of the pump is lower than the pressure at the source.

$$Q_{Air\_Pump} = Q_{Air\_Inlet} * \frac{\left(P_{Air\_Inlet} + 14.7\right) * \left(T_{Air\_Pump} + 459.67\right)}{\left(P_{Air\_Pump} + 14.7\right) * \left(T_{Air\_Inlet} + 459.67\right)}$$

These calculations are detailed in Appendix-A and the uncertainty in the pressure sensor and temperature sensors are 0.3% and 0.75% respectively. Calculating the uncertainty for 75^0 F and 15 psi suction we have the following relationships.

$$U_{Q_{Air\_Inlet}} = \sqrt{\left(U_{AFM1} * \frac{60}{2385 * 0.133681}\right)^2 + \left(U_{AFM2} * \frac{60}{3695 * 0.133681}\right)^2}$$

$$U_{Q_{air}} = \sqrt{a + b + c + d + e + f + g}$$

$$a = \left(U_{Q_{Air\_Inlet}} \frac{(P_{Air\_Inlet} + 14.7)(T_{Air\_Pump} + 459.67)}{(P_{Air\_Pump} + 14.7)(T_{Air\_Inlet} + 459.67)} \right)^2$$

$$b = \left(U_{P_{Air\_Inlet}} Q_{Air\_Inlet} \frac{(T_{Air\_Pump} + 459.67)}{(P_{Air\_Pump} + 14.7)(T_{Air\_Inlet} + 459.67)} \right)^2$$

$$c = \left(U_{T_{Air\_Pump}} Q_{Air\_Inlet} \frac{(P_{Air\_Inlet} + 14.7)}{(P_{Air\_Pump} + 14.7)(T_{Air\_Inlet} + 459.67)} \right)^2$$

$$d = \left(U_{P_{Air\_Pump}} Q_{Air\_Inlet} \frac{(P_{Air\_Inlet} + 14.7)(T_{Air\_Pump} + 459.67)}{(P_{Air\_Pump} + 14.7)^2 (T_{Air\_Inlet} + 459.67)} \right)^2$$

$$e = \left(U_{T_{Air\_Inlet}} Q_{Air\_Inlet} \frac{(P_{Air\_Inlet} + 14.7)(T_{Air\_Pump} + 459.67)}{(P_{Air\_Pump} + 14.7)(T_{Air\_Inlet} + 459.67)^2} \right)^2$$

f= Uncertainty in flow meter DAQ (0.3%)

g= Uncertainty in NI-ATD DAQ (0.062 %)

$U_{Q_{air}}$ is calculated 1.74%.

D.3 Gas Volume Fraction (GVF)

The gas volume fraction is defined as

$$GVF = \frac{Q_{Air\_Pump}}{Q}$$

where $Q = Q_{Air\_Pump} + Q_{Water}$

The uncertainty in calculation of GVF is hence

$$U_{GVF} = \sqrt{\left(U_{Q_{Air\_Pump}} \frac{1}{Q} \right)^2 + \left(U_Q \frac{Q_{Air\_Pump}}{Q^2} \right)^2}$$

The calculated value is 2.267%.

D.4 Vibration

Though a tri-axial accelerometer was used the accuracy as different for each axis of measurement. The following table details the sensitivity and uncertainty of each axis of measurement.

Table D.2: Accelerometer sensitivity and accuracy.

AXIS	Sensitivity (mV/g)	Uncertainty (%)
X	104.7	0.4
Y	105.5	2.4
Z	105.8	1.7

APPENDIX E

PROGRESSIVE CAVITY PUMP SPECIFICATIONS

seepex.com Inc.

Data Sheet 818562 **Page 1**

seepex				
date	09/12/07		commission no.	818562
customer	Texas A&M University			
seepex job no.	2107569		item/denomination	
project				
1 of	seepex progressive cavity pump			
	type BN 130-12 / A6-A7-A7-F0-IE-X			
	X=0804, 13C3, 17V			

conveying product   X.000.WM
denomination	Gas, Oil and water			
rate of solids	no advice		viscosity	no advice
size of solids	no advice		pH-value	no advice
specific gravity	no advice		temperature	40 to 80 F
composition				

performance data	nom.		min	max	
conveying capacity			482	640	US.GPM
pump speed			295	390	rpm
press in press. branch	200	psig			
press in suct. branch	50	psig			
differential pressure	150	psi	operating torque	1123	lb. ft.
required drive power	88.6	Hp	starting torque	1151	lb. ft.
remarks	Data according to Performance Curve				

technical pump data			
range	BN	kind of install.	horizontal
size	130	direction of rot.	counterclockwise
pressure stage	12	pos. of branch	1

component	material	design/option
lantern	grey cast iron GG25	standard
suction casing	1.4408/316ss	
suction connection		DN 8" ANSI B16.5 150 lb.
pressure branch	1.4571/316Ti	
pressure connection		DN 8" ANSI B16.5 300 lb.
joint	standard	standard
grease	10325	
joint seal	NBR Perbunan	
coupling rod	1.4462 / Duplex SS	standard
rotor	1.4571/316Ti	standard
stator	NBR Perbunan	even wall
mechanical seal	1.4571/316Ti	for mechanical seal, Cartex DE5 with quench
seal		DE5-140-Q1Q1VMG/BQ1VMG
plug-in shaft	1.4571/316Ti	drilled ф 100x190
special designs	300 lb ANSi discharge flange	

seepex.com

Data Sheet	818562	Page 2

general operating data

kind of operation	continuous operation - 8 hr/day
site of installation	indoor dry atmosphere
remarks	

drive

type	Gear motor			
make	Nord	ratio	i= 5.68	
model	SK92F-VL-280S/4		nom./ min- max	
mounting position	B5	output speed	313/ 295 – 390	rpm
flange dia	450 mm	motor speed	1780/1676 – 2215	rpm
output shaft	716/1300-008B4	frequency	60/ 57 – 75	Hz

electric motor

manufacturer	Nord		
model	280S/4	voltage	3x460 VAC
nominal power	100 Hp	rated frequency	60 Hz.
mounting position	B5	protection	TEFC
starting	Direct at VFD	thermal class	F
special	NEMA design with Thermostats		

baseplate

standard	B-ST-LS	material	steel
drawing no.	801-200/1300-C-108A3	surface	painted
special/accessories	with risers		

painting

execution	standard
color	RAL 5013 (blue)
remarks	

packing

packing type	Skid
marking	2107569

documentation

dimensional drawing no.	89568	operating manual	1 copy English
sectional drawing no.	062-004_1		
shaft sealing sect. view	062-0GB/1380-0-1;5_4		
remarks			

additional accessories / special designs / remarks

accessories:

(1) One AcTech VFD 100 HP, model MH41000B, 3x460 VAC, NEMA 1

APPENDIX F

AIR FLOWMETER CALIBRATION DATA

1. Diameter of Sonic nozzle-1– 0.522 inches, FLOWMETER-Air High

	Calculated Data													
	Input Data													
	Diameter Used = 0.552 inches				0.552 R-Gas Con	53.35		32						
Sl.No	P_Air	T_Air(F)	P_Stagnat	T_Stagnat	P_Throat	T_Throat(	Speed_So	Area_Thro	Density_T	Density_t	m_dot	ACFM	K-Value	ACFM_M	K-Factor
1	125.233	62.769	16.2188	67.7806	8.568392	439.7996	1025.259	0.239314	0.052586	0.646602	0.089601	8.314306	197	4.91	1421.646
2	125.84	63.34	16.83	68.466	8.891289	440.3707	1025.925	0.239314	0.054497	0.649027	0.092917	8.589814	239	5.96	1669.419
3	126.169	63.78	18.5584	69.04	9.804403	440.849	1026.482	0.239314	0.060029	0.650177	0.102404	9.450079	323	8.08	2050.776
4	125.988	63.91	20.0606	69.33	10.59801	441.0907	1026.763	0.239314	0.064852	0.649083	0.110662	10.22942	386	9.66	2264.057
5	125.74	64.5334	21.93	69.5797	11.58562	441.2988	1027.005	0.239314	0.070862	0.647036	0.120946	11.21542	438	10.97	2343.202
6	126.07	64.1976	33.53	70.2222	17.7139	441.8342	1027.628	0.239314	0.108214	0.64915	0.18481	17.08169	708	17.76	2486.874

2. Diameter of Sonic nozzle-2 – 0.255 inches, FLOWMETER-Air High

	Calculated Data													
	Input Data													
	Diameter Used = 0.255 inches				0.255 R-Gas Con	53.35		32						
Sl.No	P_Air	T_Air(F)	P_Stagnat	T_Stagnat	P_Throat	T_Throat(	Speed_So	Area_Thro	Density_T	Density_t	m_dot	ACFM	K-Value	ACFM_M	K-Factor
1	109.111	76.2539	107.912	77.2149	57.00991	447.6612	1034.382	0.051071	0.343739	0.549194	0.126101	13.77662	571	14	2486.821
2	107.535	76.0213	81.4122	76.8243	43.01007	447.3357	1034.006	0.051071	0.259516	0.541497	0.095169	10.5451	435	11	2475.083
3	107.321	75.9281	59.0262	76.4131	31.18354	446.993	1033.61	0.051071	0.188301	0.540513	0.069027	7.662352	316	8	2474.436
4	107.012	75.7544	43.3122	76.1566	22.88184	446.7793	1033.363	0.051071	0.138238	0.539132	0.050662	5.63823	228	6	2426.293
5	106.812	75.6599	37.6122	76.0277	19.87053	446.6719	1033.238	0.051071	0.120074	0.538219	0.044	4.905117	168	4	2054.997
6	106.651	75.6088	31.2158	75.9601	16.49131	446.6156	1033.173	0.051071	0.099667	0.537459	0.03652	4.076957	35	1	515.09

3. Diameter of Sonic nozzle-2 – 0.255 inches, FLOWMETER- Air Medium

	Calculated Data												
	Input Data												
	Diameter Used = 0.255 inches				0.255 R-Gas Constant	53.35		32					
Sl.No	P_Air	T_Air(F)	P_Stagnation	T_Stagnation(F)	P_Throat	T_Throat(R)	Speed_Sound	Area_Throat(inch^2)	Density_Throat	Density_turbine	m_dot	ACFM	K-Value	K-Factor
1	104.661	75.8461	14.7748	75.4533	7.805527	446.1932349	1032.684621	0.051070516	0.04721797	0.527196932	0.017293	1.968163	221	6737.246
2	104.596	75.7894	14.824	75.4622	7.831519	446.2006513	1032.693204	0.051070516	0.047374418	0.526925271	0.017351	1.975719	314	9535.769
3	104.578	75.7638	15.3412	75.4851	8.104756	446.2197338	1032.715286	0.051070516	0.049025185	0.526859765	0.017956	2.044861	418	12264.89
4	104.546	75.7965	16.0061	75.5343	8.456023	446.2607322	1032.762727	0.051070516	0.051145277	0.526666406	0.018733	2.134172	551	15490.78
5	104.497	75.8558	17.73	75.5648	9.366759	446.2861478	1032.792136	0.051070516	0.056650534	0.526361305	0.02075	2.365331	622	15777.92
6	104.349	75.9373	19.6509	75.5821	10.38157	446.3005639	1032.808817	0.051070516	0.062786126	0.525535885	0.022998	2.625671	698	15950.21
7	104.2351	76.0761	19.9218	75.6121	10.52469	446.3255629	1032.837742	0.051070516	0.063648107	0.524826324	0.023314	2.665391	705	15870.09

VITA

Shankar Bhaskaran Narayanan received his Bachelor of Technology degree in mechanical engineering from the National Institute of Technology Karnataka, India in May 2008.

After that he worked for GE Oil and Gas on the reciprocating compressors team for 14 months in collaboration with Nuovo Pignone Italy.

He entered the mechanical engineering program at Texas A&M University in the Fall of 2009 and received his Master of Science degree in May 2011. His research interests include experiments in fluid mechanics, monitoring and instrumentation of turbo-machinery.

Shankar B. Narayanan

narayan.shankarb@gmail.com

Texas A&M University

Department of Mechanical Engineering

3123 TAMU

College Station, TX 77843-3123